

UC Riverside

UC Riverside Electronic Theses and Dissertations

Title

Synthesis and Application of Magnetic/Plasmonic Anisotropic Nanostructures

Permalink

<https://escholarship.org/uc/item/7n05k9bz>

Author

Wang, Xiaojing

Publication Date

2018

Copyright Information

This work is made available under the terms of a Creative Commons Attribution-NonCommercial-NoDerivatives License, available at <https://creativecommons.org/licenses/by-nc-nd/4.0/>

Peer reviewed|Thesis/dissertation

UNIVERSITY OF CALIFORNIA
RIVERSIDE

Synthesis and Application of Magnetic/Plasmonic
Anisotropic Nanostructures

A Dissertation submitted in partial satisfaction
of the requirements for the degree of

Doctor of Philosophy

in

Materials Science and Engineering

by

Xiaojing Wang

March 2018

Dissertation Committee:

Dr. Yadong Yin Chairperson

Dr. Ruoxue Yan

Dr. Boniface Fokwa

Copyright by
Xiaojing Wang
2018

The Dissertation of Xiaojing Wang is approved:

Committee Chairperson

University of California, Riverside

Acknowledgments

I would like to express my most profound gratitude to my advisor, Prof. Yadong Yin, for his academic advice and direction. I am ever grateful to him, and I am lucky to have the opportunity to work under his guidance. His insightful and knowledgeable guidance helps me to explore the mystery of nanoworld, and his wise and enlightened insight helps me to understand the real big world better.

I am also very thankful to my other committee members, Prof. Ruoxue Yan, and Prof. Boniface Fokwa, for their time spent in my final defense and valuable comments on my dissertation. My special thanks go to Dr. Yu Lu, for her assistance in scientific research as well as helpful tips in daily life.

I would like to thank my project collaborators: Dr. Huakang Yu, Dr. Zhiyuan Li, and Dr. Qiao Zhang and I learned a lot from them. I am much indebted to many past and current members of Yin group for providing a rich working experience, intellectual stimulation, and friendship: Dr. Le He, Dr. Michael Dahl, Dr. Mingsheng Wang, Dr. Yiding Liu, Dr. Yaocai Bai, Dr. Lishun Fu, Dr. Wenjing Xu, Ji Feng, Zhiwei Li, Fan Yang, Rashed Aleisa, Dr. Yoon Jae Lee, Dr. Anirban Das, Dr. Wenshou Wang, Qingsong Fan, Chaolumeng Wu, Dr. Yongqing Wang, Dr. Aiwei Tang, Dr. Guangsheng Wang, Dr. Hua Ma, Dr. Jingbing Liu, Dr. Dawei Wang, Dr. Shichuan Li, Dr. Chunyu Zhou, Dr. Mingfu Gong, Dr. Aiqin Gao, Dr. Yun Liu, Dr. Linru Xu, Jinxing Chen, Jian Zhang, Jian Liu, Shuai Zhou, Lan Peng, Panpan Xu, Wenwen Yin, Bo Li, Xiaojun Zeng, Zhouhui Xia, Zhenyuan Liu et al. I would also like to thank the undergraduate and high school students

who have worked and are working with me right now: Andrea Noronha, Dahae Jung, Brian Hwang, Soobean Kim, and Michael Lee.

I thank Dr. Krassimir N. Bozhilov, Dr. Mathias Rommelfanger, and Dr. Michael Pigeon for assistance in using facilities in CFAMM; Dr. Dan Borchardt for assistance in using optical facilities in Chemistry department. I also would like to thank Dr. Kevin Simpson for his help and guidance during my teaching.

I am incredibly grateful to my family for their support and understanding, which make this thesis possible. My thanks also go to my friends Yuping Zhang, Dr. Fangfang Zhang, Dr. Jiadeng zhu, Liling Kuang, Xue Di and Lyuye Niu for their valuable help.

Dedication

To my family.

ABSTRACT OF THE DISSERTATION

Synthesis and Application of Magnetic/Plasmonic Anisotropic Nanostructures

by

Xiaojing Wang

Doctor of Philosophy, Graduate Program in Materials Science and Engineering
University of California, Riverside, March 2018
Dr. Yadong Yin, Chairperson

Anisotropic properties of both magnetic and plasmonic nanostructures make them interesting research topics, as the shape anisotropy of the magnetic nanorods could be used to control their orientation and that of the plasmonic nanostructures attached to them. Thus, by applying an external magnetic field, instantaneous and reversible tuning of the plasmonic property of anisotropic metal nanostructures could be achieved. This holds great promises for developing novel optoelectronic devices and effective chemical and biomedical sensors. This dissertation discusses our efforts in the synthesis and application of magnetic/plasmonic anisotropic nanostructures.

Firstly, uniform nonmagnetic β -FeOOH nanorods with different sizes and aspect ratios were synthesized by the hydrolysis of FeCl_3 . Parameters influencing the synthesis, such as the concentration of reagents, different ligands, and temperature, were systematically studied. The indirect synthesis of magnetic iron oxide nanorods was achieved by a post-reduction method.

Then we successfully synthesized the anisotropic magnetic/plasmonic Fe_3O_4 NRs@ SiO_2 @Au core-shell nanocomposites by combining a post-reduction and a seeded growth method. The nanocomposites exhibited angle-dependent plasmonic property. Furthermore, we demonstrated the nanocomposites array, when fixed inside a polymer film, could find unique applications for information encryption. In particular, we have fabricated a six-column nanocomposite array film and demonstrate that it could realize multi-level information encryption. Taking advantage of the instantaneous tuning over the orientation of the nanocomposites in solution, we extended the working principle and fabricated a new type of magnetic field direction sensor. An actuator system which consists of the sensor and a MeArm base servo motor vividly showed the performance of the sensing ability.

Finally, we demonstrated that the confined growth of gold and silver nanorods within resorcinol-formaldehyde (RF) resin could be realized by using β -FeOOH nanorods as sacrificial templates through a seeded growth method. The RF shell is flexible and stretchable, due to its polymer nature, which offers more size tunability within one Au seed@RF template. At the same time, partially reduced Fe_xO_y @RF could serve as the reducing agent, and facilitate the gold shell formation between Fe_xO_y nanorod and RF layer. More efforts will be put into the investigation of formation mechanism and optimization of the shell quality.

Table of Contents

Acknowledgments.....	iv
Dedication	vi
Abstract of the Dissertation	vii
List of Tables	xii
List of Figures	xiii
Chapter 1 Introduction to Anisotropic Magnetic/Plasmonic Nanostructures	1
1.1 Magnetic Anisotropy	1
1.2 Anisotropic Plasmonic Metal Nanostructures	10
1.3 Dynamic Tuning of Photonic Properties	15
1.4 The Scope of This Dissertation	19
1.5 References	22
Chapter 2 Indirect Synthesis of Magnetic Iron Oxide Nanorods.....	24
2.1 Introduction	24
2.2 Materials and Methods	30
2.2.1 Materials	30
2.2.2 Synthesis of Nonmagnetic β -FeOOH Nanorods.....	30
2.2.3 Post-reduction Method to Form Magnetic Nanorods	31
2.2.4 Magnetophoresis Performance of Magnetic Nanorods.....	33
2.3 Results and Discussion.....	35
2.3.1 Synthesis of Nonmagnetic β -FeOOH Nanorods.....	35
2.3.2 Post-reduction Method to Form Magnetic Nanorods	54
2.3.3 Post-reduction Method for the Synthesis of Photonic Crystal.....	64
2.3.4 Magnetophoresis Performance of Magnetic Nanorods.....	66
2.4 Conclusion.....	73
2.5 References	75

Chapter 3 Anisotropic Magnetic/Plasmonic Composite Nanostructures for Information Encryption and Magnetic Field Sensing	77
3.1 Introduction	77
3.2 Materials and Methods	84
3.2.1 Materials	84
3.2.2 Synthesis of the Magnetic Iron Oxide Nanorods	84
3.2.3 The Growth of Gold Shell on Magnetic Nanorods	85
3.2.4 Magnetically Controlled Angle-dependent Plasmonic Property Measurement	87
3.2.5 FDTD Simulation of the Plasmonic Extinction	88
3.2.6 Fabrication of Polymer Film Consists of Nanocomposites Array with Different Orientations	88
3.2.7 Design and Setup of the Homemade IRPECS	89
3.2.8 Information Encryption by Using Nanocomposites Film Array	90
3.2.9 Information Decryption by Using the Identification System	90
3.2.10 Fabrication of Magnetic Field Direction Sensor	91
3.3 Results and Discussion	93
3.3.1 Synthesis of Anisotropic Magnetic/Plasmonic Nanocomposites	93
3.3.2 Magnetically Controlled Angle-dependent Plasmonic Property	99
3.3.3 Nanocomposites Array for Information Encryption	105
3.3.4 Application in Magnetic Field Direction Sensing	115
3.4 Conclusion	121
3.5 References	123
Chapter 4 Confined Growth of Gold/Silver Nanostructures within Resorcinol-formaldehyde (RF) Resin Templates	125
4.1 Introduction	125
4.2 Materials and Methods	130

4.2.1	Materials	130
4.2.2	Synthesis of Gold and Silver NRs within Hollow RF Templates.....	130
4.2.3	Confined Growth of Gold Shell within $\text{Fe}_x\text{O}_y@\text{RF}$ Templates.....	133
4.3	Results and Discussion.....	135
4.3.1	Synthesis of Gold and Silver NRs within Hollow RF Templates.....	135
4.3.2	Confined Growth of Gold Shell within $\text{Fe}_x\text{O}_y@\text{RF}$ Templates.....	143
4.4	Conclusion.....	151
4.5	References	152

List of Tables

Table 2.1 Size and aspect ratio evolution with different concentration of HCl.	37
Table 2.2 Size and aspect ratio evolution with different concentration of CTAB.	42
Table 2.3 Morphology and size evolution when changing the concentration of CTAC..	45
Table 2.4 Size and aspect ratio changes with different surfactant.	48
Table 2.5 FeOOH nanorods synthesized at 40 °C for different reaction time.	53
Table 2.6 Separation performance of magnetic nanorods.....	70
Table 4.1 Size and aspect ratio evolution of Au nanorods during the seeded growth with different amount of HAuCl ₄	140
Table 4.2 Summary of different partial reduction methods and their product when incubated with HAuCl ₄	145

List of Figures

Figure 1.1 (a-d) Spin configuration of the four types of magnetic exchange observable in magnetic materials without the effect of an external magnetic field. (e) Parameters describing the strength and magnetization of superparamagnetic, ferromagnetic and ferrimagnetic materials. Copyright © 2013 Springer. ¹²	3
Figure 1.2 Direction of the spontaneous magnetization of nanoparticles depending on various independent contributions: magnetocrystalline, surface and shape anisotropy. Copyright © 2013 Springer. ¹²	6
Figure 1.3 Direction of the spontaneous magnetization of nanoparticles with different shape and magnetic property when changing the direction of the external magnetic field.	8
Figure 1.4 (a) TEM image of Fe ₃ O ₄ @SiO ₂ nanorods. Scale bar: 1 μm; (b) SEM image of a fixed nanorod array in a polymer matrix. Scale bar: 1 μm; (c) Magnetic hysteresis loop of the nanorods; (d) Optical images showing the arrangement of nanorods. Scale bar: 10 μm. Reprinted with permission from Ref. ⁹ . Copyright © 2014 American Chemical Society.....	9
Figure 1.5 Tunable optical properties of gold nanorods by changing the aspect ratios. (a-c) Representative TEM images of AuNRs with increasing aspect ratios. (d) The digital image showing AuNRs solution with aspect ratio ranges from 2.4 to 5.7. (e) Extinction spectra showing AuNRs with different aspect ratios. Reproduced with permission from Ref. ²⁵ . © 2010 Elsevier.....	11
Figure 1.6 Tunable optical properties of gold and silver nanoplates. (a) Representative TEM image and extinction spectrum of gold nanoplates synthesized through polyvinylpyrrolidone (PVP)-assisted H ₂ O ₂ reduction method. Reprinted with permission from Ref. ²⁶ . Copyright © 2016 Royal Society of Chemistry. (b) Orientation-averaged extinction efficiency for trigonal prisms based on a 100-nm edge dimension with snips of 0, 10, and 20 nm. The inset shows the shape of a snipped prism. The prism thickness is 16 nm. Results are based on DDA calculations with a 2-nm cubic grid. For snip = 0, 68 704 dipoles are used in the calculation. Reprinted with permission from Ref. ¹⁶ . Copyright © 2003 American Chemical Society. (c-e) silver nanoparticles with irregular shapes can be converted to silver nanoplates in the presence of H ₂ O ₂ . (f) Digital image of silver nanoplates prepared in the presence of glycerol by tuning the synthetic	

conditions. Reprinted with permission from Ref. ²¹. Copyright © 2011 American Chemical Society. 14

Figure 1.7 Plasmon coupling between neighboring Au nanoparticles (AuNPs). (a, b) Role of salt in the spontaneous assembly of charged gold nanoparticles in ethanol. (a) Digital images and TEM images showing the assembly and disassembly of gold nanoparticles. (b) Normalized UV-vis extinction spectra of dispersions of centrifuged AuNP precipitation in EtOH (100 μ L) with the addition of different volumes of the supernatant of the original synthesis solution (0, 2, 5, 10 μ L). Reprinted with permission from Ref. ²⁷. Copyright © 2011 American Chemical Society. (c, d) The thermoresponsive tuning of plasmonic properties of charged colloidal AuNPs: AuNPs switching between the disassembled and assembled states in response to temperature changes. Reprinted with permission from Ref. ²⁴. Copyright © 2012 John Wiley and Sons. 16

Figure 1.8 Magnetically tunable photonic property. (a-e) Magnetically controlled assembly of superparamagnetic nanocrystal clusters into one-dimensional photonic crystals. (a, b) Representative TEM image and magnetic hysteresis loop. (c) Scheme of Bragg diffraction from the 1D chain-like structures assembled from the building blocks. (d) Reflectance spectra of an aqueous dispersion of chain-like structures under magnetic fields with different strengths. (e) Digital photos of an aqueous dispersion of one typical nanocluster sample encapsulated in a capillary tube with a width of 1 cm under magnetic fields with increasing strengths from left to right. Reproduced with permission from ref ²⁸. Copyright 2016 American Chemical Society. (f, g) Magnetic tuning of plasmonic excitation of gold nanorods. (f) TEM image of the as-assembled Fe₃O₄/Au NR structure. Scale bar: 100 nm. (g) From top to bottom: spectra of a dispersion of the hybrid nanostructures when changing the angle between the long axis of the nanorods and the polarization direction from 0° to 90°. Reprinted with permission from Ref. ¹⁸. Copyright © 2013 American Chemical Society. 18

Figure 2.1 (a, c) Morphology and magnetic properties of the as-prepared Fe₃O₄ nanostructures. Reprinted with permission from Ref. ⁴. Copyright © 2007 Springer. (b) The influence of the shape of iron particles on the coercivity. Reprinted with permission from Ref. ¹. Copyright © 2007 John Wiley and Sons. 25

Figure 2.2 Magnetic field induced synthesis of magnetic nanowires. TEM images of the samples obtained in zero magnetic field (a), and 0.15 T (b), 0.25 T (c), and 0.35 T (d)

magnetic fields. Reprinted with permission from Ref. ⁸. Copyright © 2013 John Wiley and Sons. 27

Figure 2.3 Indirect synthesis of magnetic nanorods. (a) An SEM image of the ellipsoidal colloids of hematite. Reprinted with permission from Ref. ¹⁴. Copyright © 2001 John Wiley and Sons. (b) TEM image of large akaganéite needles. Reprinted with permission from Ref. ¹⁵. Copyright © 2012 American Chemical Society. (c) TEM images of small akaganéite nanorods. Reprinted with permission from Ref. ¹⁶. Copyright © 2008 Nature Publishing Group. (d) Schematic illustration of the indirect synthesis of magnetic nanorods strategy. 29

Figure 2.4 TEM images of FeOOH nanorods synthesized with different concentration of HCl. (a) Without adding of HCl. (b-h) With 0.01 M (b), 0.02 M (c), 0.03 M (d), 0.04 M (e), 0.05 M (f), 0.06 M (g) and 0.07 M (h) HCl. Scale bars are 500 nm. 36

Figure 2.5 (a) TEM images of FeOOH nanorods synthesized with different concentration of $\text{FeCl}_3 \cdot 6\text{H}_2\text{O}$. (a) 0.1 M (b) 0.2 M (c) 0.3 M (d) 0.4 M (e) 0.5 M (f) 0.6 M. Scale bars are 200 nm. 39

Figure 2.6 Effect of concentration of CTAB. (a-d) TEM images of FeOOH nanorods synthesized without CTAB, and with different concentration of HCl: With 0 M (a), 0.02 M (b), 0.04 M (c), and 0.04 M (d) HCl. (e-h) TEM images of FeOOH nanorods synthesized with 0.5 g of CTAB, and with different concentration of HCl: With 0 M (e), 0.02 M (f), 0.04 M (g), and 0.04 M (h) HCl. (i, j) TEM images of FeOOH nanorods synthesized with 1.0 g of CTAB, and with different concentration of HCl: With 0 M (i), and 0.04 M (j) HCl. Scale bars are 500 nm. 41

Figure 2.7 Effect of concentration of CTAC. TEM images of FeOOH nanorods synthesized with different concentration of CTAC: With 0 M (a), 0.01 M (b), 0.02 M (c), 0.04 M (d), 0.08 M (e), and 0.16 M (f) of CTAC. Scale bars are 200 nm. 44

Figure 2.8 FeOOH nanorods synthesized with different surfactants (a) With no surfactant. (b) With 0.5 g of CTAB. (c) With 0.08 M NaCl. (d) With 0.5 g of CTAB and 0.08 M of NaCl. Scale bars are 200 nm. 47

Figure 2.9 Synthesis of quasi-spherical FeOOH nanoclusters by adjusting the concentration of $\text{FeCl}_3 \cdot 6\text{H}_2\text{O}$ and CTAC. (a) With 0.1 M $\text{FeCl}_3 \cdot 6\text{H}_2\text{O}$ and 0.08 M CTAC.

(b) With 0.1 M $\text{FeCl}_3 \cdot 6\text{H}_2\text{O}$ and 0.04 M CTAC. (c) With 0.2 M $\text{FeCl}_3 \cdot 6\text{H}_2\text{O}$ and 0.08 M CTAC. (a) With 0.05 M $\text{FeCl}_3 \cdot 6\text{H}_2\text{O}$ and 0.08 M CTAC. Scale bars are 200 nm. 49

Figure 2.10 (a-e) FeOOH nanostructures synthesized by different reaction parameters. Scale bars are 200 nm. (a) 2 μm nanorods synthesized by using 0.6 M FeCl_3 and 0.07 M of HCl at 98 °C for 24 h. (b) Nanoclusters synthesized with 0.1 M $\text{FeCl}_3 \cdot 6\text{H}_2\text{O}$ and 0.08 M CTAC at 87 °C for 24 h. (c) Nanorods synthesized with 0.08 M NaCl at 87 °C for 24 h. (d) Nanorods synthesized by using 0.1 M $\text{FeCl}_3 \cdot 6\text{H}_2\text{O}$ and 0.05 M of HCl at 98 °C for 24 h. (e) Nanorods synthesized by using 0.1 M $\text{FeCl}_3 \cdot 6\text{H}_2\text{O}$ and 0.5 g CTAB. (f) XRD patterns of all the above mentioned FeOOH nanostructures. 51

Figure 2.11 Effect of reaction temperature. FeOOH nanorods synthesized at 40 °C for different reaction time: (a) 26 h, (b) 34 h, (c) 42 h, (d) 48 h, (e & g) 5 days, and (f & h) 13 days. Scale bars in a-f are 100 nm. 52

Figure 2.12 Solution phase polyol reduction of FeOOH nanorods. (a) Scheme showing the chemical transformation during surface protected polyol reduction. (b-e) TEM images of $\beta\text{-FeOOH}$ and $\beta\text{-FeOOH}$ reduced for 1, 4, and 8 h, respectively, (scale bars, 50 nm; insets, 20 nm) and (f) XRD. (g) The mass magnetization M as a function of applied external field H for the dried 8 h magnetite measured at 300 K (inset, expanded low-field curve). Figure a-g are reprinted with permission from Ref. ¹⁹. Copyright © 2017 American Chemical Society. (h & i) TEM images of $\beta\text{-FeOOH}$ nanorods with large aspect ratio before (h) and after (i) polyol reduction. (j & k) TEM images of $\beta\text{-FeOOH}$ nanoclusters before (j) and after (k) polyol reduction. Scale bars in h-k are 200 nm. 58

Figure 2.13 Solid phase hydrogen reduction. (a-d) $\text{FeOOH}@\text{SiO}_2$ nanorods reduced by forming gas at 360 °C for 2 h. (a) TEM image of $\text{FeOOH}@\text{SiO}_2$ with 15 nm silica coating after reduction. (b & c) TEM image and magnetic hysteresis loop of $\text{FeOOH}@\text{SiO}_2$ with 40 nm silica coating after reduction. (d) XRD patterns of $\text{FeOOH}@\text{SiO}_2$ with 40 nm silica coating before and after reduction. (e-h) $\text{FeOOH}@\text{SiO}_2$ nanorods reduced by hydrogen gas at 500 °C for 2 h. (e) TEM images of FeOOH nanorods. (f & g) TEM image and magnetic hysteresis loop of $\text{FeOOH}@\text{SiO}_2$ after reduction. (h) Red line: XRD patterns of $\text{FeOOH}@\text{SiO}_2$ after reduction. The green line is for another sample which is not mentioned here. Scale bars are 200 nm. Figure e-h are reprinted with permission from Ref. ²². Copyright © 2015 John Wiley and Sons. 61

Figure 2.14 Solid phase carbothermal reduction. (a) scheme showing the carbothermal reduction procedure for FeOOH nanorods. (b) XRD patterns of FeOOH@RF nanorods reduced by the carbothermal method at a different temperature. (c-e) TEM images of FeOOH@RF nanorods before (c) and after carbothermal reduction at 550 °C (d) and 600 °C (e). Scale bars are 500 nm. 63

Figure 2.15 Post-reduction method for the synthesis of CNC-like photonic crystal. (a) Digital image of FeOOH@SiO₂ nanoclusters reduced in DEG for 4 h and 24 h, respectively. (b) Digital image showing the magnetic separation for sample reduced for 24 h. (c) FeOOH@SiO₂ nanoclusters reduced by hydrogen under different parameters all show structure color. (d) Structure color of 3-D photonic crystal assembled from sample magnetically separated in b. (e) Optical microscope image of the sample (2) in c. (f & g) TEM images of supernatant and magnetic separated nanoparticles from b. (h) TEM image of the sample (2) in c. Scale bars are 100 nm. 65

Figure 2.16 TEM images of FeOOH nanorods for separation. (a) As-synthesized FeOOH nanorods. (b-e) FeOOH@SiO₂ nanorods with 7.5 nm, 12.5 nm, 28 nm and 33 nm of silica coating, respectively. (f & g) FeOOH@SiO₂ with 12.5 nm silica coating after oxalic acid etching for 3 h. (h) Nanorods first etched by oxalic acid for 3 h and then reduced by DEG. Scale bars in a, f and h are 500 nm, and in other images are 100 nm..... 67

Figure 2.17 Magnetic nanorods for magnetophoresis and separation. (a-f) Fe₃O₄@SiO₂ nanorods before (a, c and e) and after (b, d, and f) oxalic etching and separated in DI water (a, b), pH = 8.75 buffer (c, d) and pH = 7.30 buffer (e, f). (g-l) Optical microscope images of the nanorods after separation and re-dispersed in water. (g-k) Nanorods before and (h-i) after etching and separated in DI water (g, h), pH = 8.75 buffer (I, j), and pH = 7.30 buffer (k, l), respectively..... 69

Figure 2.18 Magnetic nanorods with different oxalic acid etching time for separation (a) Real-time transmittance measurement during the separation procedure. Inset image shows the set up for the measurement. (b-d) TEM images of FeOOH@SiO₂ nanorods etched by oxalic acid for 3 h, 5 h, and 7 h, respectively. Scale bars in b and c are 200 nm, and scale bar in d is 1 μm. 72

Figure 3.1 Magnetic tuning of plasmonic excitation of gold nanorods. (a) Scheme showing the plasmon excitation of AuNRs under polarized light. (b) Spectra of a dispersion of the hybrid nanostructures under a magnetic field with its direction varying

from perpendicular to parallel within the yz plane. The incident light is polarized along the z-axis. The inset shows digital images of the dispersion under a magnetic field with its direction parallel (bottom) and perpendicular (up) to the incident beam. (c) Spectra of the dispersion under a magnetic field with its direction varying within the xy plane from perpendicular to parallel relative to the incident light. (d, e) TEM images of the assembled $\text{Fe}_3\text{O}_4/\text{Au}$ NR structure. Scale bar: 100 nm. Reprinted with permission from Ref. ³. Copyright © 2013 American Chemical Society. 79

Figure 3.2 Magnetically switchable plasmonic nanorods assembled from a binary nanocrystal mixture. (a) Schematic of the $\text{Zn}_{0.2}\text{Fe}_{2.8}\text{O}_4/\text{Au}$ hybrid nanorod fabrication process. Step 1: a Si substrate with a spin-coated bilayer of Durimide and the thermal resist is imprinted with a nanorod-pillar-patterned stamp. Step 2: a mixture of Au and $\text{Zn}_{0.2}\text{Fe}_{2.8}\text{O}_4$ nanocrystals is deposited by spin-coating. Step 3: resist lift-off. Step 4: ligand-exchange of the patterned nanocrystal-based nanorods with NH_4SCN . Step 5: nanorod release on dissolving the Durimide layer. (b,c) Low- and high-resolution SEM images, respectively, of hybrid nanorod arrays before release. Scale bars, 1 μm for (b); 250 nm for (c). (d) Transmission spectra of the 1:3 vol/vol $\text{Zn}_{0.2}\text{Fe}_{2.8}\text{O}_4/\text{Au}$ hybrid nanorod array as a function of the polarization angle, θ , of incident light from 0° , for light polarized along the longitudinal direction, to 90° , for light polarized along the transverse direction. (e) Dependence of nanorod array transmission at 2,600 nm on θ , the angle between the light polarization direction (black double-headed arrow) and the nanorod (green) orientation. (f) Schematic of the modulated light transmission by controlling the orientation of the hybrid nanorods (green). Black double-headed arrows represent light polarization direction, and light blue arrows represent a light path. e, the cyclic performance of the light transmission at 2,600 nm for a 100- μm path length hybrid nanorod suspension in Remover PG under an alternating 120 Oe external magnetic field. Transmission for nanorods oriented perpendicular (above red line) and parallel (below red line) to the light polarization direction. Reprinted with permission from Ref. ¹¹. Copyright © 2016 Nature Publishing Group. 82

Figure 3.3 Synthesis and characterization of anisotropic magnetic/plasmonic Fe_3O_4 NRs@ SiO_2 @Au shell nanocomposites. (a) Scheme showing the synthesis procedure. (b) TEM image of $\beta\text{-FeOOH}$ nanorods. The size of the nanorods is 286 nm in length and 45 nm in width. (c) TEM image of the magnetic Fe_3O_4 NRs@ SiO_2 after forming gas reduction. The thickness of silica coating is 45 nm. (d) A three-dimensional schematic illustration of the nanocomposite structure. (e) Magnetic hysteresis loop of Fe_3O_4

NRs@SiO₂. (f) TEM image of Fe₃O₄ NRs@SiO₂@Au shell after seeded growth to form a complete gold shell coating. The thickness of the gold shell is measured to be 36.5 nm. (g) TEM image of the gold seed loaded NRs. Scale bars in b, c, f, and g are 200 nm. 94

Figure 3.4 (a) UV-Vis spectra measured during the seeded growth process with different amount of the gold growth solution. (b-d) TEM images of the nanocomposites when the amount of the gold growth solution is 1, 4 and 12 mL, respectively..... 98

Figure 3.5 Magnetically controlled angle-dependent plasmonic property of the nanocomposites. (a) Schematic representation of the setup for plasmonic extinction measurement. (b) Extinction spectra measured when changing θ from 0° to 90° by 10° each time. The spectra are measured in a solution with CS₂ as the solvent. (c) Extinction spectra of the nanocomposites with θ of 90 ° and 0°, and without applying the external magnetic field, respectively. The inset shows the TEM image of a typical nanocomposite. (d) Calculated extinction spectra using the finite-difference time-domain (FDTD) method with θ of 90 ° and 0°. The inset shows the scheme of the nanocomposite used for simulation. (e) Electric field distributions, from top to bottom, under different excitation wavelengths of each peak as shown in extinction spectra: located at 601 nm, 692 nm, 958 nm, 1280 nm, and 1910 nm, respectively. The left column is when incident light polarized along the transverse axis (i.e., $\theta = 90^\circ$), and the right column is when incident light polarized along the longitudinal axis (i.e., $\theta = 0^\circ$). 100

Figure 3.6 (a) Extinction spectra of the Fe₃O₄@SiO₂ NRs in PEGDA solution with θ of 90 ° and 0°, and without applying the external magnetic field, respectively. (b) Extinction spectra of CS₂..... 102

Figure 3.7 The electrical response of the nanocomposites array when tested by a homemade IR photoelectric coupling system. (a) Schematic illustration of the three polymer films consist of nanocomposites with different orientations (top row) and the digital images of the fabricated film. (b, c) Extinction spectra of the film measured under the illumination of linearly Z-polarized light (b) and linearly Y-polarized light (c). (d) Diagram of the homemade IR photoelectric coupling system (IRPECS). (e, f) Voltage of the film measured under the illumination of linearly Z-polarized light (e) and linearly Y-polarized light (f). 107

Figure 3.8 (a) Spectrum of the IR light source. (b) Photodiode responsivity profile. 108

Figure 3.9 Diagram of the homemade IR photoelectric coupling system (IRPECS, left part) combined with the identification system (right part), which is a common anode LED that connected to the IRPECS through ARDUINO..... 110

Figure 3.10 Nanocomposites array for information encryption. (a) Digital image of the fabricated film which consists of six building blocks. The sequence of the six columns is film 0, 1, 2, 0, 1, 2. (b) Digital image showing the IR light source, sample stage and photodiode part of the homemade IR photoelectric coupling system (on the right), and a common anode LED which connected to the system through ARDUINO (on the left). (c, d) Scheme showing the two decryption methods for the fabricated polymer film when using linearly Y-polarized light (c) and Z-polarized light (d), respectively. (e, f) A different voltage reading of the film when measured under the illumination of linearly Y-polarized light (e) and Z-polarized light (f). Insets: corresponding LED color when reading the specific column of the film. 111

Figure 3.11 27 possible combinations of a three-column film, which shows a “222” reading under the Y-polarized light when reading under the Z-polarized light. 114

Figure 3.12 Magnetically controlled real-time photoelectric response of the nanocomposites in solution and its application for magnetic field direction sensor. (a) Schematic representation of the sample stage part. A cuvette containing the sample solution was placed in between the light source and the photodiode. A permanent magnet was used to dynamically control the orientation of the nanocomposites in XY plane. (b) Circuit diagram of the magnetic field direction sensor (left part) and an actuator (right part). (c) Extinction spectra and photoelectric response of the nanocomposites in solution when changing θ from 90° to 0° , by 10° each time. (d) Voltage plotted over θ angle and its sine fit. (e) Integration of the measured extinction from 1300 nm to 1700 nm of the nanocomposites in PEG-DA solution plotted over θ angle and its sine fit. (For both d and e, when θ changes from 90° all the way back to 0° , we did the conversion for the angle to be 90° to 180° . The similar conversion has been done for the second cycle of the angle change to be 180° to 360° .) (f) Digital images showing the magnetic field direction sensor based actuator system. From left to right, the robotic arm moved accordingly when changing the direction of the external magnetic field..... 117

Figure 3.13 θ angle (a) and voltage (b) plotted over time when using a servo motor which equipped with a permanent magnet to apply the external magnetic field. The rotation rate

of the servo motor is 10° per 50 ms. The voltage was measured by using the homemade IR photoelectric coupling system (see Figure 3.7d for circuit diagram). Insets in b are the corresponding θ angles. 119

Figure 4.1 Template synthesis of AuNRs by using hollow silica tube as templates. (a) Scheme showing a general templating approach to the synthesis of metal nanorods. (b-e) TEM images of the (b) silica nanotubes with inner cavity functionalized with amino groups; (c) Au seed@silica nanotubes; (d) Au nanorod@silica nanotubes after seeded growth; (e) Au nanorods after removal of silica templates. Reprinted with permission from Ref. ³. Copyright © 2011 American Chemical Society. 127

Figure 4.2 Template synthesis of anisotropic nanostructures. (a) Scheme showing the template synthesis of hollow anisotropic nanostructures. Reprinted with permission from Ref. ². Copyright © 2016 American Chemical Society. (b) Outline of the confined dewetting process for the fabrication of Au nanocups. (c-h) SEM images of the Au nanocups prepared using templates of 350 nm silica coated with RF thickness of (a) 25 nm, (b) 18 nm, and (c) 12 nm, demonstrating the convenient control over cup opening by the thickness of the RF layer. (d-f) SEM images of Au nanocups obtained using silica cores with diameters of ≈ 80 , ≈ 250 , and ≈ 350 nm. All scale bars are 200 nm. Reprinted with permission from Ref. ⁹. Copyright © 2013 John Wiley and Sons. 129

Figure 4.3 Confined growth of Au/Ag nanostructures within RF resin by using FeOOH NRs as templates: synthesis strategy and Au seed loading. (a) Scheme for the synthesis strategy. (b) TEM image of FeOOH NRs. (c) TEM image of Au seed loaded FeOOH NRs after RF coating. (d) TEM image of Au seed@void@RF when removing the FeOOH NRs template. Scale bars are 100 nm. 136

Figure 4.4 Confined growth of Au nanorods within RF resin by using FeOOH NRs as templates: the seeded growth of gold with different amount of HAuCl₄. (a-f) TEM images of (a) Au seed@void@RF template and AuNRs synthesized by seeded growth with (b) 5 μ L, (c) 7.5 μ L, (d) 20 μ L, (e) 30 μ L, and (f) 60 μ L of 0.05 M HAuCl₄. (g) Extinction spectra of the as-synthesized AuNRs with different amount of HAuCl₄. Scale bars are 100 nm. 139

Figure 4.5 Confined growth of Ag nanorods within RF resin by using FeOOH NRs as templates: seeded growth. (a, d) The growth of silver based on Au seed@void@RF. (a) TEM image of Ag nanorod synthesized by using 50 μ L of 0.1 M AgNO₃. (d) Extinction

spectrum of the synthesized Ag nanorod. (b, c & e) The growth of silver based on Au NRs@void@RF. (b) AuNRs synthesized by seeded growth with 5 μL HAuCl_4 of as the seed for the growth of silver. (c) TEM image after growth of silver by using 45 μL of 0.1 M AgNO_3 . (e) Extinction spectra before and after growth of silver. Scale bars are 100 nm. 142

Figure 4.6 Confined growth of gold shell within Fe_xO_y @RF composite. (a) scheme showing the synthesis procedure. (b-k) TEM images of partially reduced FeOOH @RF nanorods incubated with HAuCl_4 with (b-f) and without (g-k) the addition of $\text{NH}_3\cdot\text{H}_2\text{O}$. The partial reduction parameters are 300 $^\circ\text{C}$, 2 h by carbothermal reduction (b, g), 300 $^\circ\text{C}$, 2 h by carbothermal reduction with the protection of silica (c, h), 200 $^\circ\text{C}$, 2 h by carbothermal reduction (d, i), 400 $^\circ\text{C}$, 2 h by carbothermal reduction with the protection of silica (e, j), and 220 $^\circ\text{C}$, 10 min by DEG. Scale bars are 100 nm. 144

Figure 4.7 Confined growth of gold shell within Fe_xO_y @RF composite with different reaction time. (a) UV-Vis spectra of samples synthesized with different reaction time. (b, c) TEM images of samples synthesized with 45 min (b) and 90 min (c), respectively. Scale bars are 200 nm. 147

Figure 4.8 Effect of the concentration of $\text{NH}_3\cdot\text{H}_2\text{O}$. TEM images of sample synthesized with (a) 40 μL $\text{NH}_3\cdot\text{H}_2\text{O}$, (b) 200 μL $\text{NH}_3\cdot\text{H}_2\text{O}$, (b) 400 μL $\text{NH}_3\cdot\text{H}_2\text{O}$, and (d) NaOH. Scale bars are 200 nm. 148

Figure 4.9 (a) TEM image of Fe_xO_y @Au shell@RF when etching away the Fe_xO_y nanorods. (b, c) TEM image of Fe_xO_y @Au shell@RF when etching away the RF layer. 150

Chapter 1 Introduction to Anisotropic Magnetic/Plasmonic Nanostructures

1.1 Magnetic Anisotropy

Magnetic nanoparticles have attracted tremendous research interests recently, due to their magnetic property, and could find application in many areas such as magnetic resonance imaging,^{1,2} biomedicine,^{3,4} magnetically controlled assembly,⁵ data storage,⁶ energy storage⁴ and environmental remediation.^{7,8} Anisotropic property of magnetic nanostructures makes them interesting research topics, as the shape anisotropy of the magnetic nanorods could be used to control the orientation of the nanorods.^{9,10}

Magnetism originates from the magnetic dipoles associated to the electron spin and orbital moment. As shown in Figure 1.1e, the three main parameters that can describe the magnetic strength and magnetization of the material are: the coercive field (H_C), the saturation magnetization (M_S) and the remanent magnetization (M_R). H_C is the external field required to reduce the magnetization back to zero; M_S is the maximum value of magnetization that the material can reach with increasing field; M_R indicates the residual magnetization of the material at zero applied field.

Depending on the magnetic response observed, there are mainly five types of magnetism: diamagnetism, paramagnetism, ferromagnetism, ferrimagnetism, and antiferromagnetism.¹¹ A material that creates a magnetic dipole in opposition to an externally applied magnetic field, which causing a repulsive effect, is called diamagnet. Oppositely to diamagnets, the other four types of magnetic materials are attracted by the applied magnetic field (Figure 1.1 a-d).

For a material shows randomly oriented magnetic dipoles that can only be aligned in the presence of an external magnetic field and along its direction, it is paramagnetic. Superparamagnetism (Figure 1.1a), describes the magnetic behavior of a material in which all the spins are always collinear to each other, but they collectively move randomly. Only when an external magnetic field is applied along a certain direction, the spins align along the same direction. A superparamagnetic material shows zero coercivity and remanence (Figure 1.1e, purple dotted line), which means when the external magnetic field is switched off, the internal magnetic dipoles randomize again and no energy is required to demagnetize the material.

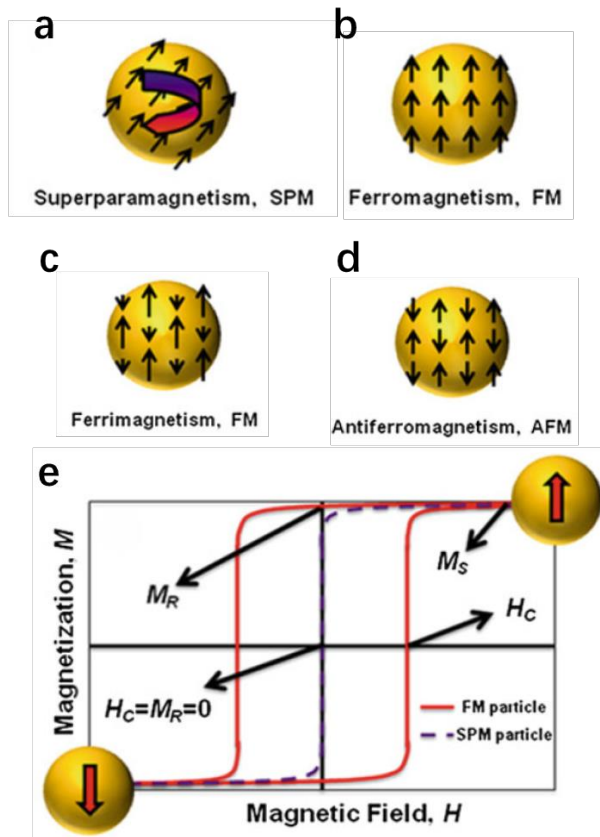


Figure 1.1 (a-d) Spin configuration of the four types of magnetic exchange observable in magnetic materials without the effect of an external magnetic field. (e) Parameters describing the strength and magnetization of superparamagnetic, ferromagnetic and ferrimagnetic materials. Copyright © 2013 Springer.¹²

If the spins align parallel to each other, an enhanced collective response is observed. This is what is known as ferromagnetism (Figure 1.1b). In contrast to the ferromagnetic situation, neighboring magnetic dipoles can align antiparallel in the lattice, which means that they cancel each other. This type of magnetic exchange can lead to two different situations: antiferromagnetism (Figure 1.1d), and ferrimagnetism (Figure 1.1c). For antiferromagnetism, the magnetic dipoles or spins interacting present the same value and hence the material exhibits a net zero magnetization. For ferrimagnetism, the two coupled spins show different values, and a net magnetic dipole different than zero still magnetizes the material, even in the absence of the external magnetic field. For ferromagnetic and ferrimagnetic materials, when the external magnetic field is switched off, the internal magnetic dipoles could not randomize, thus leaves a the remanent magnetization (M_R) and extra energy (the coercive field, H_C) is required to demagnetize the material.

Magnetic anisotropy is the dependence of the internal energy on the direction of the spontaneous magnetization. The directions of magnetization could be classified into easy and hard directions, based on the total energy of the material. Briefly, easy direction minimizes the total energy of the material, while hard direction maximizes the total energy of the material. The most energetically stable configuration is the one where the total magnetization vector lies along the easy direction/s.

Magnetic anisotropy consists of three independent contributions from magnetocrystalline, surface and shape anisotropy (Figure 1.2). Magnetocrystalline anisotropy derives from the crystalline symmetry of the material and hence reflects the same symmetry. It is an intrinsic characteristic of the material and does not depend on the

presence of an external field.

Surface anisotropy is related to the surface to volume ratio, which is more evident for nanomaterials. Surface anisotropy can increase by more than one order of magnitude the total anisotropy of the sample with decreasing size from bulk to nanocrystals. Atoms located at the surface show an incomplete coordination sphere, and this leads to a broken symmetry compared to the core atoms. Such decrease in the crystalline symmetry at the surface induces a different orientation of the surface spins concerning the magnetization direction, spin pinning and surface-core strains that reduce the surface energy.¹³

The shape anisotropy is a dipolar contribution. Shape anisotropy states that an elongated nanocrystal in the z-direction minimizes its shape energy by aligning the magnetization direction with the long axis of the particle.¹² This arises from the demagnetizing field associated with the surface magnetic charge distribution (magnetic dipoles) of a magnetic object.¹⁴ The demagnetizing field generated in non-spherical nanoparticles is a consequence of the long-range dipolar interactions in the particle.

In thin films, fine particles and nanocrystals, surface and shape anisotropies acquire a significant weight. It is worth to point out that shape anisotropy can be the dominant effect even for bulk materials, which show large values of M_s and low magnetocrystalline anisotropy.¹⁵

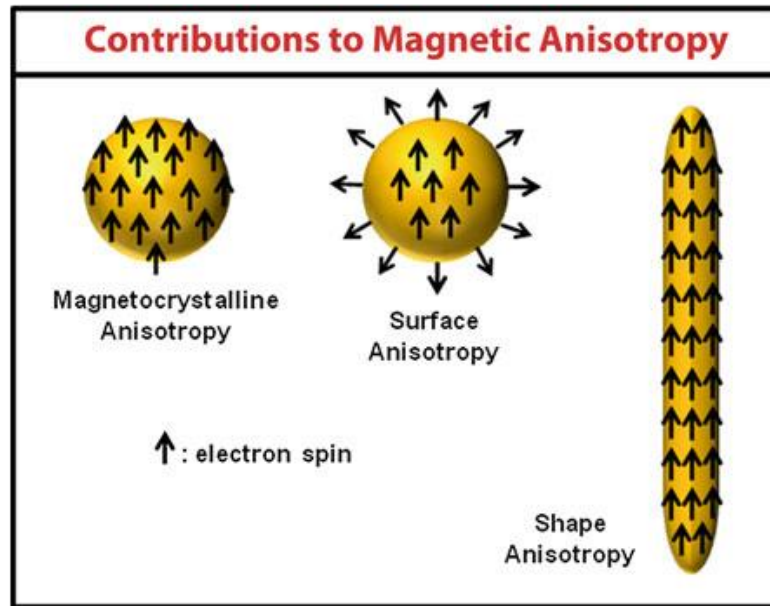


Figure 1.2 Direction of the spontaneous magnetization of nanoparticles depending on various independent contributions: magnetocrystalline, surface and shape anisotropy. Copyright © 2013 Springer.¹²

Due to the shape anisotropy and ferromagnetic/ferrimagnetic nature, the orientation of the magnetic nanorods could be efficiently controlled by applying an external magnetic field, as shown in Figure 1.3. For spherical paramagnetic nanoparticles, when the external magnetic field direction changes, the magnetization inside the particles will change their direction accordingly, thus the particles themselves would not rotate. However, for ferromagnetic nanoparticles, when the external magnetic field direction changes, since the magnetization inside the particles will remain its original orientation, thus resulting in the rotating of the nanoparticles to align the internal magnetization parallel to the external magnetic field. For ferromagnetic spherical nanoparticles, we will not realize the rotation since the particles are isotropic; but for anisotropic nanorods, we will observe the nanorods rotating with the changing of the external magnetic field direction.

One example of the orientation control over the magnetic nanorods by applying an external magnetic field is shown in Figure 1.4. From the SEM image, we can see that the orientation of the nanorods has been fixed and they all parallel with each other. The optical images in Figure 1.4d show that when the external magnetic field direction changes, the magnetic nanorods align themselves parallelly to the magnetic field direction.



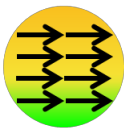
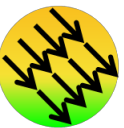
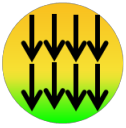


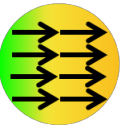



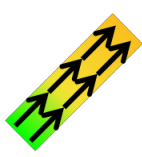
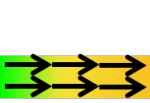
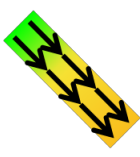

Magnetic field direction Type of materials		↑	↗	→	↘	↓
Paramagnetic						
Ferromagnetic						
Ferromagnetic						

Figure 1.3 Direction of the spontaneous magnetization of nanoparticles with different shape and magnetic property when changing the direction of the external magnetic field.

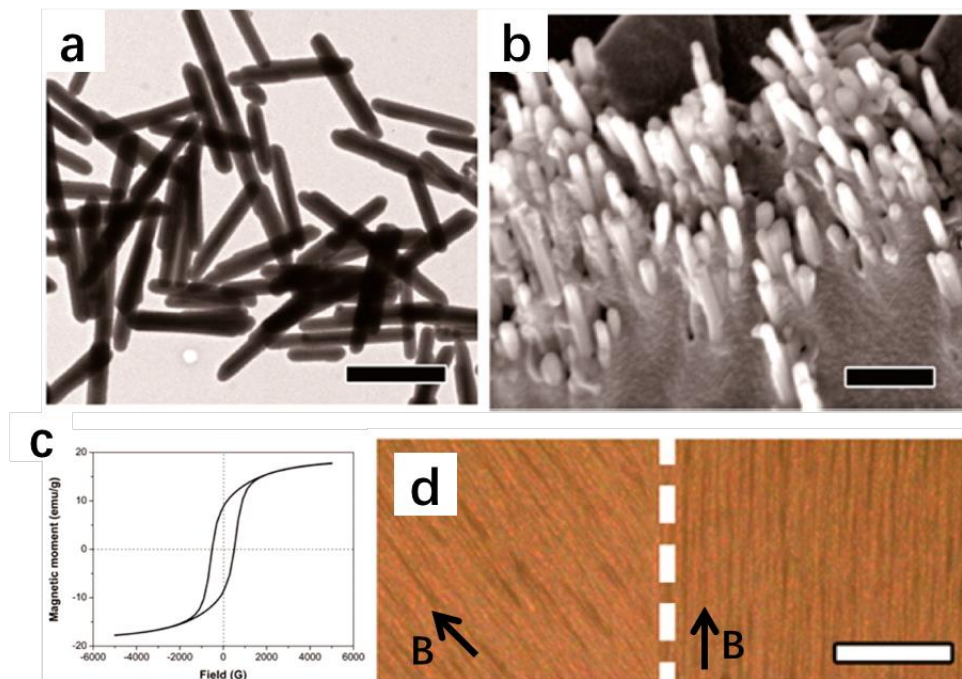


Figure 1.4 (a) TEM image of $\text{Fe}_3\text{O}_4@\text{SiO}_2$ nanorods. Scale bar: 1 μm ; (b) SEM image of a fixed nanorod array in a polymer matrix. Scale bar: 1 μm ; (c) Magnetic hysteresis loop of the nanorods; (d) Optical images showing the arrangement of nanorods. Scale bar: 10 μm . Reprinted with permission from Ref. ⁹. Copyright © 2014 American Chemical Society.

1.2 Anisotropic Plasmonic Metal Nanostructures

The plasmonic properties of metal nanostructures are mainly due to their size, shape and geometrical arrangement.¹⁶⁻¹⁹ Compared to isotropic spherical particles, anisotropic nanostructures like nanorods, nanoplates, could offer tunability in plasmonic properties by controlling their shapes^{20,21} and geometric arrangement²²⁻²⁴.

For gold nanoparticles, they show an intrinsic plasmon extinction peak at about 520 nm. When changing the shape of nanoparticles from sphere to nanorod, another extinction peak corresponding to the longitudinal mode emerges, as shown in Figure 1.5e. The peak at about 520 nm corresponds to the transverse mode. When increasing the aspect ratio of the nanorods, the extinction peak for longitudinal mode gradually red-shifts, thus the color of the nanorods solution gradually changes, as shown in Figure 1.5d.²⁵

Other than one-dimensional nanorods, two-dimensional gold and silver nanoplates (e.g., nanotriangles, nanohexagons), with their lateral dimensions significantly being larger than their thicknesses, also show the similar anisotropic plasmonic property. Figure 1.6a shows that for gold nanoplates, there are also two extinction peaks, which corresponding to the in-plane and out-of-plane modes.²⁶

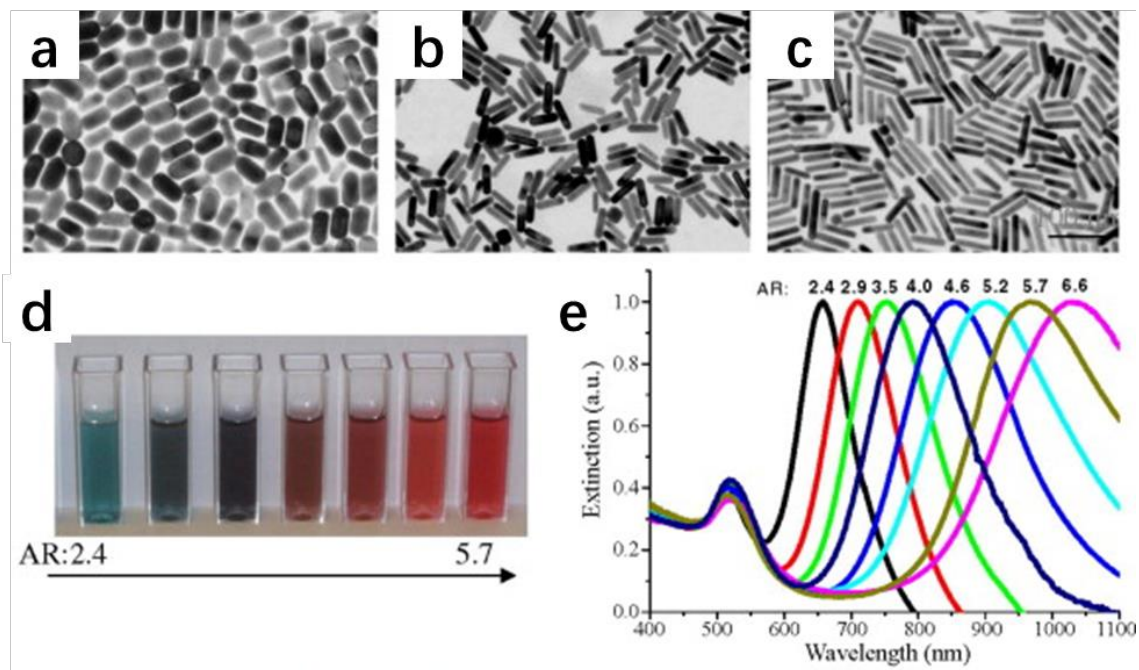


Figure 1.5 Tunable optical properties of gold nanorods by changing the aspect ratios. (a-c) Representative TEM images of AuNRs with increasing aspect ratios. (d) The digital image showing AuNRs solution with aspect ratio ranges from 2.4 to 5.7. (e) Extinction spectra showing AuNRs with different aspect ratios. Reproduced with permission from Ref. ²⁵. © 2010 Elsevier.

The shape of the nanoplates will also influence the plasmonic property. The spectra in Figure 1.6b show a long wavelength peak at 770 nm (referring to the perfect triangle), a weaker peak at 460 nm, and a small but sharp peak at 335 nm. Also, we see that the red-most peak is very sensitive to snipping, with the 20-nm snipped prism giving a peak that is blue-shifted by 100 nm as compared to the perfect prism. The other peaks are more weakly sensitive to snipping.¹⁶

Not only gold but also silver nanoplates show the anisotropic plasmonic property. As shown in Figure 1.6c, when changing the shape of silver nanoparticles to nanoplates, other than the intrinsic peak at about 400 nm for silver nanoparticles, two extinction peaks at longer wavelengths emerged. TEM images (Figure 1.6d & e) confirm the morphology change, and digital images show an apparent color change from yellow to blue. Similar to gold nanorods, when changing the synthetic conditions, the extinction peak, as well as the color of the products could be readily adjusted.²¹

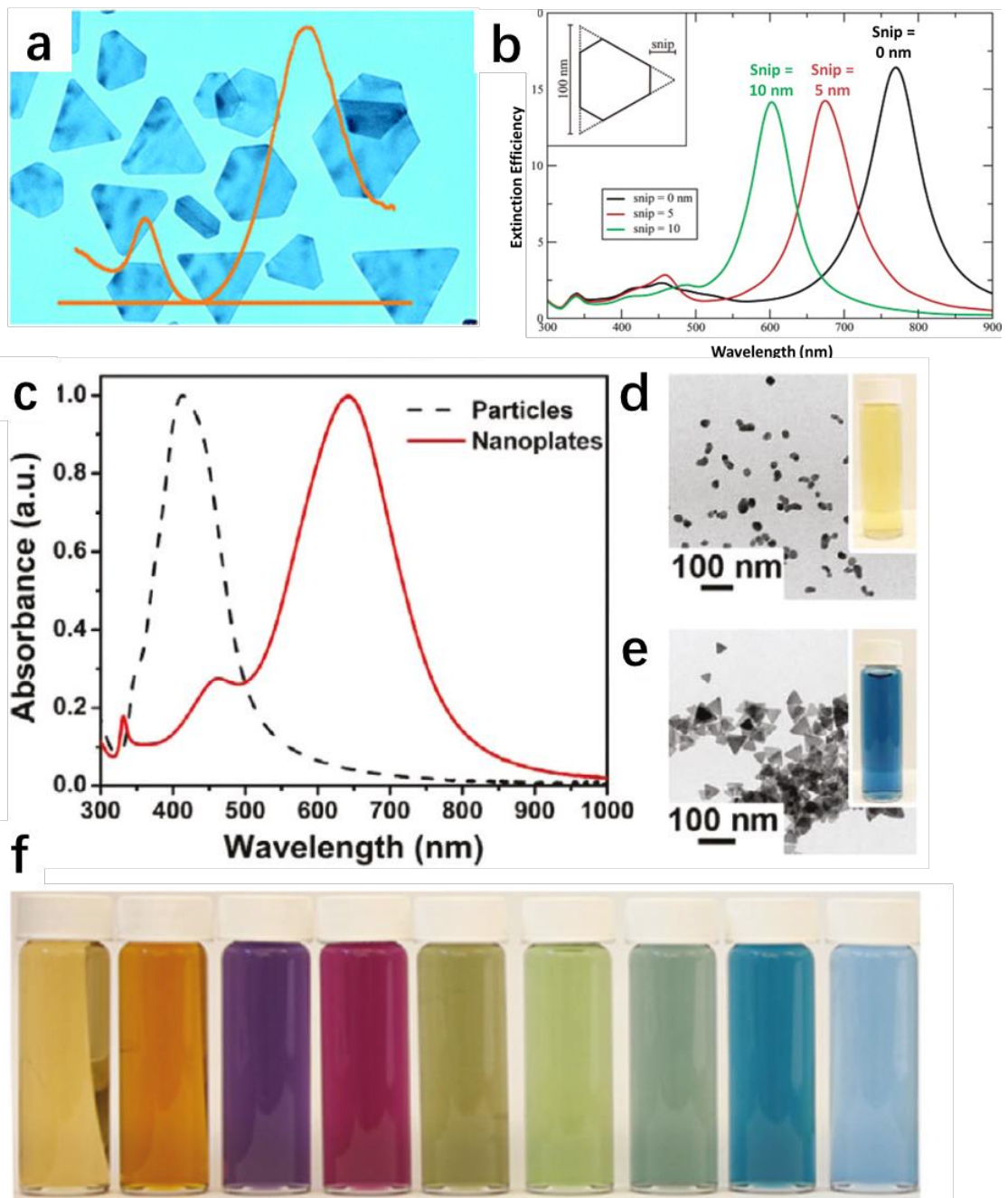


Figure 1.6 Tunable optical properties of gold and silver nanoplates. (a) Representative TEM image and extinction spectrum of gold nanoplates synthesized through polyvinylpyrrolidone (PVP)-assisted H_2O_2 reduction method. Reprinted with permission from Ref. ²⁶. Copyright © 2016 Royal Society of Chemistry. (b) Orientation-averaged extinction efficiency for trigonal prisms based on a 100-nm edge dimension with snips of 0, 10, and 20 nm. The inset shows the shape of a snipped prism. The prism thickness is 16 nm. Results are based on DDA calculations with a 2-nm cubic grid. For snip = 0, 68 704 dipoles are used in the calculation. Reprinted with permission from Ref. ¹⁶. Copyright © 2003 American Chemical Society. (c-e) silver nanoparticles with irregular shapes can be converted to silver nanoplates in the presence of H_2O_2 . (f) Digital image of silver nanoplates prepared in the presence of glycerol by tuning the synthetic conditions. Reprinted with permission from Ref. ²¹. Copyright © 2011 American Chemical Society.

1.3 Dynamic Tuning of Photonic Properties

Instantaneous and reversible tuning of the photonic property of metal nanostructures holds great promises for developing novel optoelectronic devices and more effective chemical and biomedical sensors by allowing instant selective excitation or quenching of specific plasmon modes.

The dynamic tuning of photonic property could be realized by the plasmon coupling between neighboring Au nanoparticles, which can be achieved through the reversible assembly and disassembly of Au nanoparticle chain-like structures. Either internal or external stimuli could control the interactions between adjacent particles. For example, our previous results demonstrate that remaining salt in conjunction with ethanol, instead of ethanol itself, induces the assembly of gold nanoparticles in ethanol. In the absence of salt, gold nanoparticles can be well dispersed in an ethanol solution (Figure 1.7 a & b).²⁷ External stimuli, such as temperature, could also be used to trigger the assembly and disassembly. Figure 1.7 c and d show that thermoresponsive assembly and disassembly of charged AuNPs could be realized through the manipulation of the electrostatic interactions by temperature variation. Thus the dynamic and reversible tuning of the surface plasmon coupling could be achieved by controlling the temperature of the solution.²⁴

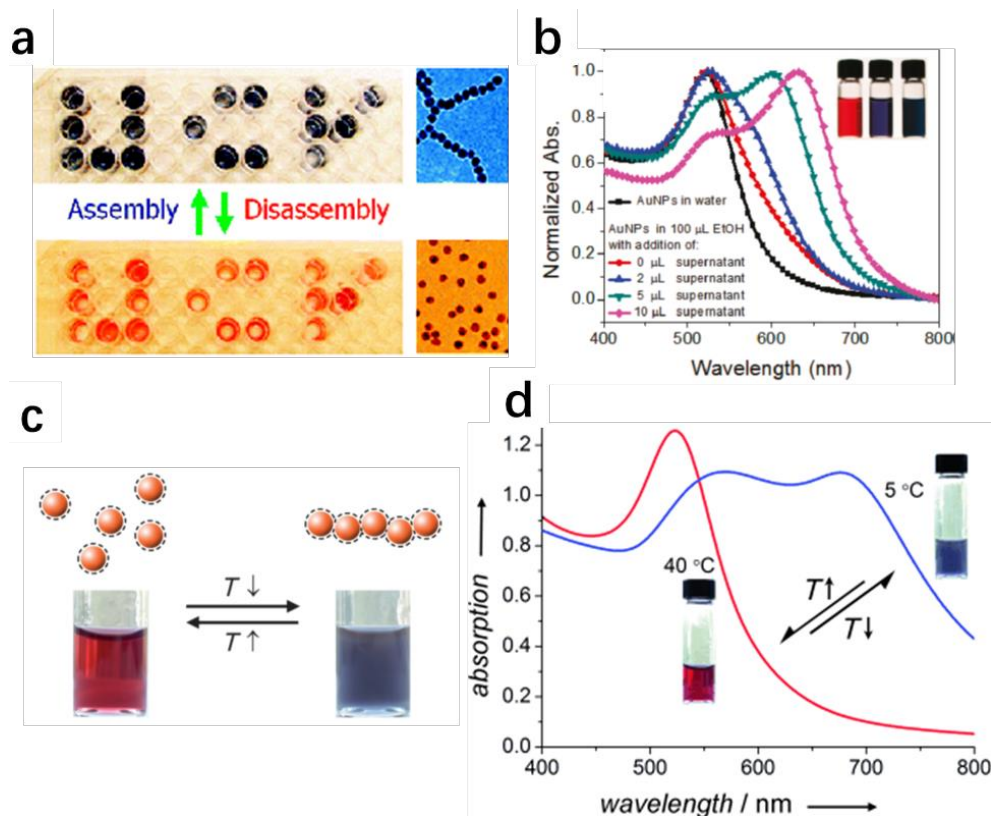


Figure 1.7 Plasmon coupling between neighboring Au nanoparticles (AuNPs). (a, b) Role of salt in the spontaneous assembly of charged gold nanoparticles in ethanol. (a) Digital images and TEM images showing the assembly and disassembly of gold nanoparticles. (b) Normalized UV-vis extinction spectra of dispersions of centrifuged AuNP precipitation in EtOH (100 μL) with the addition of different volumes of the supernatant of the original synthesis solution (0, 2, 5, 10 μL). Reprinted with permission from Ref. ²⁷. Copyright © 2011 American Chemical Society. (c, d) The thermoresponsive tuning of plasmonic properties of charged colloidal AuNPs: AuNPs switching between the disassembled and assembled states in response to temperature changes. Reprinted with permission from Ref. ²⁴. Copyright © 2012 John Wiley and Sons.

We have created magnetically tunable photonic nanostructures by magnetically controlled assembly of superparamagnetic nanocrystal clusters into one-dimensional photonic crystals or incorporating magnetic actuation into noble metal nanostructures to achieve active tuning of plasmonic properties. As shown in Figure 1.8, when applying an external magnetic field, the superparamagnetic nanocrystal clusters could form periodic chains, which could show bright structure color. Slight changes in the field strength can lead to the destruction of the original equilibrium and reconstruction of a new equilibrium, and thus changes the interparticle separation and the periodicities of chain-like structures.²⁸ The magnetic-responsive photonic nanostructures can also be achieved by controlling the orientation of anisotropic noble metal nanostructures such as Au nanorods, using external magnetic fields (Figure 1.8 f & g).¹⁸ Detailed discussion for this example could be found in section 3.1.

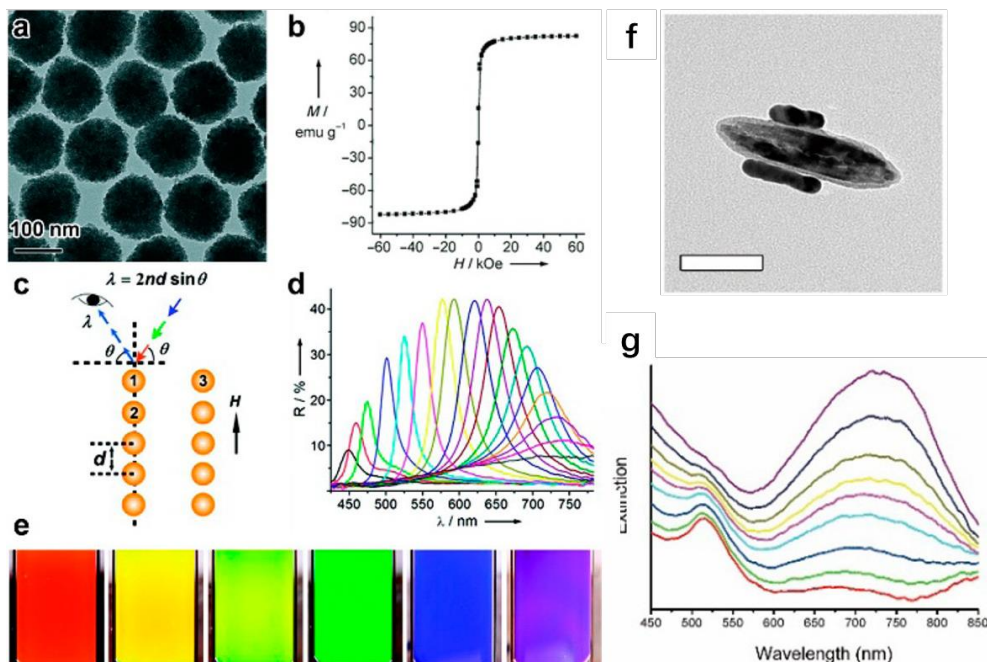


Figure 1.8 Magnetically tunable photonic property. (a-e) Magnetically controlled assembly of superparamagnetic nanocrystal clusters into one-dimensional photonic crystals. (a, b) Representative TEM image and magnetic hysteresis loop. (c) Scheme of Bragg diffraction from the 1D chain-like structures assembled from the building blocks. (d) Reflectance spectra of an aqueous dispersion of chain-like structures under magnetic fields with different strengths. (e) Digital photos of an aqueous dispersion of one typical nanocluster sample encapsulated in a capillary tube with a width of 1 cm under magnetic fields with increasing strengths from left to right. Reproduced with permission from ref²⁸. Copyright 2016 American Chemical Society. (f, g) Magnetic tuning of plasmonic excitation of gold nanorods. (f) TEM image of the as-assembled $\text{Fe}_3\text{O}_4/\text{Au}$ NR structure. Scale bar: 100 nm. (g) From top to bottom: spectra of a dispersion of the hybrid nanostructures when changing the angle between the long axis of the nanorods and the polarization direction from 0° to 90° . Reprinted with permission from Ref.¹⁸. Copyright © 2013 American Chemical Society.

1.4 The Scope of This Dissertation

Anisotropic properties of both magnetic and plasmonic nanostructures make them interesting research topics, as the shape anisotropy of the magnetic nanorods could be used to control their orientation and that of the plasmonic nanostructures attached to them. Thus, by applying an external magnetic field, instantaneous and reversible tuning of the plasmonic property of anisotropic metal nanostructures could be achieved. This holds great promises for developing novel optoelectronic devices and effective chemical and biomedical sensors. This dissertation discusses our efforts in the synthesis and application of magnetic/plasmonic anisotropic nanostructures.

Chapter 1 is the introduction to anisotropic magnetic/plasmonic nanostructures. First, magnetism and magnetic anisotropy (especially shape anisotropy) will be discussed. Due to the shape anisotropy and ferromagnetic/ferrimagnetic nature, the orientation of the magnetic nanorods could be efficiently controlled by applying an external magnetic field. Then, anisotropic plasmonic nanostructures will be generally introduced. At last, we will talk about the commonly used strategy for dynamic tuning of photonic properties.

Starting from Chapter 2, we will introduce our work regarding the synthesis of anisotropic magnetic iron oxide nanorods. First, uniform nonmagnetic β -FeOOH nanorods with different sizes and aspect ratios were synthesized by the hydrolysis of FeCl_3 . Parameters influencing the synthesis, such as the concentration of reagents, different ligands, and temperature, were systematically studied. The indirect synthesis of magnetic iron oxide nanorods was achieved by a post-reduction method. Based on the reaction medium and the surface modification, we classify the post-reduction methods

into (1) Solution phase polyol reduction; (2) Solid phase hydrogen reduction and (3) Solid phase carbothermal reduction.

Then we successfully synthesized the anisotropic magnetic/plasmonic Fe_3O_4 NRs@ SiO_2 @Au core-shell nanocomposites by combining a post-reduction and a seeded growth method. The nanocomposites exhibited angle-dependent plasmonic property. Chapter 3 will focus on the potential application of the magnetic/plasmonic nanocomposites. First, we demonstrated the nanocomposites array, when fixed inside a polymer film, could find unique applications for information encryption. In particular, we have fabricated a six-column nanocomposite array film and demonstrate that it could realize multi-level information encryption. We believe that with more orientation control over the fixed nanocomposites and more complicated encoding and decoding methods, the information encryption security could be significantly improved. Furthermore, taking advantage of the instantaneous tuning over the orientation of the nanocomposites in solution, we extended the working principle and fabricated a new type of magnetic field direction sensor. An actuator system which consists of the sensor and a MeArm base servo motor vividly showed the performance of the sensing ability.

Finally, we demonstrated that the confined growth of gold and silver nanorods within RF could be realized by using β -FeOOH nanorods as a sacrificial template through a seeded growth method. The RF shell is flexible and stretchable, due to its polymer nature, which offers more size tunability within one Au seed@RF template. At the same time, partially reduced Fe_xO_y @RF could serve as the reducing agent, and facilitate the

gold shell formation between Fe_xO_y nanorod and RF layer. More efforts should be put into the investigation of formation mechanism and optimization of the shell quality.

1.5 References

- (1)Sun, C.; Lee, J. S. H.; Zhang, M. *Adv. Drug Delivery Rev.* **2008**, 60, 1252-1265.
- (2)Shin, T.-H.; Choi, Y.; Kim, S.; Cheon, J. *Chem. Soc. Rev.* **2015**, 44, 4501-4516.
- (3)Mornet, S.; Vasseur, S.; Grasset, F.; Duguet, E. *J. Mater. Chem.* **2004**, 14, 2161-2175.
- (4)Frey, N. A.; Peng, S.; Cheng, K.; Sun, S. *Chem. Soc. Rev.* **2009**, 38, 2532-2542.
- (5)He, L.; Wang, M.; Ge, J.; Yin, Y. *Acc. Chem. Res.* **2012**, 45, 1431-1440.
- (6)Reiss, G.; Hütten, A. *Nat. Mater.* **2005**, 4, 725.
- (7)Ambashta, R. D.; Sillanpää, M. *J. Hazard. Mater.* **2010**, 180, 38-49.
- (8)Tang, S. C. N.; Lo, I. M. C. *Water Res.* **2013**, 47, 2613-2632.
- (9)Wang, M.; He, L.; Zorba, S.; Yin, Y. *Nano Lett.* **2014**, 14, 3966-3971.
- (10)Wang, M.; He, L.; Xu, W.; Wang, X.; Yin, Y. *Angew. Chem., Int. Ed.* **2015**, 54, 7077-7081.
- (11)O'handley, R. C. *Modern magnetic materials: principles and applications*; Wiley, **2000**.
- (12)Krahne, R.; Manna, L.; Morello, G.; Figuerola, A.; George, C.; Deka, S. *Physical Properties of Nanorods*; Springer, **2013**.
- (13)Bødker, F.; Mørup, S.; Linderöth, S. *Phys. Rev. Lett.* **1994**, 72, 282.
- (14)Bedanta, S.; Kleemann, W. *J. Phys. D: Appl. Phys.* **2009**, 42, 013001.
- (15)Cullity, B. D.; Graham, C. D. *Introduction to magnetic materials*; John Wiley & Sons, **2011**.
- (16)Kelly, K. L.; Coronado, E.; Zhao, L. L.; Schatz, G. C. *J. Phys. Chem. B* **2003**, 107, 668-677.
- (17)Li, N.; Zhao, P.; Astruc, D. *Angew. Chem., Int. Ed.* **2014**, 53, 1756-1789.
- (18)Wang, M.; Gao, C.; He, L.; Lu, Q.; Zhang, J.; Tang, C.; Zorba, S.; Yin, Y. *J. Am. Chem. Soc.* **2013**, 135, 15302-15305.
- (19)Murphy, C. J.; Sau, T. K.; Gole, A. M.; Orendorff, C. J.; Gao, J.; Gou, L.; Hunyadi, S. E.; Li, T. *J. Phys. Chem. B* **2005**, 109, 13857-13870.
- (20)Chen, H.; Shao, L.; Li, Q.; Wang, J. *Chem. Soc. Rev.* **2013**, 42, 2679-2724.

- (21)Zhang, Q.; Li, N.; Goebel, J.; Lu, Z.; Yin, Y. *J. Am. Chem. Soc.* **2011**, 133, 18931-18939.
- (22)Pérez-Juste, J.; Rodríguez-González, B.; Mulvaney, P.; Liz-Marzán, L. M. *Adv. Funct. Mater.* **2005**, 15, 1065-1071.
- (23)Ou, J.-Y.; Plum, E.; Zhang, J.; Zheludev, N. I. *Nat. Nanotechnol.* **2013**, 8, 252.
- (24)Liu, Y.; Han, X.; He, L.; Yin, Y. *Angew. Chem., Int. Ed.* **2012**, 51, 6373-6377.
- (25)Huang, X.; El-Sayed, M. A. *J. Adv. Res.* **2010**, 1, 13-28.
- (26)Wang, G.; Tao, S.; Liu, Y.; Guo, L.; Qin, G.; Ijima, K.; Maeda, M.; Yin, Y. *Chem. Commun.* **2016**, 52, 398-401.
- (27)Han, X.; Goebel, J.; Lu, Z.; Yin, Y. *Langmuir* **2011**, 27, 5282-5289.
- (28)Wang, M.; Yin, Y. *J. Am. Chem. Soc.* **2016**, 138, 6315-6323.

Chapter 2 Indirect Synthesis of Magnetic Iron Oxide Nanorods

2.1 Introduction

As introduced in section 1.1, shape anisotropy plays an important role in magnetic anisotropy. For example, the coercivity (H_c) of iron particles with an aspect ratio of 10 is almost 13 times to that of particles with an aspect ratio of 1.1 (See Figure 2.1b).¹ H_c is strictly related to the anisotropic energy barrier that must be overcome to invert the direction of the magnetic dipoles of the material. So, one focus of the proposed research is to synthesize anisotropic nanorods with different aspect ratio, as well as the control of the size, morphology, and quality.

Some approaches have been reported to produce magnetic nanoparticles,^{1,2} among which, co-precipitation is the preferred route regarding simplicity of the synthesis, but the shape control is not so good. Thermal decomposition method could control the size and morphology, but the synthesis process is complicated and requires organic solvents, which makes it more complicated and time-consuming for the washing step and also surface modification.³ For other methods, such as micro-emulsion and hydrothermal synthesis, the yield of the reaction is relatively low and not scalable.¹

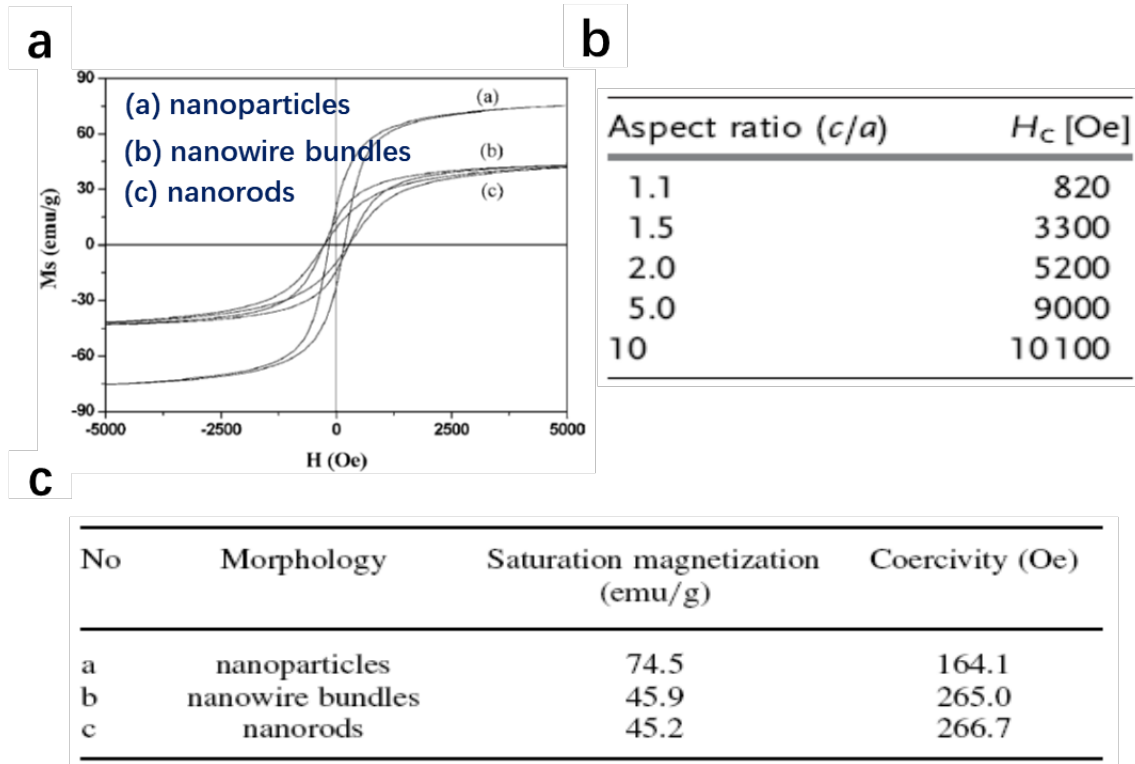


Figure 2.1 (a, c) Morphology and magnetic properties of the as-prepared Fe_3O_4 nanostructures. Reprinted with permission from Ref. ⁴. Copyright © 2007 Springer. (b) The influence of the shape of iron particles on the coercivity. Reprinted with permission from Ref. ¹. Copyright © 2007 John Wiley and Sons.

For the synthesis of anisotropic magnetic nanomaterials, there are mainly two methods. The first one is hydrolysis of the iron precursor, the shape of the synthesized materials could be controlled by additives such as urea⁵ and diamine hydrate⁶. The other method is magnetic field induced growth.^{7,8} The applied external magnetic field may induce orientate growth of nanorods or self-assembly of nanoparticles to chain-like structures. Without a magnetic field, to get pure magnetite nanorods, it is important to keep the initial reagent molar ratio of $\text{Fe}^{3+}/\text{Fe}^{2+}$ as 2:1. If the molar ratio was above 2, the impurity of Fe_2O_3 would appear in the final product due to hydrolysis of the excessive Fe^{3+} ions. For magnetic induced synthesis, there are several disadvantages. Self-made reaction cells with a magnet under them are usually employed, which leads inhomogeneous distribution of magnetic field and thus influence the size distribution or aspect ratio of the synthesized nanorods. Moreover, it is also difficult to scale up to a relatively large scale due to the homemade experiment setup. Since the magnetic nanorods are not paramagnetic, the existence of an external magnetic field may result in some degree of aggregation (Figure 2.2).⁸

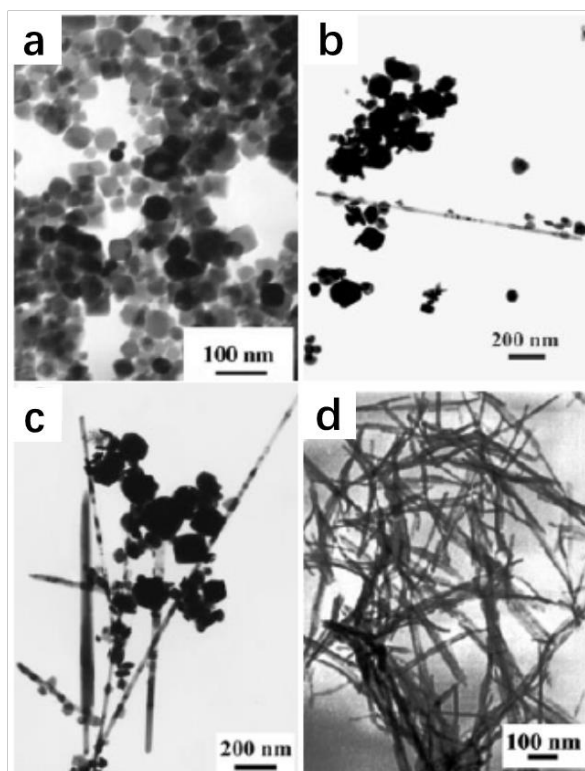


Figure 2.2 Magnetic field induced synthesis of magnetic nanowires. TEM images of the samples obtained in zero magnetic field (a), and 0.15 T (b), 0.25 T (c), and 0.35 T (d) magnetic fields. Reprinted with permission from Ref. ⁸. Copyright © 2013 John Wiley and Sons.

For almost any application of magnetic nanomaterials, the chemical stability is critical, especially for pure metals, such as Fe, Co, Ni and their metal alloys, which are very sensitive to air. Several strategies to improve the chemical stability of magnetic nanoparticles were developed, including surface passivation by mild oxidation, surfactant and polymer coating, precious-metal coating, silica and carbon coating. Among which, silica coating is relatively stable under aqueous condition, and the coating process is easy. Also the thickness of the coating layer could be varied through adjusting of the concentration of ammonium and amount of tetraethoxysilane (TEOS) added.⁹ After silica coating, the surfaces of coated nanoparticles are ready to be modified with other functional groups due to the existence of a large amount of hydroxyl groups. Most recently, a general sol-gel process has been developed to form a coating of resorcinol-formaldehyde (RF) resin on inorganic nanostructures of various compositions and morphologies. The RF shell can be conveniently converted into carbon through high-temperature carbonization under an inert atmosphere.¹⁰

Based on the above introduction, we propose the indirect strategy for the synthesis of iron oxide-based magnetic nanorods.¹¹⁻¹³ Briefly, as shown in Figure 2.3d, nonmagnetic hematite (α -Fe₂O₃) or akaganéite (β -FeOOH) nanorods with different sizes and aspect ratios will be first synthesized. Then different surface modification (polymer ligands or silica) will be coated on the surface of synthesized materials, render the well dispersibility in both ethanol and aqueous solution. After that, the core-shell materials will be then reduced through a post-reduction method, resulting in the magnetic nanorods.

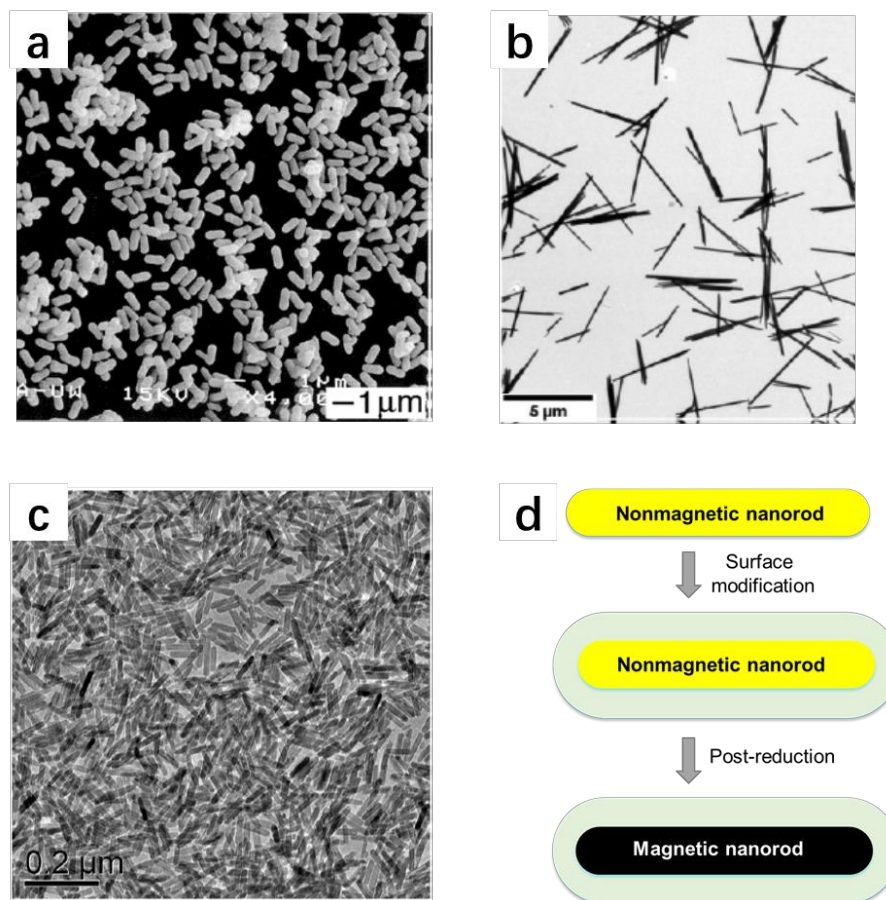


Figure 2.3 Indirect synthesis of magnetic nanorods. (a) An SEM image of the ellipsoidal colloids of hematite. Reprinted with permission from Ref. ¹⁴. Copyright © 2001 John Wiley and Sons. (b) TEM image of large akaganéite needles. Reprinted with permission from Ref. ¹⁵. Copyright © 2012 American Chemical Society. (c) TEM images of small akaganéite nanorods. Reprinted with permission from Ref. ¹⁶. Copyright © 2008 Nature Publishing Group. (d) Schematic illustration of the indirect synthesis of magnetic nanorods strategy.

2.2 Materials and Methods

2.2.1 Materials

Iron(III) chloride hexahydrate ($\text{FeCl}_3 \cdot 6\text{H}_2\text{O}$), iron(III) chloride, anhydrous salt (FeCl_3), polyacrylic acid (PAA, average M.W. 1800), tetraethyl orthosilicate (TEOS), diethylene glycol (DEG), cetrimonium bromide (CTAB), cetrimonium chloride (CTAC), resorcinol (R), formaldehyde (HCHO) were purchased from Sigma-Aldrich. $\text{NH}_3 \cdot \text{H}_2\text{O}$ solution (28%), HCl (fume, 37%), NaCl were purchased from Fisher Scientific. Ethanol (200 proof) was purchased from Decon Laboratories Inc. Polyvinylpyrrolidone (PVP, K12, average M.W. 3500) was purchased from Acros Organics. All the chemicals were used as received.

2.2.2 Synthesis of Nonmagnetic β -FeOOH Nanorods

For a typical synthesis of β -FeOOH nanorods, 20 mL of 0.1 M $\text{FeCl}_3 \cdot 6\text{H}_2\text{O}$ solution and 0.5 g CTAB were placed in a small glass vial with cap. Then the solution was aged in an oven at 87°C for 24 hours. Afterward, the mixture was cooled down to room temperature, and the particles were washed several times with distilled water. Several parameters could be changed to the synthesis procedure. This synthesis could be scaled up to 200 mL.

(1) Concentration of $\text{FeCl}_3 \cdot 6\text{H}_2\text{O}$

To investigate the concentration effect of the iron precursor, concentration of $\text{FeCl}_3 \cdot 6\text{H}_2\text{O}$ solution varies from 0.1 M all the way to 0.6 M, while the other parameters remain the same. All the samples contain 0.5 g of CTAB as the surfactant.

(2) Concentration of HCl

To investigate the concentration effect of HCl, different amount of HCl was added to the reaction mixture to reach the desired HCl concentration, e.g., 0.01 M to 0.07 M. All the other parameters remain the same.

(3) Concentration of surfactants

To investigate the concentration effect of surfactants, different amount of CTAB or CTAC was added to the reaction mixture, while all the other parameters, such as the concentration of $\text{FeCl}_3 \cdot 6\text{H}_2\text{O}$ or concentration of HCl, remain the same.

For the synthesis of 2 μm FeOOH nanorods, a 200-mL solution of 0.6 M FeCl_3 and 0.07 M HCl was prepared in a 200-mL Pyrex bottle. The solution was first centrifuged at 11000 rpm for 10 min to remove impurities. Then the solution mixture was aged in an oven at 98°C for 24 hours. Afterward, the mixture was cooled under a running tap water, and the particles were washed several times with distilled water.

2.2.3 Post-reduction Method to Form Magnetic Nanorods

Based on the reaction medium and the surface modification, we classify the post-reduction methods into (1) Solution phase polyol reduction; (2) Solid phase hydrogen reduction and (3) Solid phase carbothermal reduction.

(1) Solution phase polyol reduction

Before the reduction, the as-synthesized $\beta\text{-FeOOH}$ nanorods were first modified with PAA. Typically, the pH of 0.1 M PAA solution (7.2 g/L, the concentration was calculated by the monomer) was first adjusted to 8-9 by adding 28% $\text{NH}_3 \cdot \text{H}_2\text{O}$ solution. To 40 mL of the above PAA solution, 40 mL of the $\beta\text{-FeOOH}$ nanorods (9 mg/mL) was

added, and the mixture solution was stirred overnight. After three times of washing with water, PAA modified nanorods (β -FeOOH-PAA) were dispersed in water.

For polyol reduction, an aqueous dispersion of the β -FeOOH-PAA nanorods was injected into diethylene glycol (DEG) solution preheated at 220 °C in a 3-neck flask. After refluxing for desired reaction time, typically 8 h, the solution was first cooled down to room temperature. Then 1.5 times more of ethanol was added to the flask, and the mixture was centrifuged and then washed with water.

(2) Solid phase hydrogen reduction

Before hydrogen reduction, the nanorods were first coated with silica. Typically, 40 mg nanorods were re-dispersed into 3 mL DI water. 1.0 mL of ammonia solution was then added, followed by the addition of 20 mL ethanol (200 proof) and 100 μ L of TEOS. The amount of TEOS could be adjusted to tune the silica coating thickness. After incubation for 30 min, the silica-coated nanorods were then collected by centrifugation, washed with water for several times and re-dispersed in water.

For the reduction, nanorods with different thickness of silica coating were first dried in an oven; then the solids were transferred to the porcelain combustion boats. After two hours of reduction at 360 °C in the tubular furnace with forming gas (5% H₂ and 95% N₂), the resulting black powders were then dispersed into DI water for further use. The reaction temperature and time, as well as the composition of the gas, could be adjusted to yield other products.

(3) Solid phase carbothermal reduction

Before the carbothermal reduction, the nanorods were first coated with a layer of resorcinol-formaldehyde resin. Typically, 20 mg of β -FeOOH-PAA nanorods were dispersed into 56 mL DI water. Then 50 mg resorcinol and 70 μ L formaldehyde were added. The mixture was heated up to 60 °C in a 3-neck flask. Then 40 μ L of ammonia solution (28%) was added. The mixture was then reacted for another 2 h. The RF coated nanorods (β -FeOOH@RF) were then collected by centrifugation, washed with water for several times and dried in an oven.

For carbothermal reduction, β -FeOOH@RF nanorods were first transferred to the porcelain combustion boats. After two hours of calcination under nitrogen gas in the tubular furnace, the resulting black powders were then dispersed into DI water for further use. The reaction temperature could be adjusted from 400 °C to 600°C.

2.2.4 Magnetophoresis Performance of Magnetic Nanorods

2 μ m β -FeOOH nanorods were first coated with a thin layer of silica, then reduced to magnetic through the polyol reduction method. Typically, for silica coating, 9 mg nanorods were re-dispersed into 3 mL DI water. 1 mL of ammonia solution was then added, followed by the addition of 20 mL ethanol (200 proof) and different amount of TEOS. After 30 min of reaction, the silica-coated nanorods were collected by centrifugation, washed with water for several times and redispersed in DI water. For the synthesis of end-etched nanorods, silica coated nanorods were first mixed with 0.5 M oxalic acid and refluxed at 60 °C for a different time, e.g., 3 h, 5 h, and 7 h. Then similar polyol reduction method was used to transfer them to magnetic.

The as-synthesized magnetic nanorods (both with and without oxalic acid etching) were first dispersed in water or buffer solution, and the magnetophoresis performance was tested by placing the nanorods solution near a permanent magnet. For better measurement of the magnetophoresis behavior, the magnetic nanorods were first put into the cuvette, and a permanent magnet was placed near the cuvette (Figure 2.18a inset). The real-time transmittance of the solution at 600 nm was measured by UV-Vis spectrometer.

2.3 Results and Discussion

2.3.1 Synthesis of Nonmagnetic β -FeOOH Nanorods

β -FeOOH Nanorods were synthesized by the hydrolysis of FeCl_3 . Figure 2.4 shows the TEM images of FeOOH nanorods synthesized with different concentration of HCl. When there is no HCl added to the reaction mixture, it also results in ellipsoidal nanorod (Figure 2.4 a). The size of the nanorod is 425.1×79.5 nm, with an aspect ratio of 5.3. When increasing the concentration of HCl from 0.01 M all the way to 0.07 M, all the products show very uniform nanorod structure, but with increasing aspect ratio. Starting from about 0.03 M HCl, the ends of the nanorods become flat, and the nanorods become more cylindrical, other than ellipsoidal. As shown in Table 2.1, with increasing concentration of HCl, the length of the nanorods gradually increases and the width of the nanorods gradually decreases, thus results in increased aspect ratio, which is consistent with the previous report.¹⁷ The largest aspect ratio of the nanorods that we synthesized is 31.6. Further increasing the concentration of HCl to 0.08 M, we got a clear solution, indicating there is no nanorods formed. Also, it is worth noting that, with the increasing of the HCl concentration, the yield of the products becomes lower. For all the synthesis in this group, we added CTAB as a surfactant. For the function of CTAB, we will discuss more about it later.

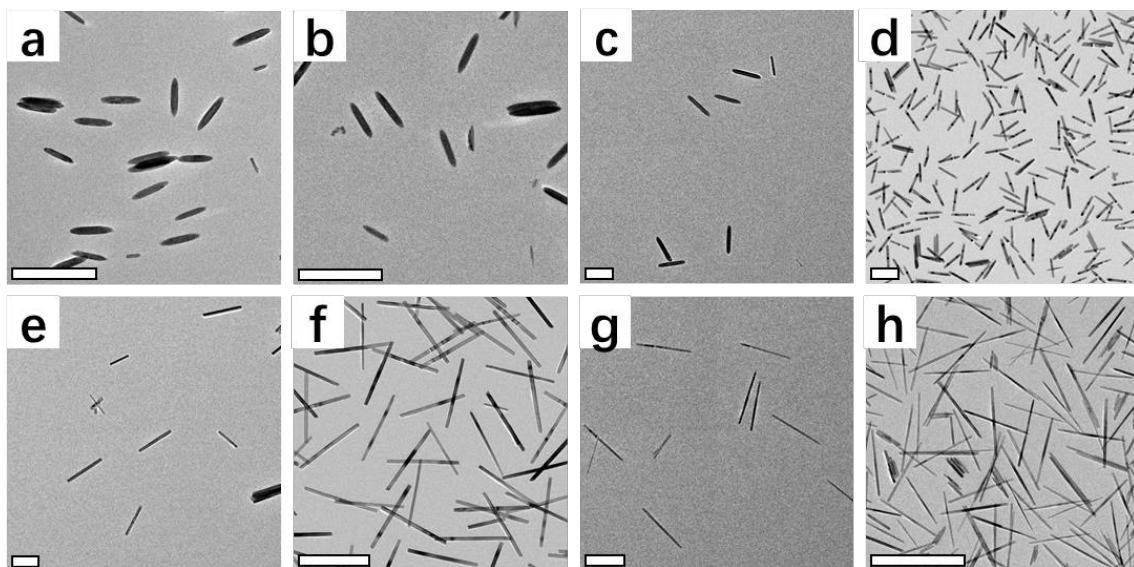


Figure 2.4 TEM images of FeOOH nanorods synthesized with different concentration of HCl. (a) Without adding of HCl. (b-h) With 0.01 M (b), 0.02 M (c), 0.03 M (d), 0.04 M (e), 0.05 M (f), 0.06 M (g) and 0.07 M (h) HCl. Scale bars are 500 nm.

Table 2.1 Size and aspect ratio evolution with different concentration of HCl.

HCl (M)	CTAB (g)	Length (nm)	Width (nm)	Aspect Ratio
0	0.5	425.1	79.5	5.3
0.01	0.5	471.1	82.1	5.7
0.02	0.5	490.5	69.6	7.0
0.03	0.5	365.0	38.4	9.5
0.04	0.5	640.9	51.5	12.4
0.05	0.5	477.6	24.3	19.7
0.06	0.5	580.1	21.0	27.6
0.07	0.5	320.0	10.1	31.6

Since when increasing the concentration of HCl, the aspect ratio increases, we thought the existence of H^+ and Cl^- both contribute to it. As for H^+ , it could react with the FeOOH nanorods, and realize the etching effect. We observed that when increasing the concentration of HCl, the ends of the nanorods become flat and irregular. For Cl^- , it could adsorb on the crystalline surface of the nanorod to direct its growth.¹⁷

To further verify the function of HCl, we investigate the effect when increasing the concentration of $\text{FeCl}_3 \cdot 6\text{H}_2\text{O}$. As shown in Figure 2.5, when increases the concentration of $\text{FeCl}_3 \cdot 6\text{H}_2\text{O}$ to 0.2 M, compared to 0.1M, the aspect ratio of the nanorods becomes larger, but the width of the nanorods does not change obviously. Further increasing the concentration of $\text{FeCl}_3 \cdot 6\text{H}_2\text{O}$ all the way to 0.6 M, the effect becomes more obvious. As we could see from the TEM images, the nanorods become longer and longer, while the width does not change obviously so that the aspect ratio of the nanorods increases.

Based on the above results, we confirm the function of Cl^- . Since when increasing the concentration of Cl^- in the reaction mixture, it results in increasing aspect ratio. However, it is also apparent that even when the concentration of $\text{FeCl}_3 \cdot 6\text{H}_2\text{O}$ increases to 0.6 M, the aspect ratio remains at about 10. This indicates that HCl plays a unique role in controlling the aspect ratio of the nanorods. We could also conclude that it is almost impossible to get the longer and “fatter” nanorods only by increasing the concentration of $\text{FeCl}_3 \cdot 6\text{H}_2\text{O}$.

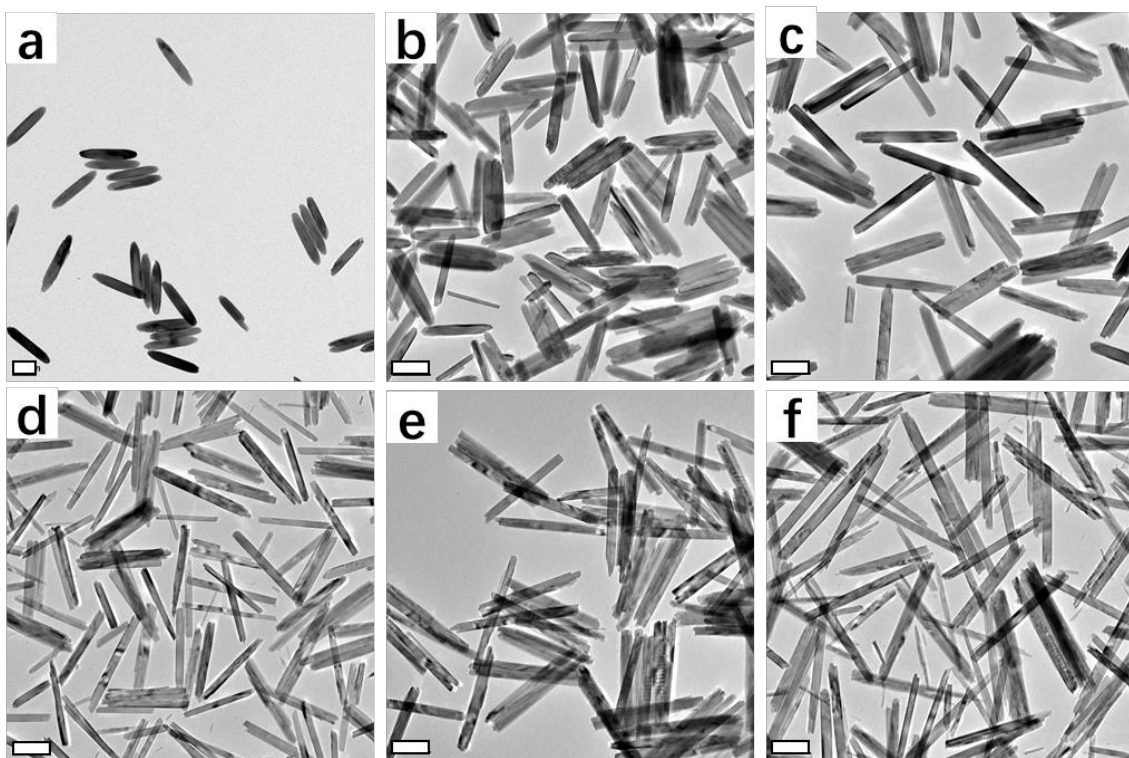


Figure 2.5 (a) TEM images of FeOOH nanorods synthesized with different concentration of FeCl₃·6H₂O. (a) 0.1 M (b) 0.2 M (c) 0.3 M (d) 0.4 M (e) 0.5 M (f) 0.6 M. Scale bars are 200 nm.

As mentioned above, during the synthesis, we added CTAB as the surfactant. To investigate the function or influence of CTAB, we varied the amount of CTAB added to the reaction mixture during the synthesis. As shown in Figure 2.6, when there is no CTAB added, the synthesis also results in FeOOH nanorods (Figure 2.6 a-d). Moreover, by varying the concentration of HCl, it shows the similar trend, as compared to that with 0.5 g CTAB (Figure 2.6 e-h). Also, for the synthesis without CTAB, the dispersibility of the nanorods is still good. When carefully compared the size and aspect ratio, and found that CTAB would limit the growth of the nanorods, especially in the length direction. Moreover, for all the four concentrations of HCl investigated, we observed decrease aspect ratio when CTAB was added as the surfactant.

When further double the amount of CTAB from 0.5 g to 1.0 g, the size limiting effect is more apparent. As shown in Figure 2.6 i & j, for both cases without and with 0.04 M of HCl, the size of the nanorods becomes obvious smaller. For the case without HCl, the length of the nanorods decreased from 425.1 nm to 157.3 nm, which is even less than half of its original size. At the same time, the width decreased from 79.5 nm to 32.4 nm. Overall, the aspect ratio decreased from 5.3 to 4.9. While for the case with 0.04 M HCl, when 1.0 g CTAB was added, the width does not change much, but the length decreased from 640.9 nm to 499.5 nm, which indicates the size limitation effect in the length direction is stronger.

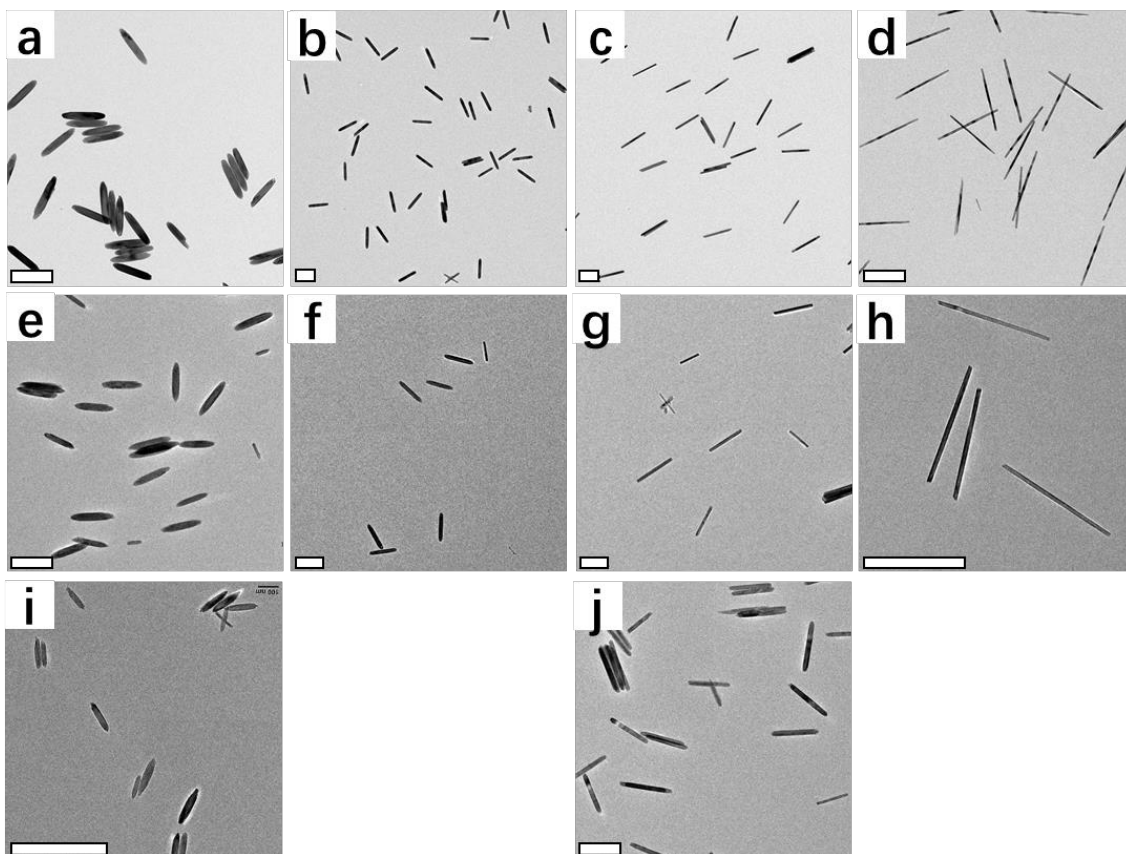


Figure 2.6 Effect of concentration of CTAB. (a-d) TEM images of FeOOH nanorods synthesized without CTAB, and with different concentration of HCl: With 0 M(a), 0.02 M (b), 0.04 M (c), and 0.04 M (d) HCl. (e-h) TEM images of FeOOH nanorods synthesized with 0.5 g of CTAB, and with different concentration of HCl: With 0 M(e), 0.02 M (f), 0.04 M (g), and 0.04 M (h) HCl. (i, j) TEM images of FeOOH nanorods synthesized with 1.0 g of CTAB, and with different concentration of HCl: With 0 M(i), and 0.04 M (j) HCl. Scale bars are 500 nm.

Table 2.2 Size and aspect ratio evolution with different concentration of CTAB.

HCl (M)	CTAB (g)	Length (nm)	Width (nm)	Aspect Ratio
0	0	440.3	79.2	5.6
0	0.5	425.1	79.5	5.3
0	1.0	157.3	32.4	4.9
0.02	0	488.6	66.5	7.3
0.02	0.5	490.5	69.6	7.0
0.04	0	630.8	48.4	13.0
0.04	0.5	640.9	51.5	12.4
0.04	1.0	499.5	53.1	9.4
0.06	0	688.5	22.9	30.1
0.06	0.5	580.1	21.0	27.6

Other than CTAB, we also explored the effect of another surfactant, CTAC. Since it has a very similar structure with CTAB, but instead of Br^- , it contains Cl^- as the anion. As shown in Figure 2.7, compared with no additive (Figure 2.7a), when 0.01 M CTAC was added, the reaction still produces ellipsoidal nanorods, but with a dramatically decreased size (Table 2.3). Since the length decreased from 440 nm to 254 nm, while the change in width is not apparent, so that the aspect ratio decreased from 5.6 to 3.8. When increasing the concentration of CTAC to 0.08 M, the aspect ratio decreased to even 1.5. Thus the morphology is more like spherical particles. Interestingly, starting from 0.02 M CTAC, the width of the nanorods gradually increased, this also contributes to the decrease of the aspect ratio. Further increasing the concentration of CTAC to 0.16 M, we got some irregularly shaped nanoclusters within 100 nm. This also demonstrates the size limiting effect of the surfactant, as well as the chloride anion.

When 0.5 g CTAB was added as the surfactant, the concentration of CTAB is about 0.07 M. When 0.08 M of CTAC was added, it almost produces quasi-spherical nanoparticles. We thought this might be due to the combined effect of the CTA^+ cation and the Cl^- anion. So that we designed the following control experiment to verify it.

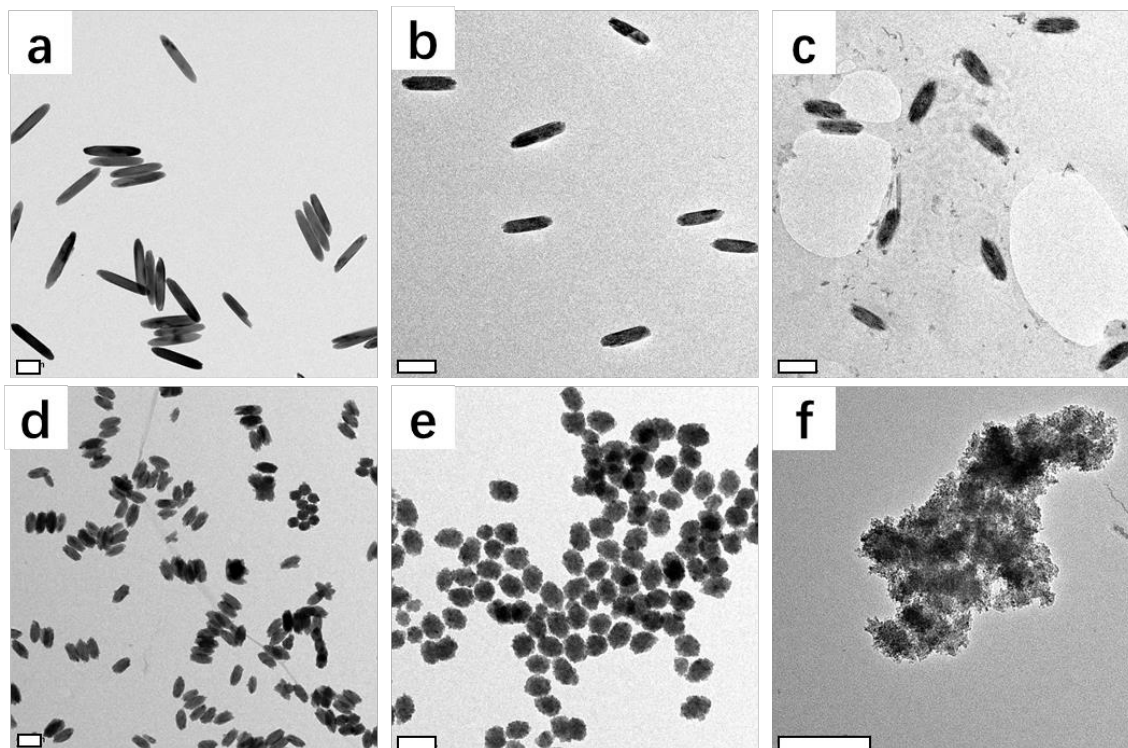


Figure 2.7 Effect of concentration of CTAC. TEM images of FeOOH nanorods synthesized with different concentration of CTAC: With 0 M(a), 0.01 M (b), 0.02 M (c), 0.04 M (d), 0.08 M (e), and 0.16 M (f) of CTAC. Scale bars are 200 nm.

Table 2.3 Morphology and size evolution when changing the concentration of CTAC

CTAC (M)	Length (nm)	Width (nm)	Aspect Ratio
0	440	79	5.6
0.01	254	68	3.8
0.02	226	81	2.5
0.04	162	86	1.9
0.08	135	92	1.5
0.16	Nanocluster < 100 nm		

We tried to use both CTAB and NaCl to replace CTAC, since the combination of CTAB and NaCl could provide both the CTA^+ cation and Cl^- anion. As shown in Figure 2.8 and summarized in Table 2.4, when both CTAB and NaCl were added as the surfactants, it still resulted in ellipsoidal nanorods. Even though the size decreased a lot compared to the control samples, but the aspect ratio did not change much. When only NaCl was added, we could also see the size limiting effect, most probably due to the existence of extra Cl^- . So that we could conclude when both CTAB and NaCl were added, the combined size limiting effect leads to the dramatically decreased size of the nanorods. However, it will not produce quasi-spherical nanoparticles, which is different from our expectation. This also demonstrates the specificity of CTAC as the surfactant, as well as the morphology controller.

Based on all the above understanding regarding CTAC, we then tried to adjust the concentration of $\text{FeCl}_3 \cdot 6\text{H}_2\text{O}$ and CTAC, and try to get the spherical FeOOH nanoclusters. As shown in Figure 2.9c, when 0.2 M $\text{FeCl}_3 \cdot 6\text{H}_2\text{O}$ and 0.08 M CTAC were used for the synthesis, it resulted in almost spherical nanoparticles.

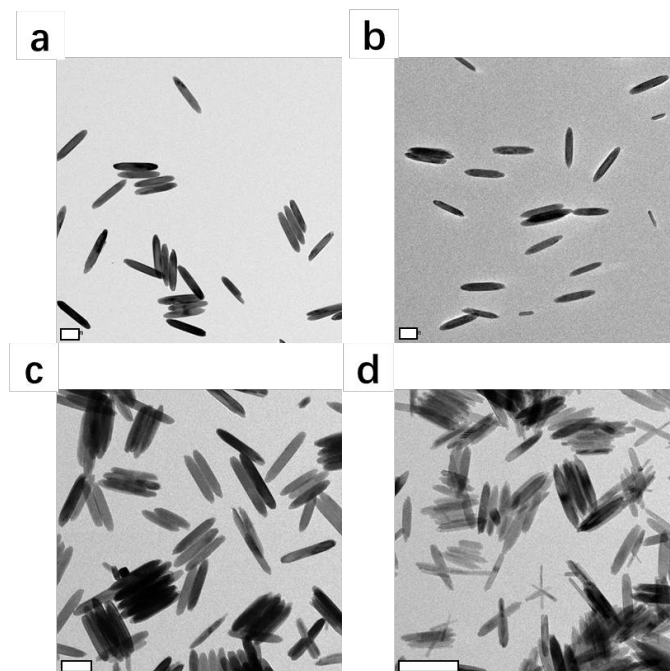


Figure 2.8 FeOOH nanorods synthesized with different surfactants (a) With no surfactant. (b) With 0.5 g of CTAB. (c) With 0.08 M NaCl. (d) With 0.5 g of CTAB and 0.08 M of NaCl. Scale bars are 200 nm.

Table 2.4 Size and aspect ratio changes with a different surfactant.

Sample	Length (nm)	Width (nm)	Aspect Ratio
No additive	440.3	79.2	5.6
CTAB only	425.1	79.5	5.3
NaCl only	377.9	68.8	5.5
CTAB + NaCl	170.1	30.7	5.5

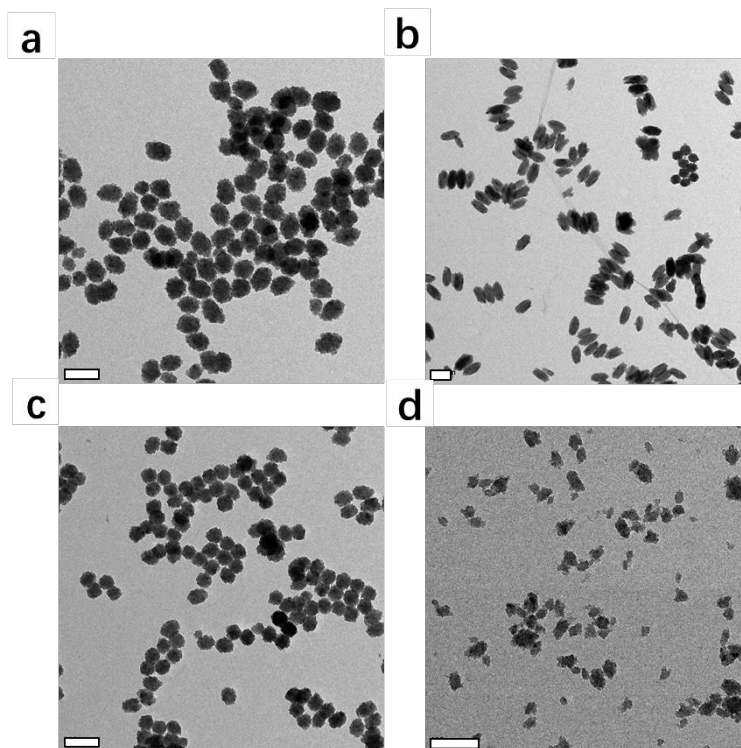


Figure 2.9 Synthesis of quasi-spherical FeOOH nanoclusters by adjusting the concentration of $\text{FeCl}_3 \cdot 6\text{H}_2\text{O}$ and CTAC. (a) With 0.1 M $\text{FeCl}_3 \cdot 6\text{H}_2\text{O}$ and 0.08 M CTAC. (b) With 0.1 M $\text{FeCl}_3 \cdot 6\text{H}_2\text{O}$ and 0.04 M CTAC. (c) With 0.2 M $\text{FeCl}_3 \cdot 6\text{H}_2\text{O}$ and 0.08 M CTAC. (d) With 0.05 M $\text{FeCl}_3 \cdot 6\text{H}_2\text{O}$ and 0.08 M CTAC. Scale bars are 200 nm.

For all the above-mentioned nanorods or clusters, we tested the X-ray diffraction (XRD) and found that all of them are β -FeOOH (Akaganéite, PDF#34-1266). Quasi-spherical FeOOH nanoclusters show a relative weak crystallinity, as the intensity of the peaks is relatively weaker and the FWHM (full width at half maximum) is larger. This is consistent with TEM image, where the large nanoclusters consist of many small particles. The low crystallinity does influence the post-reduction of the FeOOH nanoclusters, which will be discussed later in Section 2.3.2.

At last, the temperature effect was investigated by decreasing the synthesis temperature to 40 °C. At relative lower temperature, the reaction rate dramatically decreased, and the reaction resulted in a much more uniform product (Figure 2.11 g & h). The TEM images taken at different time point reveal the growth process for the FeOOH nanorods. Both the length and width gradually increased with prolonged reaction time, and the overall effect is the increase of the aspect ratio (Table 2.5). This also provides a new strategy for the synthesis of relative smaller nanorods.

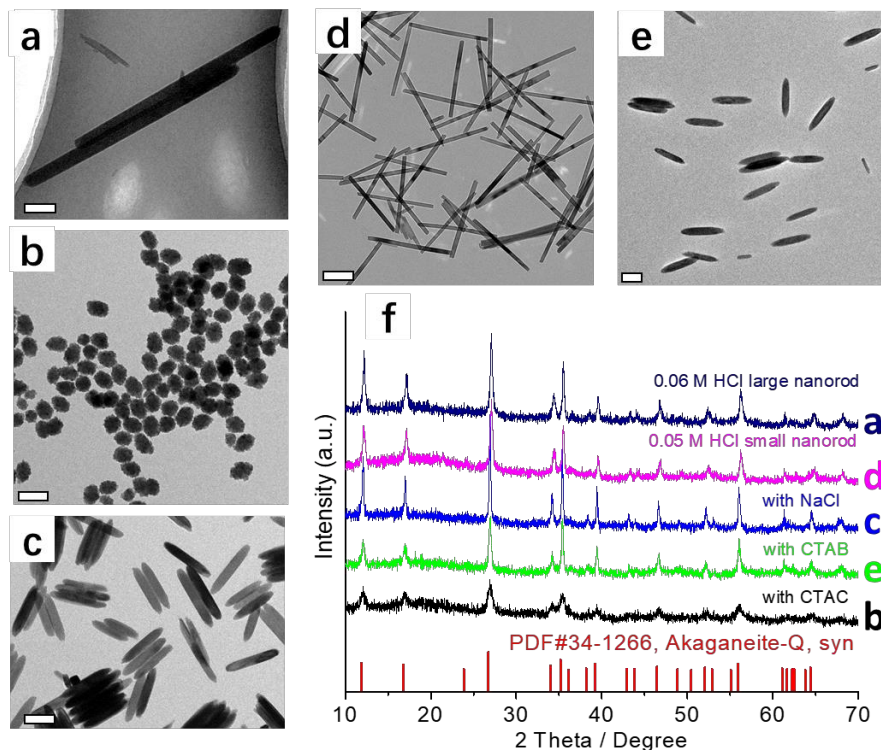


Figure 2.10 (a-e) FeOOH nanostructures synthesized by different reaction parameters. Scale bars are 200 nm. (a) 2 μm nanorods synthesized by using 0.6 M FeCl_3 and 0.07 M of HCl at 98 $^\circ\text{C}$ for 24 h. (b) Nanoclusters synthesized with 0.1 M $\text{FeCl}_3 \cdot 6\text{H}_2\text{O}$ and 0.08 M CTAC at 87 $^\circ\text{C}$ for 24 h. (c) Nanorods synthesized with 0.08 M NaCl at 87 $^\circ\text{C}$ for 24 h. (d) Nanorods synthesized by using 0.1 M $\text{FeCl}_3 \cdot 6\text{H}_2\text{O}$ and 0.05 M of HCl at 98 $^\circ\text{C}$ for 24 h. (e) Nanorods synthesized by using 0.1 M $\text{FeCl}_3 \cdot 6\text{H}_2\text{O}$ and 0.5 g CTAB. (f) XRD patterns of all the above mentioned FeOOH nanostructures.

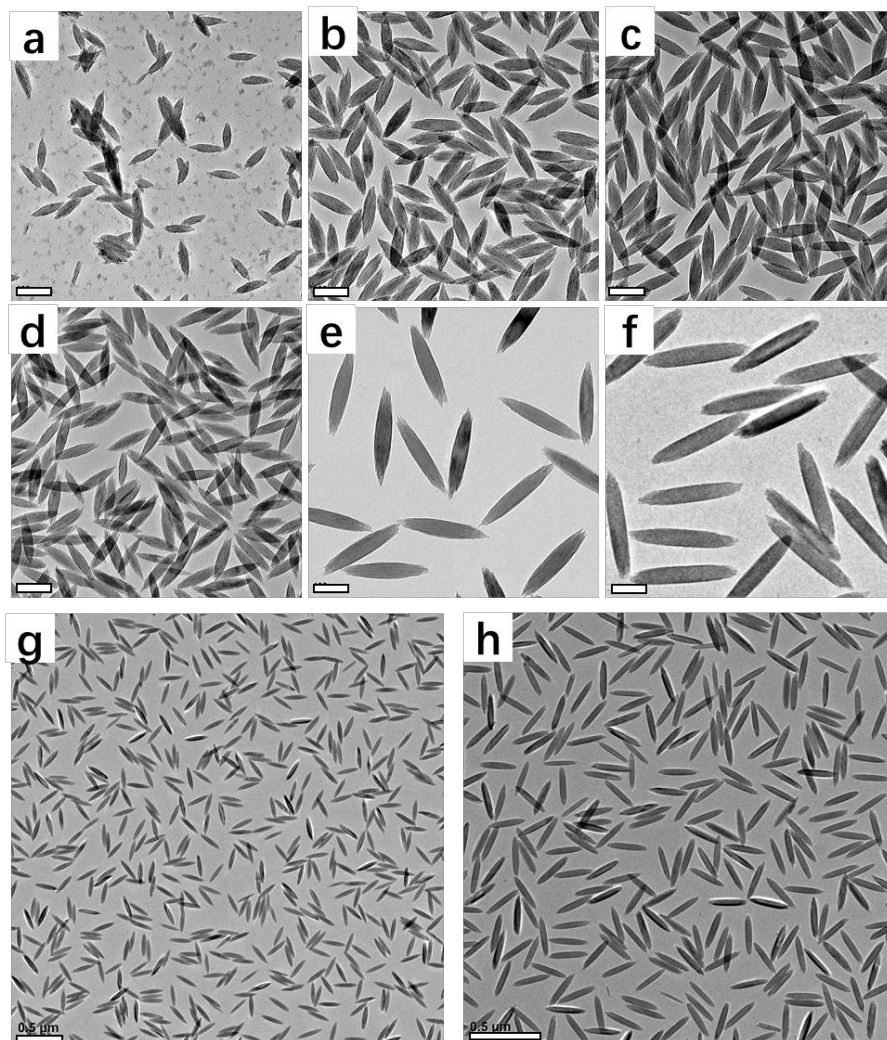


Figure 2.11 Effect of reaction temperature. FeOOH nanorods synthesized at 40 °C for different reaction time: (a) 26 h, (b) 34 h, (c) 42 h, (d) 48 h, (e & g) 5 days, and (f & h) 13 days. Scale bars in a-f are 100 nm.

Table 2.5 FeOOH nanorods synthesized at 40 °C for different reaction time.

Time	Length (nm)	Width (nm)	Aspect Ratio
26 h	91	24	3.9
34 h	132	36	3.7
42 h	151	36	4.2
48 h	151	31	4.9
5 days	257	45	5.7
13 days	270	47	5.7

2.3.2 Post-reduction Method to Form Magnetic Nanorods

Compared with the direct synthesis of magnetic iron oxide nanorod, we proposed the indirect synthesis strategy by a post-reduction method. There are several advantages of this strategy. First, the nonmagnetic hematite or akaganéite (β -FeOOH) nanorods could be synthesized in large scale (eg. 500 mL reaction solution, and dozens of grams' iron precursor), and the synthesis method is very easy (as illustrated above). Second, Surface modification of the nonmagnetic nanorods not only render the well dispersibility but also reserve the morphology of the anisotropic nanorods during the reduction procedure. Moreover, it will inhibit or reduce the aggregation of the magnetic nanoparticles due to the steric hindrance effect. Third, this strategy is universal and could be applied to nonmagnetic precursor materials with any sizes or components. It could be very promising to control the size and morphology of the magnetic materials by using different nonmagnetic precursor materials. Finally, by controlling the reduction parameters, eg. time and temperature, the reduction rate could be easily controlled, thus resulting in magnetic nanomaterials with different magnetization intensity.

(1) Solution phase polyol reduction

A polyol is an organic compound containing multiple hydroxyl groups. In the polyol synthesis, the multiple hydroxyl groups serve as the reducing agent during the synthesis.¹⁸ Via stabilization with strong coordinating capping ligands, such as PAA, we demonstrate the effectiveness of this method by transforming β -FeOOH nanorods into magnetic Fe_3O_4 nanorods, which are known to be challenging to produce directly.¹⁹

Figure 2.12a shows the scheme for PAA-protected polyol reduction of β -FeOOH nanorods. An aqueous dispersion of the β -FeOOH nanorods was injected into diethylene glycol (DEG) solution preheated at 220 °C. DEG was chosen as the reducing agent because the reduction in a solution phase of polyol could help eliminate close contact of the nanoparticles and reduce the possibility of aggregation and coalescence, which were commonly encountered during the high-temperature H_2 reduction of the solid phase. Moreover, in contrast to the cases of the rapid reduction under H_2 , the mild reducing power of polyols could allow convenient control over the conversion by fine-tuning the reaction time and temperature.

The as-synthesized β -FeOOH nanorods exhibited well-defined rodlike morphology with uniform size distribution. The average length of a typical nanorod sample is around 110 nm and average width approximately 20 nm (Figure 2.12b). To study the phase transition process, upon a certain time of incubation, the reaction was quenched to room temperature at different points in time (1, 4, and 8 h) and the respective intermediates were examined by TEM (shown in Figure 2.12c-e). Conversion started very quickly when the nanorods were reduced by DEG at 220 °C, producing small pores that coalesced and grew bigger over time. The nanorods appeared to be noticeably porous after ~1 h of reaction and hollow after ~4 h. Significantly, the overall morphology of the hollow nanorods changed very little upon continued heating for ~8 h, only showing a slight increase in hollowness inside the shell.

Subsequently, the phase transition process was further confirmed by X-ray diffraction (XRD) measurement. Figure 2.12f shows the XRD patterns of the original

sample and those underwent surface-protected reduction for 1, 4, and 8 h. All diffraction peaks in the black curve for the starting material can be indexed to β -FeOOH (JCPDS Card No. 75-1594). We concluded that β -FeOOH was fully converted to magnetite in 8 h based on the absence of the characteristic peak of β -FeOOH at 27° in the 8 h curve.

We also investigated the magnetic behavior of the final product magnetite nanorods by characterizing the field dependence of magnetization. The magnetic hysteresis loop of the magnetite nanorods measured at 300 K was illustrated in Figure 2.12g. Their saturation magnetization (M_s) was 40 emu/g. The coercivity was less than 2 Oe, which could be categorized as superparamagnetic, given a typical superparamagnetic limit of 30 Oe.²⁰

We then apply the same reduction method to β -FeOOH with even larger aspect ratio, which is about 28. As shown in Figure 2.12h & i, the nanorod morphology was well maintained after reduction. Also, we observed that the ends of the nanorods became open and irregular, as well as the decrease in length. This may be attributed to the partial dissolution of the iron species by DEG.²¹ We also tried the reduction of FeOOH nanoclusters that synthesized in the presence of CTAC. However, different from the nanorods, the morphology and shape of the nanoclusters could not be reserved during this ligand protected polyol reduction process (Figure 2.12j & k). This may be explained by the low crystallinity of the clusters, as discussed in section 2.3.1.

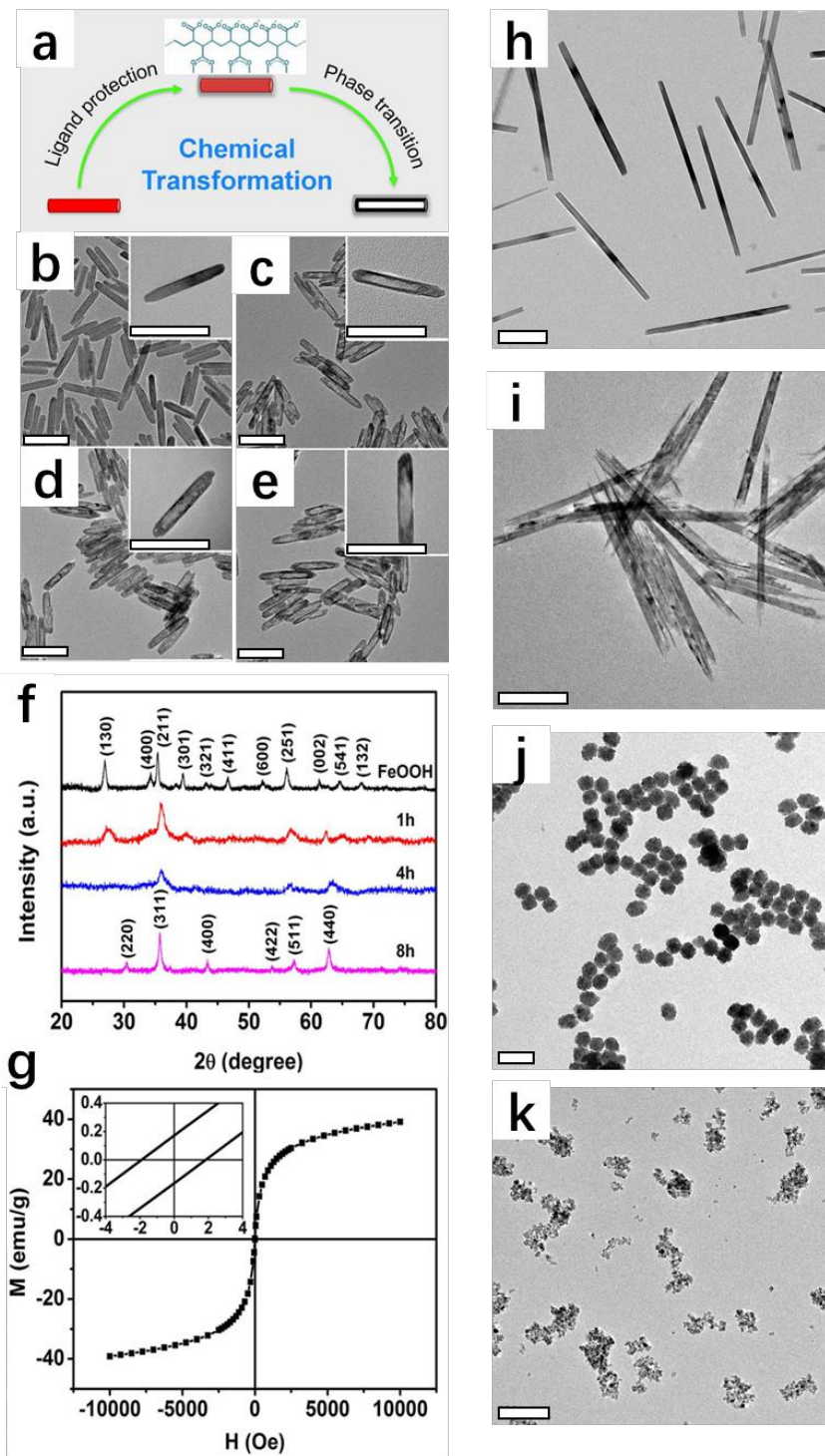


Figure 2.12 Solution phase polyol reduction of FeOOH nanorods. (a) Scheme showing the chemical transformation during surface protected polyol reduction. (b-e) TEM images of β -FeOOH and β -FeOOH reduced for 1, 4, and 8 h, respectively, (scale bars, 50 nm; insets, 20 nm) and (f) XRD. (g) The mass magnetization M as a function of applied external field H for the dried 8 h magnetite measured at 300 K (inset, expanded low-field curve). Figure a-g are reprinted with permission from Ref. ¹⁹. Copyright © 2017 American Chemical Society. (h & i) TEM images of β -FeOOH nanorods with large aspect ratio before (h) and after (i) polyol reduction. (j & k) TEM images of β -FeOOH nanoclusters before (j) and after (k) polyol reduction. Scale bars in h-k are 200 nm.

(2) Solid phase hydrogen reduction

For the solid phase hydrogen reduction, it is usually conducted at an elevated temperature, and hydrogen gas serves as the reducing agent. Since it is a solid phase reaction, so the aggregation and coalescence is a common problem. As introduced above, we did the silica coating first before the reduction. The silica layer will help to preserve the morphology of the anisotropic nanorods during the reduction procedure. Moreover, it will inhibit or reduce the aggregation of the magnetic nanoparticles due to the steric hindrance effect, and the surface charged induced repulsive force among particles in the solution.

We varied the silica coating thickness and performed the reduction under the same condition. Forming gas, which is the 5 % hydrogen and 95 % nitrogen gas mixture, was used as the reducing agent. The reaction temperature was 360 °C. Figure 2.13a & b show the TEM images of FeOOH@SiO₂ with 15 nm and 40 nm of silica coating after reduction. When the silica coating is thin, the nanorod shape could not be successfully reserved, as compared to 40 nm of silica coating. The hysteresis loop of FeOOH@SiO₂ with 40 nm silica coating after reduction and XRD pattern before and after reduction show that the nonmagnetic FeOOH nanorods have been transferred to magnetite after the solid phase forming gas reduction. However, when pure hydrogen was used as the reducing agent, under 500 °C of reaction for 2 h, the experimental results show that FeOOH has been transferred to metallic iron (Figure 2.13h). So, for the synthesis of magnetite, forming gas and lower reaction temperature are suggested.

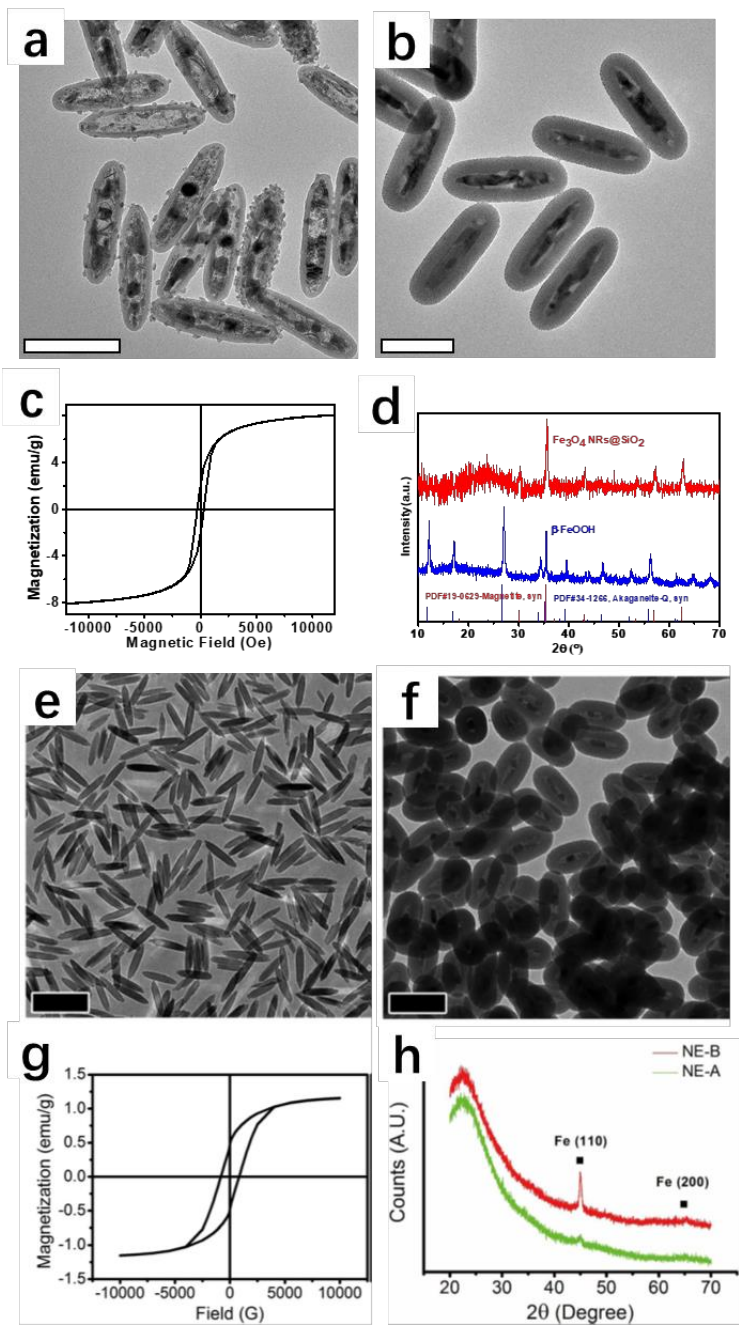


Figure 2.13 Solid phase hydrogen reduction. (a-d) FeOOH@SiO₂ nanorods reduced by forming gas at 360 °C for 2 h. (a) TEM image of FeOOH@SiO₂ with 15 nm silica coating after reduction. (b & c) TEM image and magnetic hysteresis loop of FeOOH@SiO₂ with 40 nm silica coating after reduction. (d) XRD patterns of FeOOH@SiO₂ with 40 nm silica coating before and after reduction. (e-h) FeOOH@SiO₂ nanorods reduced by hydrogen gas at 500 °C for 2 h. (e) TEM images of FeOOH nanorods. (f & g) TEM image and magnetic hysteresis loop of FeOOH@SiO₂ after reduction. (h) Red line: XRD patterns of FeOOH@SiO₂ after reduction. The green line is for another sample which is not mentioned here. Scale bars are 200 nm. Figure e-h are reprinted with permission from Ref. ²². Copyright © 2015 John Wiley and Sons.

(3) Solid phase carbothermal reduction.

Carbothermal reduction of iron oxides is the oldest technological process, which defined the history of humans during the last 4000-5000 years starting from the beginning of the Iron Age.²³ The carbon source could be either gas like CO or solid carbon.

Recently, resorcinol-formaldehyde resins (RFs) has been synthesized and used as a new form of carbon source. It is an attractive choice for its good carbon yield and easy handling. First, an RF shell was synthesized around the core and then calcining the RFs into carbon. It is the carbon shell that acts as a reducing agent. Simultaneously, the carbon shell prevents severe aggregation of the product caused by its own magnetic properties.²⁴

Figure 2.14a shows the schematic illustration for the experimental procedure. First, FeOOH nanorods were modified by PAA polymer to facilitate the RF coating. Then a Stöber-like sol-gel method was used to coat a layer of RF around the nanorod surface. After calcination under an elevated temperature, the nanorods could be reduced by the carbon species that produced during the carbonization process. As shown in the XRD patterns, relatively lower calcination temperatures, 400 °C to 550 °C, result in magnetite; but when the temperature was increased to 600 °C, metallic iron was the final product. TEM images after reduction show that at relatively lower temperature, the shape and morphology of the nanorods could be well reserved. However, when the temperature increased to 600 °C, the nanorods became hollow, and some of them broke into small pieces.

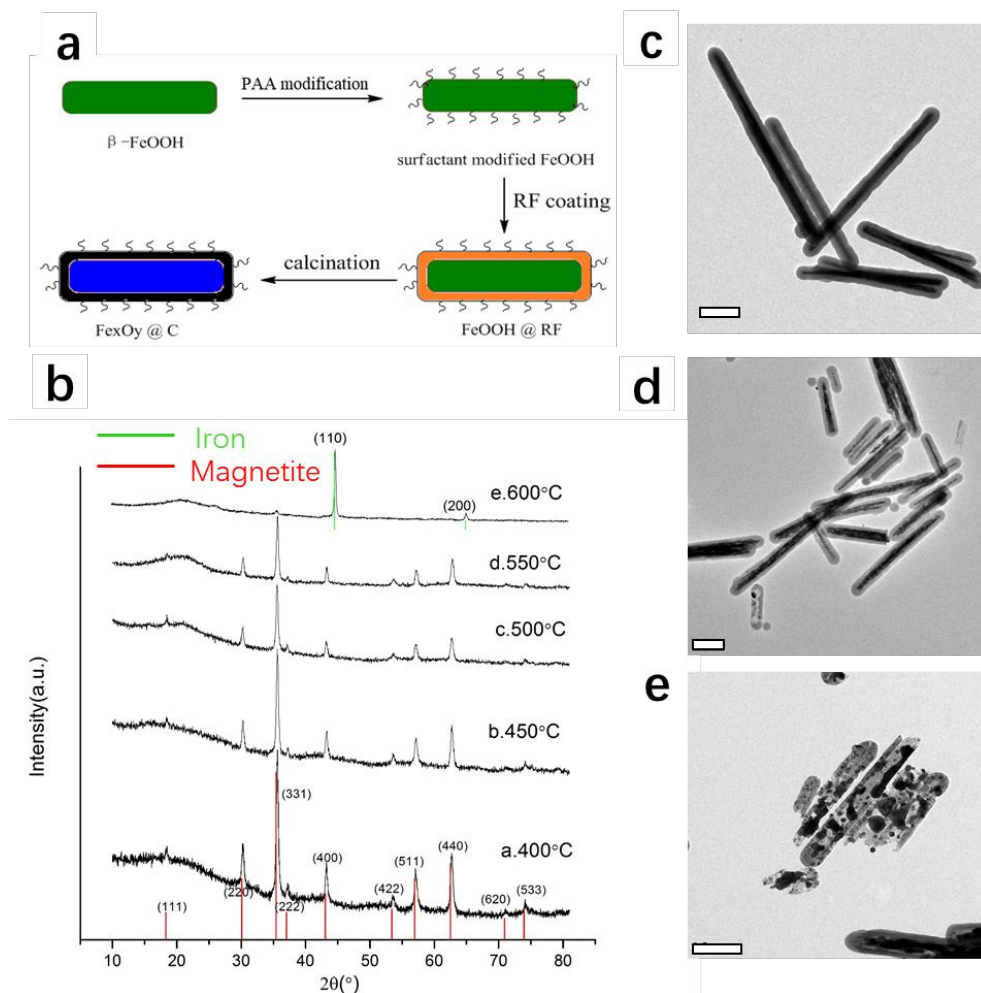


Figure 2.14 Solid phase carbothermal reduction. (a) scheme showing the carbothermal reduction procedure for FeOOH nanorods. (b) XRD patterns of FeOOH@RF nanorods reduced by the carbothermal method at a different temperature. (c-e) TEM images of FeOOH@RF nanorods before (c) and after carbothermal reduction at 550 °C (d) and 600 °C (e). Scale bars are 500 nm.

2.3.3 Post-reduction Method for the Synthesis of Photonic Crystal

In section 1.3, we introduced the magnetically controlled assembly of superparamagnetic colloidal nanocrystal clusters (CNCs) into one-dimensional photonic crystals. Moreover, in section 2.3.1, we demonstrated that nonmagnetic FeOOH nanoclusters could be readily synthesized by using CTAC as the surfactant. If we could use the post-reduction method to transfer those nanoclusters into magnetic nanoparticles, they may have the similar property.

Since the polyol reduction of PAA coated FeOOH nanoclusters could not reserve their original shape, a silica layer was first coated on the surface of the nanoclusters. Then both polyol and hydrogen reduction methods were used to transfer the nanoclusters to be magnetic. As shown in Figure 2.15a & b, the sample reduced by DEG for 24 h was used for magnetic separation first. After separation, the supernatant mainly consists of hollow particles or unreduced clusters (Figure 2.15f), and the TEM image for magnetically separated sample shows more dense clusters. After magnetically induced packing, the sample shows bright structure color, as shown in Figure 2.15d. Similarly, when different composition of hydrogen gas was used for the reduction, the samples all show some structure colors under magnetic field (Figure 2.15c). The sample reduced by forming gas at 360°C has the strongest bright color.

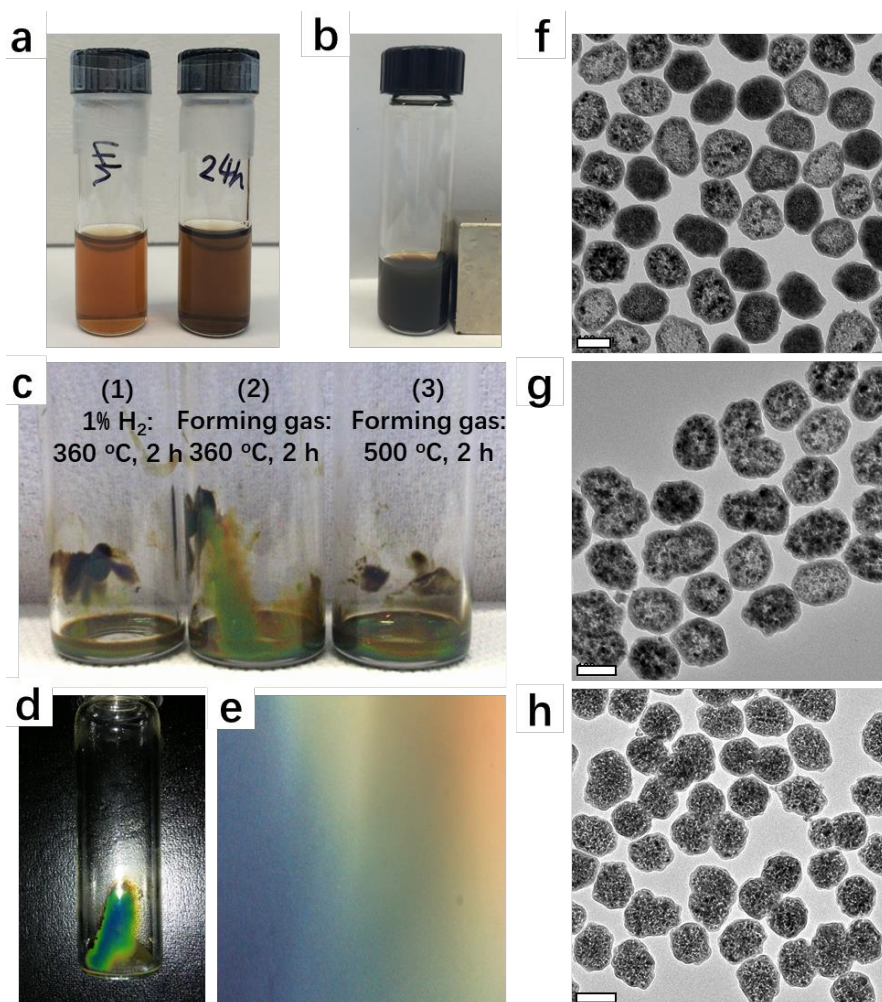


Figure 2.15 Post-reduction method for the synthesis of CNC-like photonic crystal. (a) Digital image of FeOOH@SiO₂ nanoclusters reduced in DEG for 4 h and 24 h, respectively. (b) Digital image showing the magnetic separation for sample reduced for 24 h. (c) FeOOH@SiO₂ nanoclusters reduced by hydrogen under different parameters all show structure color. (d) Structure color of 3-D photonic crystal assembled from sample magnetically separated in b. (e) Optical microscope image of the sample (2) in c. (f & g) TEM images of supernatant and magnetic separated nanoparticles from b. (h) TEM image of the sample (2) in c. Scale bars are 100 nm.

2.3.4 Magnetophoresis Performance of Magnetic Nanorods

Magnetic nanorods-based separation has been reported by Lim et al.²⁵ They systematically investigate the role of shape anisotropy in magnetophoresis. They claimed that under low gradient magnetic separation, the separation of magnetic nanoparticles is first driven by aggregation of particles by an externally applied magnetic field, and later the particle clusters formed can be easily collected through cooperative magnetophoresis. Also, the magnetophoresis is favored in anisometric particles at low particle concentration.

We tested the magnetophoresis performance of the magnetic nanorods synthesized based on 2 μm $\beta\text{-FeOOH}$ nanorods. First, the nanorods were coated with a layer of silica. Figure 2.16a-e show the TEM images of 2 μm $\beta\text{-FeOOH}$ nanorods before and after silica coating. When adding 20, 50 100 μL and 200 μL of TEOS, the coated silica shell thicknesses are 7.5 nm, 12.5 nm, 28 nm and 33 nm, respectively. Silica-coated $\beta\text{-FeOOH}$ nanorods with a shell thickness of 12.5 nm were chosen for the further experiment because of the relatively smooth surface. Also the shell thickness is not so large compared to the diameter of the rod. To improve the dispersibility of the magnetic nanorods, silica coated nanorods were first etched by 0.5 M oxalic acid at 60 $^{\circ}\text{C}$ for 3 h.²⁶ This etching procedure aims at producing cavity space at the end of the tube and further prevent the aggregation of nanorods due to magnetic interaction. TEM images (Figure 2.16f-h) indicate that after etching, both ends of most nanorods are etched away, and the cavity space was successfully produced.

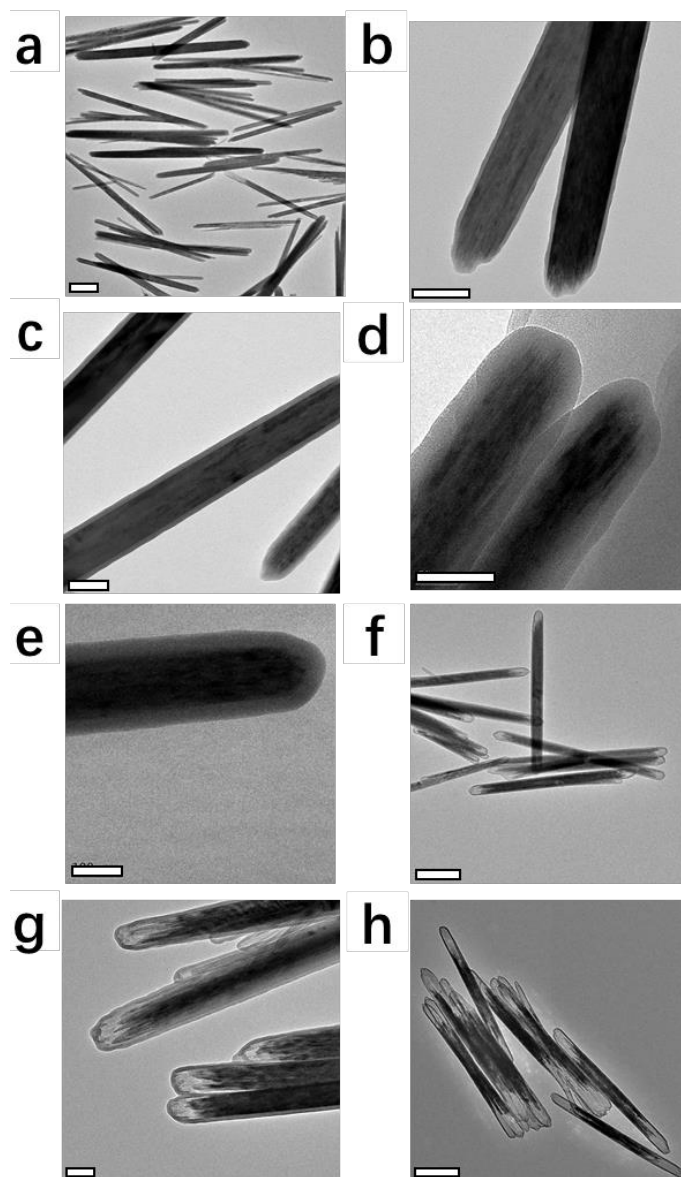


Figure 2.16 TEM images of FeOOH nanorods for separation. (a) As-synthesized FeOOH nanorods. (b-e) FeOOH@SiO₂ nanorods with 7.5 nm, 12.5 nm, 28 nm and 33 nm of silica coating, respectively. (f & g) FeOOH@SiO₂ with 12.5 nm silica coating after oxalic acid etching for 3 h. (h) Nanorods first etched by oxalic acid for 3 h and then reduced by DEG. Scale bars in a, f and h are 500 nm, and in other images are 100 nm.

The next step is to reduce the β -FeOOH nanorods by a post-reduction method. Solution phase polyol reduction is much milder than H_2 or carbothermal reduction, thus the reduction rate could be easily controlled.²⁷ Then nanorods both with and without oxalic acid etching were reduced at 230 °C for 24 h in DEG. The magnetophoresis and separation performance is shown in Figure 2.17. When dispersed in DI water, NRs before etching have shorter separation time, which is about 120 s; while the separation time for NRs after etching is longer than 120 s. Optical microscope images (Figure 2.17g & h) of NRs after etching and re-dispersed in water show that the NRs before etching could form longer chains, thus explain why they could be separated out more easily.

During the experiments, we found that the dispersibility of silica coated magnetic nanorods is much better in ethyl alcohol than in water. This reminded us to pay attention to the surface charge of the particles, and lowering the surface charge might do some benefit to the separation. We then tested the performance in buffer solution. When dispersed in the buffer, NRs after etching could be separated out more quickly, with a separation time of about 60 s in pH = 8.75 buffer solution and 45 s in pH = 7.30 buffer solution. Separation in buffer with neutral pH is faster. NRs tend to form a longer chain in water, but they form shorter clusters in the buffer.

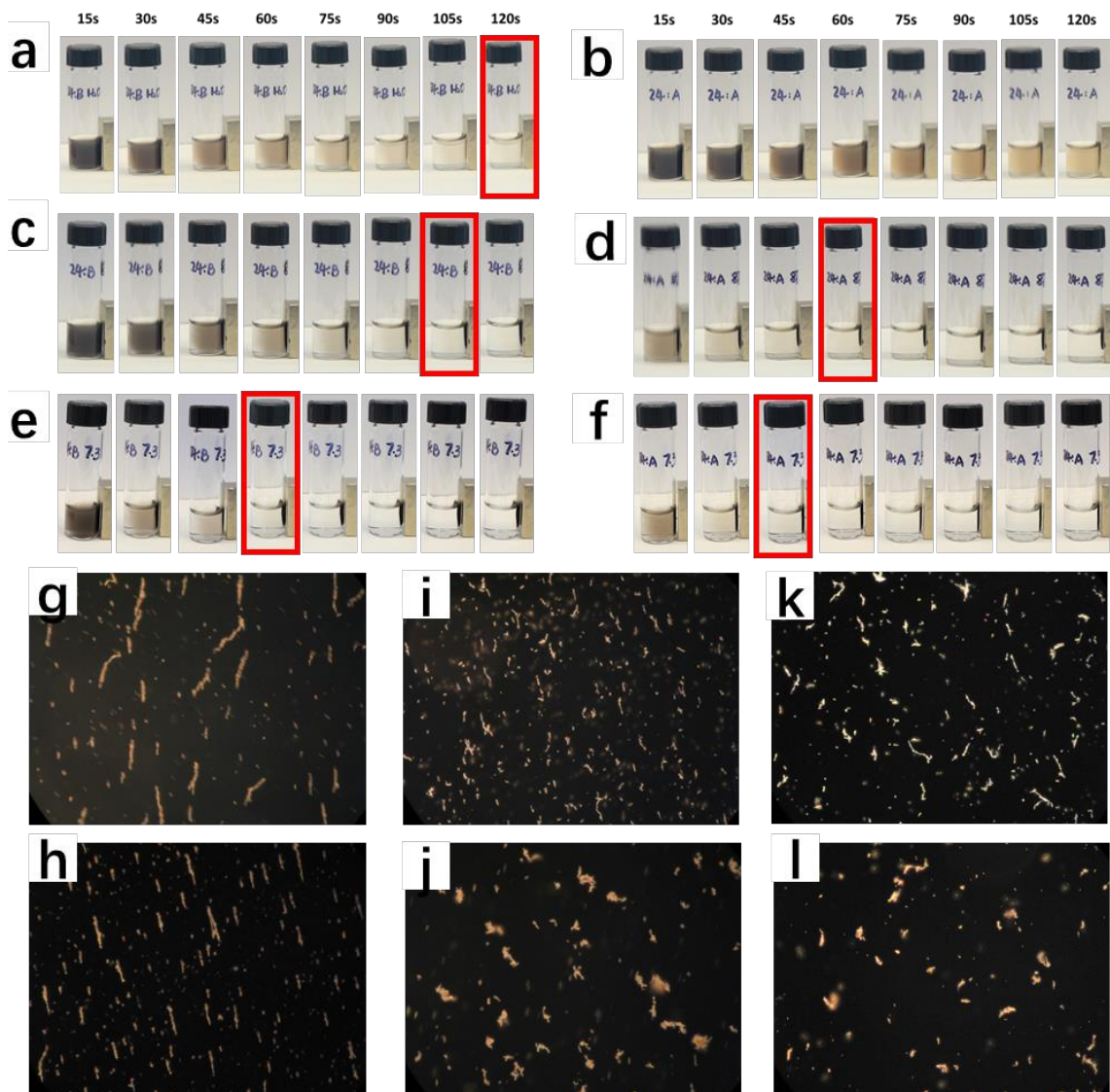


Figure 2.17 Magnetic nanorods for magnetophoresis and separation. (a-f) $\text{Fe}_3\text{O}_4@\text{SiO}_2$ nanorods before (a, c and e) and after (b, d, and f) oxalic etching and separated in DI water (a, b), pH = 8.75 buffer (c, d) and pH = 7.30 buffer (e, f). (g-l) Optical microscope images of the nanorods after separation and re-dispersed in water. (g-k) Nanorods before and (h-i) after etching and separated in DI water (g, h), pH = 8.75 buffer (I, j), and pH = 7.30 buffer (k, l), respectively.

Table 2.6 Separation performance of magnetic nanorods.

	Before etching	After etching
In DI water	~ 120 s	>120 s
In buffer (pH = 8.75)	~ 105 s	~ 60 s
In buffer (pH = 7.30)	~ 60 s	~ 45 s

Since etching of the nanorod ends can significantly improve the magnetophoresis and separation performance, we then varied the oxalic acid etching time from 3 h to 5 h and 7 h. As shown in Figure 2.18b-d, compared to 3 h etching, 5 h etching resulted in larger cavity space of the ends. When the etching time is 7 h, the majority of the FeOOH nanorods has been etched away. We then measured the real-time transmittance change of the solution at 600 nm by UV-Vis spectrometer to test the separation performance, and the time to reach 80% of transmittance was chosen as the separation time. From Figure 2.18a, we found that the longer the etching time, the longer the separation time. It is easy to understand since longer etching time means low magnetization for each nanorod. The ultimate case will be that when all the FeOOH has been etched away, and the nanorods lost their magnetic property. According to optical microscope observation, samples with longer etching time form smaller clusters, which were separated out with longer time.

It is worth noting that the end-etched magnetic nanorods achieved the best magnetophoresis and separation performance under almost neutral pH. It is very promising to test the performance of these magnetic nanorods in a physiological condition such as the bio-system. What's more, the cavity spaces located at the end of the tube could be the excellent carrier to accommodate some cargoes such as some biomolecules or drugs.

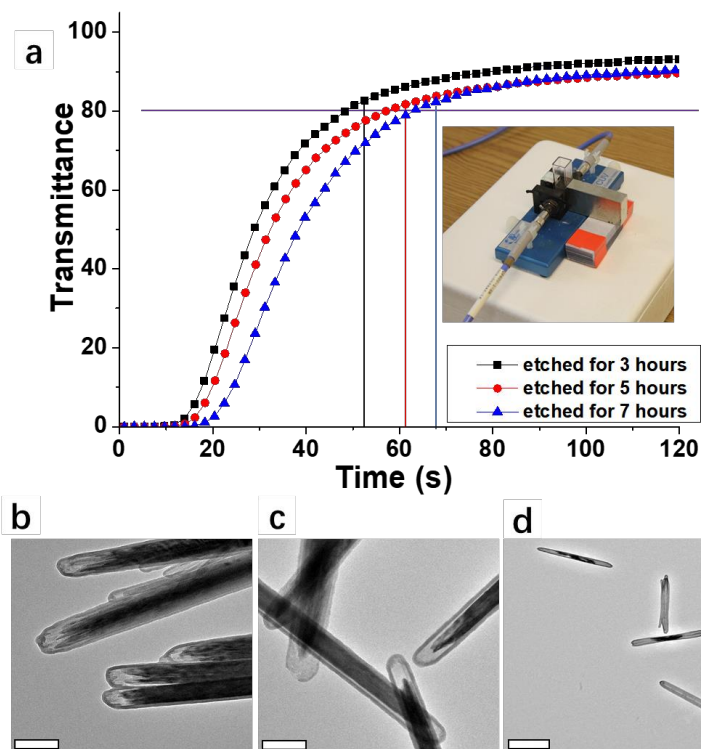


Figure 2.18 Magnetic nanorods with different oxalic acid etching time for separation (a) Real-time transmittance measurement during the separation procedure. Inset image shows the set up for the measurement. (b-d) TEM images of FeOOH@SiO₂ nanorods etched by oxalic acid for 3 h, 5 h, and 7 h, respectively. Scale bars in b and c are 200 nm, and scale bar in d is 1 μm.

2.4 Conclusion

First, uniform nonmagnetic β -FeOOH nanorods with different sizes and aspect ratios were synthesized by the hydrolysis of FeCl_3 . Parameters influencing the synthesis were systematically studied. HCl plays a special role in controlling the aspect ratio of the nanorods. With increasing concentration of HCl, the length of the nanorods gradually increases, and the width of the nanorods gradually decreases, thus results in increased aspect ratios. When increases the concentration of $\text{FeCl}_3 \cdot 6\text{H}_2\text{O}$, the width does not change obviously, while the length gradually increases, thus also results in increased aspect ratio. Both Cl^- and CTAB act as size-limiting agent in the synthesis. However, the using of CTAC as surfactant would result in decreased aspect ratio and size of the nanorods. We successfully synthesized quasi-spherical FeOOH nanoclusters by adjusting the concentration of $\text{FeCl}_3 \cdot 6\text{H}_2\text{O}$ and CTAC. At last, the temperature effect was investigated by decreasing the synthesis temperature to 40 °C. Due to dramatically lowered reaction rate, the reaction results in much more uniform FeOOH nanorods.

The indirect synthesis of magnetic iron oxide nanorods was achieved by a post-reduction method. Based on the reaction medium and the surface modification, we classify the post-reduction methods into (1) Solution phase polyol reduction; (2) Solid phase hydrogen reduction and (3) Solid phase carbothermal reduction. Solution phase polyol reduction is milder, and the reduction rate could be well controlled. However, it could not apply to FeOOH nanoclusters with relative low crystallinity. For both solid phase hydrogen reduction and carbothermal reduction, the reaction could be easily scaled up, and due to an elevated temperature, the reaction could be completed very efficiently

within a relatively shorter time. When high temperature (e.g., 500 °C) and pure hydrogen are used, metallic iron will be the product. For the synthesis of magnetite, forming gas and lower reaction temperature are suggested. For carbothermal reduction, to preserve the nanorod morphology, a relative lower temperature which is less than 600 °C should be used.

At last, the as-synthesized magnetic nanoparticles and nanorods could find potential applications for photonic crystal and separation. The FeOOH@SiO₂ nanoclusters, when reduced to magnetic, could show beautiful structure colors due to the formation of photonic crystals. 2 μm β-FeOOH nanorods, after silica coating, oxalic acid etching, and reduction, could be separated out by a magnet within 45 s in a pH = 7.30 buffer solution. It is very promising to test the performance of these magnetic nanorods in a physiological condition such as the bio-system. What's more, the cavity spaces located at the end of the tube could be the excellent carrier to accommodate some cargoes such as some biomolecules or drugs.

2.5 References

- (1) Lu, A. H.; Salabas, E. e. L.; Schüth, F. *Angew. Chem., Int. Ed.* **2007**, 46, 1222-1244.
- (2) Laurent, S.; Forge, D.; Port, M.; Roch, A.; Robic, C.; Vander Elst, L.; Muller, R. N. *Chem. Rev.* **2008**, 108, 2064-2110.
- (3) Park, J.; An, K.; Hwang, Y.; Park, J.-G.; Noh, H.-J.; Kim, J.-Y.; Park, J.-H.; Hwang, N.-M.; Hyeon, T. *Nat. Mater.* **2004**, 3, 891-895.
- (4) Wan, J.; Yao, Y.; Tang, G. *Appl. Phys. A* **2007**, 89, 529-532.
- (5) Lian, S.; Wang, E.; Kang, Z.; Bai, Y.; Gao, L.; Jiang, M.; Hu, C.; Xu, L. *Solid State Commun.* **2004**, 129, 485-490.
- (6) Wang, J.; Peng, Z.; Huang, Y.; Chen, Q. *J. Cryst. Growth* **2004**, 263, 616-619.
- (7) Yang, X.; Yu, P.; Moats, M. S.; Zhang, X. *Powder Technol.* **2011**, 212, 439-444.
- (8) Wang, J.; Chen, Q.; Zeng, C.; Hou, B. *Adv. Mater.* **2004**, 16, 137-140.
- (9) Guerrero-Martínez, A.; Pérez-Juste, J.; Liz-Marzán, L. M. *Adv. Mater.* **2010**, 22, 1182-1195.
- (10) Li, N.; Zhang, Q.; Liu, J.; Joo, J.; Lee, A.; Gan, Y.; Yin, Y. *Chem. Commun.* **2013**, 49, 5135-5137.
- (11) Zhao, W.; Gu, J.; Zhang, L.; Chen, H.; Shi, J. *J. Am. Chem. Soc.* **2005**, 127, 8916-8917.
- (12) Tartaj, P.; Serna, C. J. *J. Am. Chem. Soc.* **2003**, 125, 15754-15755.
- (13) Wang, M.; He, L.; Zorba, S.; Yin, Y. *Nano Lett.* **2014**, 14, 3966-3971.
- (14) Lu, Y.; Yin, Y.; Xia, Y. *Adv. Mater.* **2001**, 13, 415-420.
- (15) Hijnen, N.; Clegg, P. S. *Chem. Mater.* **2012**, 24, 3449-3457.
- (16) Piao, Y.; Kim, J.; Na, H. B.; Kim, D.; Baek, J. S.; Ko, M. K.; Lee, J. H.; Shokouhimehr, M.; Hyeon, T. *Nat. Mater.* **2008**, 7, 242-247.
- (17) Chaudhari, N. K.; Yu, J.-S. *J. Phys. Chem. C* **2008**, 112, 19957-19962.
- (18) Xiong, Y.; Siekkinen, A. R.; Wang, J.; Yin, Y.; Kim, M. J.; Xia, Y. *J. Mater. Chem.* **2007**, 17, 2600-2602.

- (19) Xu, W.; Wang, M.; Li, Z.; Wang, X.; Wang, Y.; Xing, M.; Yin, Y. *Nano Lett.* **2017**, 17, 2713-2718.
- (20) Ge, J.; Hu, Y.; Biasini, M.; Beyermann, W. P.; Yin, Y. *Angew. Chem., Int. Ed.* **2007**, 46, 4342-4345.
- (21) Fievet, F.; Lagier, J. P.; Blin, B.; Beaudoin, B.; Figlarz, M. *Solid State Ionics* **1989**, 32-33, 198-205.
- (22) Wang, M.; He, L.; Xu, W.; Wang, X.; Yin, Y. *Angew. Chem., Int. Ed.* **2015**, 54, 7077-7081.
- (23) L'vov, B. V. *Thermochim. Acta* **2000**, 360, 109-120.
- (24) Li, X.; Gai, F.; Guan, B.; Zhang, Y.; Liu, Y.; Huo, Q. *J. Mater. Chem. A* **2015**, 3, 3988-3994.
- (25) Lim, J.; Yeap, S. P.; Leow, C. H.; Toh, P. Y.; Low, S. C. *J. Colloid Interface Sci.* **2014**, 421, 170-177.
- (26) Lee, S. O.; Tran, T.; Jung, B. H.; Kim, S. J.; Kim, M. J. *Hydrometallurgy* **2007**, 87, 91-99.
- (27) Wang, M.; Gao, C.; He, L.; Lu, Q.; Zhang, J.; Tang, C.; Zorba, S.; Yin, Y. *J. Am. Chem. Soc.* **2013**, 135, 15302-15305.

Chapter 3 Anisotropic Magnetic/Plasmonic Composite Nanostructures for Information Encryption and Magnetic Field Sensing

3.1 Introduction

It is widely known that the plasmonic properties of metal nanostructures are mainly due to their size, shape and geometrical arrangement.¹⁻⁴ Compared to isotropic spherical particles, anisotropic nanostructures like nanorods, nanoplates, could offer tunability in plasmonic properties by controlling their shapes^{5,6} and geometric arrangement⁷⁻⁹. Instantaneous tuning of the geometrical arrangement of the plasmonic nanostructures is crucial, as it could achieve the selective excitation and quenching of specific plasmon modes. Thus the plasmonic properties could be dynamically controlled. Among all the physical and chemical stimuli, the magnetic field has attracted a lot of research interest because it could alter the behavior of magnetic materials in a contactless manner.¹⁰ What's more, the response of the magnetic materials to an external magnetic field is almost real-time, and not very sensitive to changes in experimental conditions.^{3,10,11}

We have successfully demonstrated that the orientation of gold nanorods could be dynamically controlled by binding them parallelly to the surface of superparamagnetic iron oxide nanorods. When applying an external magnetic field, the angle between the field direction and the direction of polarization of the incident light could be readily adjusted, thus resulting in the selective excitation of either transverse or longitudinal mode of the gold nanorods,³ as shown in Figure 3.1. This proof-of-concept demonstration offers us numerous opportunities to develop functional devices based on the magnetically controlled plasmonic property.

One advantage of magnetic manipulation is that the orientation of the nanostructures could be remotely controlled, regardless of the dispersing medium. When dispersed in the photocurable polymer, the anisotropic nanostructure arrays with a specific orientation, which controlled by the magnetic field, could be easily fixed by exposing to light.^{12,13} Since nanostructures with different orientations will show distinguished extinction property; the immobilized nanostructure arrays could be employed for the data storage and encryption application.^{14,15} Other than fixing the nanostructures, when dispersed in solution, the orientation could be dynamically tuned, thus result in instantaneous extinction change. The correlation between the magnetic field direction and the corresponding plasmonic extinction, if being carefully studied, could serve as the primary mechanism for design and fabrication of magnetic field direction sensor.¹⁶⁻¹⁸

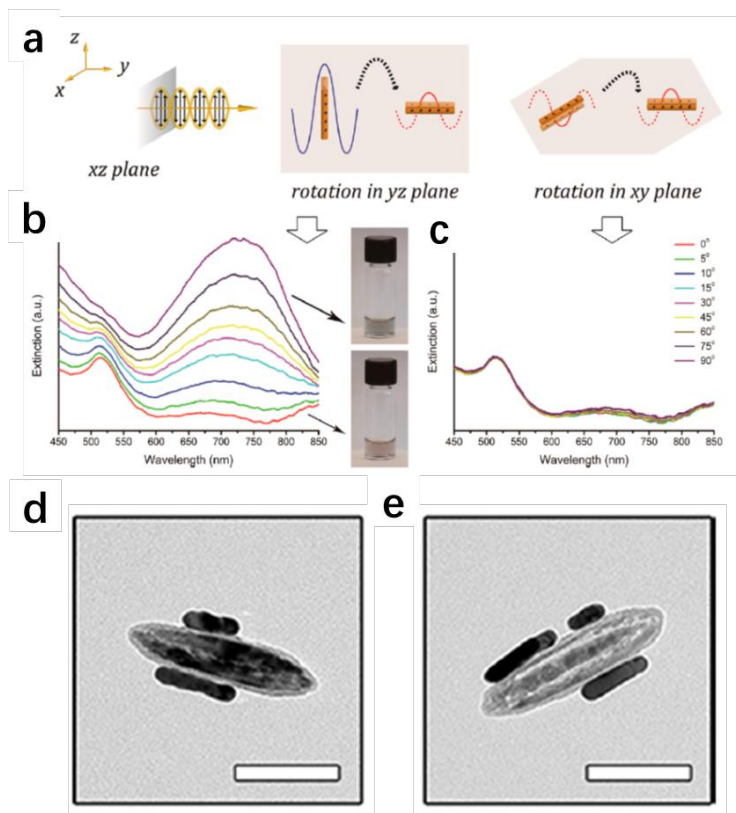


Figure 3.1 Magnetic tuning of plasmonic excitation of gold nanorods. (a) Scheme showing the plasmon excitation of AuNRs under polarized light. (b) Spectra of a dispersion of the hybrid nanostructures under a magnetic field with its direction varying from perpendicular to parallel within the yz plane. The incident light is polarized along the z-axis. The inset shows digital images of the dispersion under a magnetic field with its direction parallel (bottom) and perpendicular (up) to the incident beam. (c) Spectra of the dispersion under a magnetic field with its direction varying within the xy plane from perpendicular to parallel relative to the incident light. (d, e) TEM images of the as-assembled Fe₃O₄/Au NR structure. Scale bar: 100 nm. Reprinted with permission from Ref. ³. Copyright © 2013 American Chemical Society.

The magnetic component should have anisotropic shape, like the nanorod,¹⁹ to achieve the magnetic manipulation over the orientation of the plasmonic nanostructure. For anisotropic plasmonic structure, such as gold nanorods (AuNRs) and nanoplates, it is easy to extend the extinction peak to the near-infrared (NIR) range.^{1,2,5} For the above mentioned two applications, when the extinction is in the NIR range, it will enable more advantages to the application. For example, since the extinction is mainly in the NIR range, so that there will be negligible change in the visible range. For information encryption, the hidden information will not be recognized by naked eyes. For sensor application, the sensor performance will not be easily influenced by the room light. Magnetic/plasmonic composite nanostructures have also been fabricated by combining top-down fabrication and bottom-up self-assembly methods. The combined superparamagnetic and plasmonic functions enable switching of the infrared transmission of a hybrid nanorod suspension using an external magnetic field.¹¹

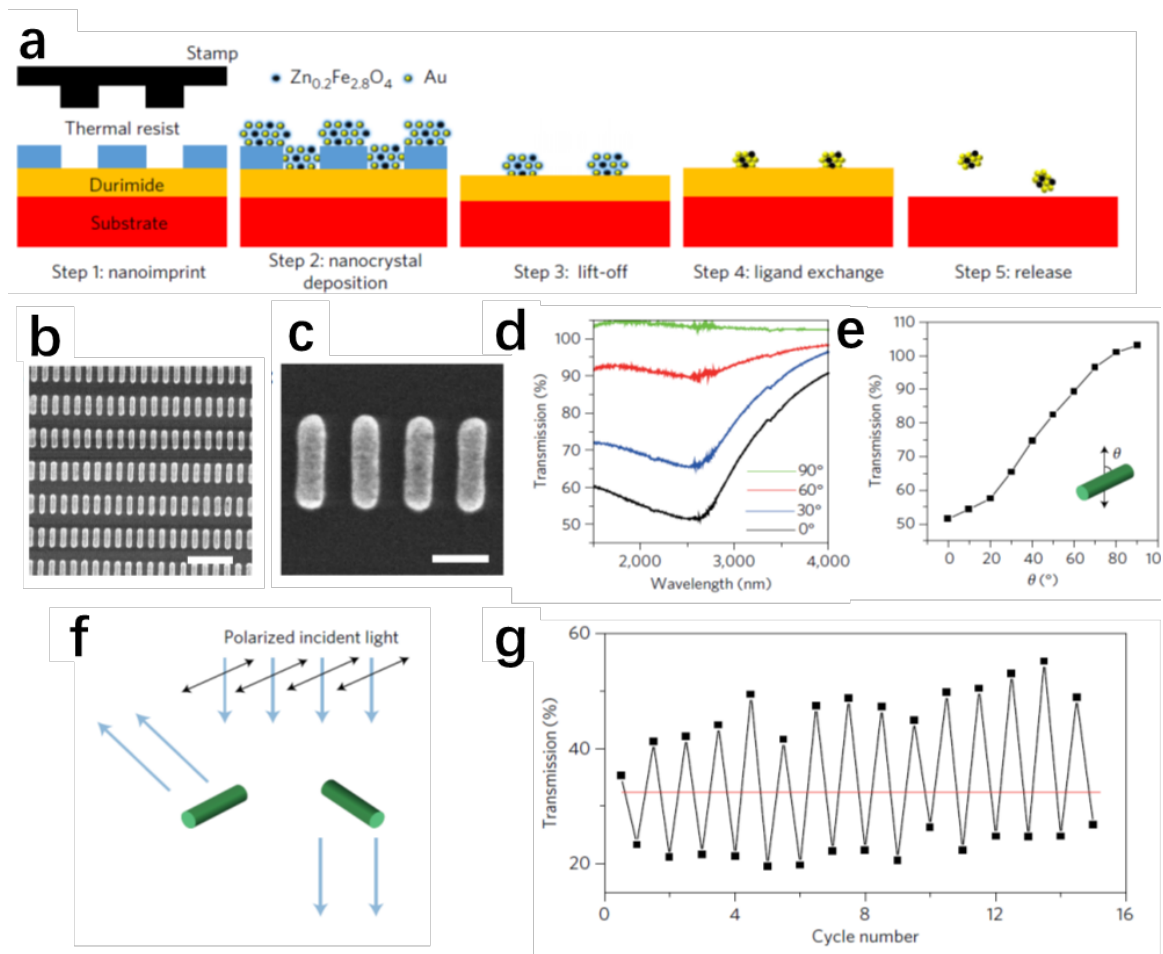


Figure 3.2 Magnetically switchable plasmonic nanorods assembled from a binary nanocrystal mixture. (a) Schematic of the $\text{Zn}_{0.2}\text{Fe}_{2.8}\text{O}_4\text{:Au}$ hybrid nanorod fabrication process. Step 1: a Si substrate with a spin-coated bilayer of Durimide and the thermal resist is imprinted with a nanorod-pillar-patterned stamp. Step 2: a mixture of Au and $\text{Zn}_{0.2}\text{Fe}_{2.8}\text{O}_4$ nanocrystals is deposited by spin-coating. Step 3: resist lift-off. Step 4: ligand-exchange of the patterned nanocrystal-based nanorods with NH_4SCN . Step 5: nanorod release on dissolving the Durimide layer. (b,c) Low- and high-resolution SEM images, respectively, of hybrid nanorod arrays before release. Scale bars, 1 μm for (b); 250 nm for (c). (d) Transmission spectra of the 1:3 vol/vol $\text{Zn}_{0.2}\text{Fe}_{2.8}\text{O}_4\text{:Au}$ hybrid nanorod array as a function of the polarization angle, θ , of incident light from 0° , for light polarized along the longitudinal direction, to 90° , for light polarized along the transverse direction. (e) Dependence of nanorod array transmission at 2,600 nm on θ , the angle between the light polarization direction (black double-headed arrow) and the nanorod (green) orientation. (f) Schematic of the modulated light transmission by controlling the orientation of the hybrid nanorods (green). Black double-headed arrows represent light polarization direction, and light blue arrows represent a light path. e, the cyclic performance of the light transmission at 2,600 nm for a 100- μm path length hybrid nanorod suspension in Remover PG under an alternating 120 Oe external magnetic field. Transmission for nanorods oriented perpendicular (above red line) and parallel (below red line) to the light polarization direction. Reprinted with permission from Ref. ¹¹. Copyright © 2016 Nature Publishing Group.

In this chapter, we started with the fabrication of anisotropic magnetic/plasmonic Fe_3O_4 NRs@ SiO_2 @Au core-shell nanocomposites. Akaganéite (β -FeOOH) nanorods are used as the starting materials, firstly coated with a layer of silica, and then reduced to magnetic nanorod; following by a seed loading and seeded growth method, we successfully synthesized the core-shell magnetic/plasmonic nanocomposites. When combining the anisotropic magnetic nanorod and ellipsoidal gold nanoshell, the orientation of the gold nanoshell could be readily adjusted by applying an external magnetic field. Our results demonstrated that the as-synthesized nanocomposites show angle-dependent plasmonic extinction property. Benefitting from the unique combination of anisotropic magnetic structure and orientation-dependent plasmonic property, together with the help of a homemade IR photoelectric coupling system, nanocomposites array with different orientation in a polymer film could generate different output voltages, thus could find unique applications for information encryption. Moreover, taking advantage of the instantaneous tuning over the orientation of the nanocomposites in solution, we extended the working principle and fabricated a new type of magnetic field direction sensor. An actuator system which consists of the sensor and a MeArm base servo motor vividly showed the performance of the sensing ability.

3.2 Materials and Methods

3.2.1 Materials

Iron(III) chloride hexahydrate ($\text{FeCl}_3 \cdot 6\text{H}_2\text{O}$), gold(III) chloride trihydrate ($\text{HAuCl}_4 \cdot 3\text{H}_2\text{O}$), polyacrylic acid (PAA, average M.W. 1800), tetraethyl orthosilicate (TEOS), formaldehyde (HCHO), 3-aminopropyltriethoxysilane (APTES), tetrakis-(hydroxymethyl)phosphonium chloride (THPC), 1-octanethiol, poly(ethylene glycol) methyl ether thiol (PEG-SH), poly(ethylene glycol) diacrylate (PEGDA, average M_n 575), phenylbis(2,4,6-trimethylbenzoyl)phosphine oxide (photoinitiator) were purchased from Sigma-Aldrich. $\text{NH}_3 \cdot \text{H}_2\text{O}$ solution (28%), NaOH, K_2CO_3 , CS_2 were purchased from Fisher Scientific. Ethanol (200 proof) was purchased from Decon Laboratories Inc. Polyvinylpyrrolidone (PVP, K12, average M.W. 3500) was purchased from Acros Organics. All the chemicals were used as received.

3.2.2 Synthesis of the Magnetic Iron Oxide Nanorods

Akaganéite ($\beta\text{-FeOOH}$) nanorods were synthesized by hydrolysis of iron chloride and used as the starting materials. In a typical synthesis, 400 mL of 0.1 M of $\text{FeCl}_3 \cdot 6\text{H}_2\text{O}$ solution was prepared and transferred into a capped glass bottle. The solution was then put into an oven of 60 °C and maintained at that temperature for 6 days. The solid product was collected by centrifugation (11000 rpm, 3 min) and was washed with water for several times. To facilitate the silica coating, the surface of $\beta\text{-FeOOH}$ nanorods was first modified by PAA. Typically, the pH of 0.1 M PAA solution (7.2 g/L, the concentration was calculated by the monomer) was first adjusted to 8-9 by adding 28% $\text{NH}_3 \cdot \text{H}_2\text{O}$ solution. To 40 mL of the above PAA solution, 40 mL of the $\beta\text{-FeOOH}$

nanorods (9 mg/mL) was added, and the mixture solution was stirred overnight. After three times of washing by water, PAA modified nanorods (β -FeOOH-PAA) were dispersed in water. The silica coating was conducted by a modified Stöber method. β -FeOOH-PAA (12 mL, 10 mg/mL), $\text{NH}_3 \cdot \text{H}_2\text{O}$ solution (28%, 4 mL) and ethanol (80 mL) were first mixed in an Erlenmeyer flask by vigorous stirring, followed by the addition of 200 μL TEOS. After 30 min reaction, the β -FeOOH NRs@SiO₂ nanorods were collected by centrifugation, washed with water (7500 rpm, 3 min) for three times and dried in an oven at 60 °C. Conversion of FeOOH NRs@SiO₂ to Fe₃O₄ NRs@SiO₂ magnetic nanorods was achieved by forming gas reduction at 360 °C for two hours in a tubular furnace. After reduction, the magnetic nanorods were collected and re-dispersed in 40 mL ethanol.

3.2.3 The Growth of Gold Shell on Magnetic Nanorods

The growth of gold shell on Fe₃O₄ NRs@SiO₂ magnetic nanorods was achieved by following a modified gold seed loading and seeded growth method reported by Halas et al.²⁰ The Fe₃O₄ NRs@SiO₂ magnetic nanorods were firstly modified by APTES to obtain the amino group functionalization, which could later serve as the anchor point for tiny gold seeds. In a typical procedure, 40 mL of the above Fe₃O₄ NRs@SiO₂ nanorod solution (dispersed in 200 proof ethanol) was transferred into a 100-mL three-neck flask, and heated to 78 °C. Then 200 μL of APTES was added to the flask. The mixture was firstly refluxed at 78 °C for 3 hours under vigorous stirring, then incubated during stirring at room temperature overnight for better functionalization of APTES. The nanorods

(Fe₃O₄ NRs@SiO₂-APTES) were collected by centrifugation and washed three times with ethanol (200 proof) and another three times by water, then dispersed in 12 mL of water.

Tiny gold seeds (about 1-2 nm) were synthesized following a reported protocol²¹ with slight modification. 96 mL of water, 315 μ L of 2.0 M NaOH, 126 μ L of 16 wt% THPC aqueous solution were mixed in an Erlenmeyer flask; after vigorous stirring for 5 min, 420 μ L of 0.25 M H₂AuCl₄·3H₂O was added in one-shot, and the color of the mixture underwent sudden change from colorless to dark brown. The as-synthesized gold seeds were further aged at 4 °C for about one week in a fridge before using. For gold seed loading, 1 mL of Fe₃O₄ NRs@SiO₂-APTES (10 mg/mL) was added to 10 mL of the above THPC gold seeds dropwise under sonication. After addition, the mixture was stirred for 60 min. Free gold seeds were removed by washing with water for twice, and the seed loaded nanorods (Fe₃O₄ NRs@SiO₂-Au seed) were re-dispersed into 15 mL of water.

Seeded growth of gold shell was conducted by using formaldehyde as reducing agent and a prepared gold growth solution²² as the gold precursor. Gold growth solution was prepared by mixing 49.6 mg K₂CO₃ with 300 μ L of 0.25 M H₂AuCl₄·3H₂O in 200 mL of DI water. The color of the mixture changed gradually from yellow to colorless within 30 min. The solution was aged for 1 day before use. Typically, 200 μ L of Fe₃O₄ NRs@SiO₂-Au seed was firstly mixed with 1 mL growth solution. For every 1 mL of growth solution, 25 μ L of formaldehyde (3.7 %) was added as the reducing agent. 50 μ L of PVP (5 wt%, average M.W. 3500) was added to the mixture when in total 4 mL of the growth solution was added. More growth solution was added with two minutes interval (1

mL each time) until in total 18 mL of the growth solution was reached. During the reaction, the color of the solution gradually changed from almost colorless to light pink, pink, red, purple, blue and green, finally blue-shifted back to purplish blue. After the completion of the gold shell growth, 500 μ L of PVP (5 wt%, average M.W. 3500) was further added to stabilize the gold surface and prevent aggregation. The mixture was incubated overnight, and excess PVP was removed by centrifugation and washing. The final product (PVP modified Fe₃O₄ NRs@SiO₂@Au shell) was concentrated to 1 mL. According to our test, the reaction for the growth of gold shell could be scaled up by at most 50 times, if more samples are needed.

3.2.4 Magnetically Controlled Angle-dependent Plasmonic Property Measurement

The extinction spectra of the nanocomposites were measured by a Varian Cary 500 double beam scanning UV/Vis/NIR spectrophotometer. Full extinction spectra were measured by using CS₂ as the solvent to eliminate the influence of water in the near infrared region. The surface of Fe₃O₄ NRs@SiO₂@Au shell was firstly functionalized by thiol groups through a ligand-exchange process, to obtain the excellent dispersibility of the nanocomposites in CS₂. In a typical procedure, 10 mL of PVP modified Fe₃O₄ NRs@SiO₂@Au shell aqueous solution was firstly re-dispersed in pure ethanol, then 0.25 mL of 1-octanethiol was added under stirring, and the mixture was incubated overnight. The thiol-functionalized samples were then washed with ethanol and re-dispersed in CS₂.

The sample was placed in a quartz cuvette with 1 cm path length. Linearly Y-polarized light (See Figure 3.5a) was achieved by using three polarizers with operating wavelength ranges located at 400-700 nm, 600-1100 nm, and 1050-1700 nm, respectively.

An external magnetic field was applied by using a servo motor which equipped with a permanent magnet. The distance between the magnet and the sample was fixed at 1.5 cm. To vary the θ angle, the polarization direction of the incident light was fixed, and the magnetic field direction was altered in the XY plane by rotating the magnet through the control over the servo motor.

3.2.5 FDTD Simulation of the Plasmonic Extinction

The finite-difference time-domain (FDTD) method was employed to calculate the extinction spectra and associated electric field distributions by using a total-field scattered-field source (TFSF). The Fe_3O_4 @ SiO_2 NRs@Au shell employed for the FDTD simulations is composed of the iron oxide core with a length of 259 nm and width of 49 nm surrounded by a 45-nm silica coating and 36.5-nm Au shell. A non-uniform meshing grid with smallest grid size ~ 1 nm was used. The refractive indices of gold and silica were adopted from Palik's Handbook of Optical Constants of Solids²³, while refractive index data of Fe_3O_4 was adopted from reference²⁴. The refractive index of surrounding CS_2 is set to be 1.62.

3.2.6 Fabrication of Polymer Film Consists of Nanocomposites Array with Different Orientations

In a typical process, the polymer film was prepared by fixing the nanocomposites in the matrix of PEGDA through photopolymerization. For a better dispersibility in PEGDA, the PVP-modified nanocomposites were first functionalized by poly(ethylene glycol) methyl ether thiol (PEG-SH) through the ligand-exchange method. Then nanocomposites made from 4 mL of the seed solution were firstly washed with ethanol and re-dispersed

into 20 mL PEGDA solution. 0.5 g (2.5 wt%) Phenylbis(2,4,6-trimethylbenzoyl)phosphine oxide was then added to the mixture solution as the photoinitiator. The mixture was sonicated for a while to make sure that the complete dissolution of the photoinitiator. Then the mixture solution was sandwiched between one glass slide (at the bottom) and one quartz slide (on top) separated by a glass spacer of 0.1 cm in height. The orientation of the nanocomposites was controlled by applying an external magnetic field. After sitting for 1 min in the magnetic field, the solution was cured by exposing to the light source for 20 s. **Film 0**, **Film 1** and **Film 2** were prepared when the magnetic field direction is parallel, 45° tilt, and perpendicular to the film. All the films are 2.5 cm * 2.0 cm in size, with a thickness of 0.1 cm.

3.2.7 Design and Setup of the Homemade IRPECS

Diagram of the homemade IR photoelectric coupling system (IRPECS) could be found in Figure 3.7d (left dashed box part). We use an infrared LED (THORLABS, LED1600L) with working voltage of 1.05 V and working current of 0.10 A and a linear film polarizer (THORLABS, LPIREA100-C) to provide the linearly Y-polarized or Z-polarized incident light. An IR photodiode (THORLABS, FGA015) and a signal amplifier (DROK, AD620) with a bias voltage of 6.0 V were used to detect the intensity change of the incident light that passes through the sample. We firstly fix the IR LED and IR photodiode on the breadboards, with a center distance of 12 mm. The breadboards were further fixed onto a plastic board to minimize the movement. For the testing of the solid film sample, a guide slot which made of PDMS was used to maintain a constant distance between the sample and the detector. For the test of the liquid sample, a cuvette

(0.5 cm path length) which contains the sample in PEG-DA solution was placed in between the light source and the photodiode. The whole system was warmed up for at least half an hour before using. The voltage signal coming from the IRPECS was recorded by an oscilloscope (OWON, VDS1022I).

3.2.8 Information Encryption by Using Nanocomposites Film Array

The nanocomposites film array (5.0 cm * 3.0 cm * 0.1 cm) was prepared by using small rectangular films (**Film 0**, **Film 1**, and **Film 2**) as the building blocks. All the small films are 1.6 cm * 0.8 cm in size, and with 0.1 cm for the thickness. Firstly, six small films in a specific sequence (e.g., **012012**) were sandwiched between one large glass slide (at the bottom) and one large quartz slide (on top) separated by a 0.1 cm glass spacer. Then pure PEGDA solution with 2.5 wt% of photoinitiator was then added to fill the remaining space between the two slides and the spacers. Upon exposing to the light source, the PEGDA solution was further cured and result in a larger film array.

3.2.9 Information Decryption by Using the Identification System

To easily read the information from the film array, we designed an identification system. The system consists of one programmed ARDUINO controller and a common anode LED (Chanzon, RGB). The anode of LED was connected to the 3.3V pin, and the cathodes of LED were connected to three different PWM pins of ARDUINO. The voltage signal that coming from the IRPECS, which serves as the input for the identification system, was connected to GND and ANALOG IN pins of ARDUINO. For **Film 0**, **1** and **2**, the emission colors were programmed to be red, green and purple (red + blue), respectively. As green and blue did not show the substantial visual difference, both in the

image and the video. Firstly, we decrypted the as-synthesized film array by using linearly Y-polarized light. We firstly placed the film array into the guide slot, then gradually moved it from left to right, so that each column could be measured. Then we changed the orientation of the polarizer and measured the film again by Z-polarized light.

3.2.10 Fabrication of Magnetic Field Direction Sensor.

The magnetic field direction sensor mainly consists of the IRPECS system and a liquid sample of nanocomposites in PEG-DA solution. Briefly, we place a cuvette (0.5 cm path length) which contains the sample in PEG-DA solution in between the light source and the photodiode. Depending on the different orientations of the nanocomposites, the IRPECS system will have different output, which could efficiently indicate the magnetic field direction change. For better visualization, we connected the sensor to a MeArm base servo motor through ARDUINO. The voltage signal that coming from the IRPECS, which indicates magnetic field direction change, was connected to GND and ANALOG IN pins of ARDUINO. The MeArm base servo motor was connected to 5.0V, GND and PWM pins of ARDUINO.

The linearly Y-polarized light was used as the incident light, and the magnetic field direction was changed in the XY plane. We choose the maximum (when $\theta = 90^\circ$) and the minimum (when $\theta = 0^\circ$) of the output voltage and set them to be 90° and 0° for the angle between the robotic arm and the long edge of the motor base (α). For the output voltage, when $90^\circ > \theta > 0^\circ$, we use a linear correlation between the voltage and the angle α . To test the performance of the sensor, we only need to place the permanent magnet near the

sample (about 1.5 cm on the left of the cuvette) and rotate it manually to change the direction of the magnetic field.

3.3 Results and Discussion

3.3.1 Synthesis of Anisotropic Magnetic/Plasmonic Nanocomposites

For the fabrication of anisotropic magnetic/plasmonic nanocomposites (Figure 3.3d), there are two main challenges. One is that direct synthesis of magnetic Fe_3O_4 nanorods usually results in aggregation^{25,26}, due to their ferrimagnetic nature. The other is that the direct gold shell deposition on bare iron oxide surface is relatively difficult by using the wet-chemical method. However, the indirect synthesis of magnetic nanorods by a post-reduction method has been more and more reported^{3,12,27,28}, and the growth of gold shell on silica surface has been well-established by Halas group²⁹. Therefore, we come up with the growth of gold nanoshells on indirectly synthesized magnetic nanorods to synthesize the nanocomposites. The whole process involves the following steps: (1) Synthesis of uniform $\beta\text{-FeOOH}$ nanorods; (2) Silica coating of $\beta\text{-FeOOH}$ nanorods; (3) Forming gas reduction to transfer the $\beta\text{-FeOOH}$ nanorods into magnetic Fe_3O_4 NRs@ SiO_2 ; (4) Introduction of amino groups onto the silica surface by 3-Aminopropyltriethoxysilane (APTES) modification and subsequent gold seed attachment and (5) Seeded growth on the surface of magnetic nanorods to form the gold shell. A scheme for the synthesis procedure could be found in Figure 3.3a.

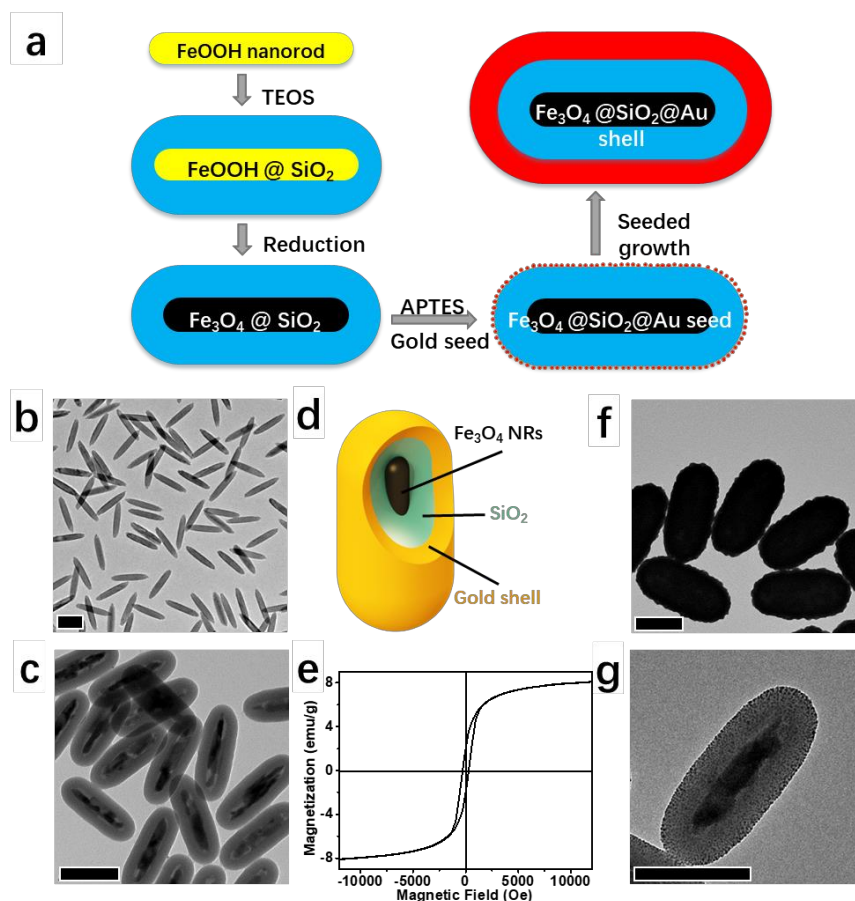


Figure 3.3 Synthesis and characterization of anisotropic magnetic/plasmonic Fe_3O_4 NRs@SiO₂@Au shell nanocomposites. (a) Scheme showing the synthesis procedure. (b) TEM image of β -FeOOH nanorods. The size of the nanorods is 286 nm in length and 45 nm in width. (c) TEM image of the magnetic Fe_3O_4 NRs@SiO₂ after forming gas reduction. The thickness of silica coating is 45 nm. (d) A three-dimensional schematic illustration of the nanocomposite structure. (e) Magnetic hysteresis loop of Fe_3O_4 NRs@SiO₂. (f) TEM image of Fe_3O_4 NRs@SiO₂@Au shell after seeded growth to form a complete gold shell coating. The thickness of the gold shell is measured to be 36.5 nm. (g) TEM image of the gold seed loaded NRs. Scale bars in b, c, f, and g are 200 nm.

We synthesized the uniform β -FeOOH nanorods by the hydrolysis of iron chloride. Figure 3.3b shows the transmission electron microscopy (TEM) image of the as-synthesized nanorods, and they possess an average size of 286 nm in length and 45 nm in width. The excellent size uniformity makes them excellent starting materials. Then we modify the nanorods with a layer of silica first and then transfer them to magnetic nanorods by forming gas reduction. Silica coating was achieved by a modified Stöber method, and the thickness of silica coating could be readily adjusted by controlling the amount of precursor (tetraethyl orthosilicate, TEOS) added. Silica coating has two functions: one is that silica could serve as the protection layer. It could prevent the nanorods from deformation during the forming gas reduction, and also prevent aggregation induced by the magnetic dipole-dipole attraction after reduction. The other is that the silica surface could serve as the substrate for further APTES modification and gold seed loading, which acts as the bridge layer. Figure 3.3c shows the TEM image of the magnetic Fe_3O_4 NRs@ SiO_2 . Due to the existence of the silica protection layer, the iron oxide core successfully maintains the rod structure. At the same time, the magnetic nanorods have an excellent dispersibility, as there is no aggregation from the TEM image. Before the forming gas reduction, the phase of the nanorods was determined to be akaganéite (Figure 2.13d, blue line), and the crystallinity is very good. After reduction, the phase changed to magnetite (Figure 2.13d, red line), and the crystallinity is not as good as previous, which we think is due to the structural deformation and shrinkage during the high-temperature treatment. Magnetic hysteresis loop of the Fe_3O_4 NRs@ SiO_2 in Figure 3.3e shows a saturated magnetization of 8.0 emu/g and coercivity of 290 G,

which confirm the ferrimagnetic property of the reduced samples. Also, the relative small saturated magnetization, which is about one-tenth of the superparamagnetic colloidal nanocrystal clusters that were used in our previous work³⁰, also explains why there is no aggregation after reduction, as the magnetic dipole-dipole interactions between the magnetic nanorods are very weak.

For gold seed loading, we first functionalized the silica-coated magnetic nanorods by APTES, which introduces abundant amino groups onto the silica surface. As shown in Figure 3.3g, we could successfully load the nanorods with a significant amount of the tiny gold seeds. The gold seeds are evenly and densely distributed on the nanorod surface, which facilitates the successful formation of a gold shell. We conducted the growth of the gold shell by using a prepared growth solution as gold precursor and formaldehyde as the reducing agent. The key in the seeded growth step is to avoid self-nucleation events. A fast reaction is preferred at first to avoid the ripening of the gold seeds. With small gold seeds ripening into large nanoparticles, the density of the seeds will decrease, which will influence the formation of a complete shell. However, after adding 4 mL of the growth solution, we added 50 μ L of polyvinylpyrrolidone (PVP, 5 wt%, average M.W. 3500) to the reaction mixture to prevent the aggregation of the composites. During the growth of the gold shell, with more and more growth solution added, the extinction spectra first gradually red shifted to about 765 nm, then a new peak located at about 650 nm emerged and became stronger and stronger (Figure 3.4a). When only 1 mL of growth solution was added, the gold seeds only grew larger, but couldn't form a continuous shell (Figure 3.4b). After adding 4 mL of growth solution, the larger gold nanoparticles coalesced and

covered most of the nanorod surface, but it was still not a complete shell (Figure 3.4c). When adding 12 mL of the growth solution, a continuous and complete shell was formed (Figure 3.4d). We stopped the reaction when 18 mL of the growth solution was added, since the peak at about 650 nm is already very obvious. Figure 3.3f shows a typical TEM image of the as-synthesized Fe_3O_4 NRs@ SiO_2 @Au shell nanocomposites, with in total of 18 mL of the growth solution used. The gold shell thickness was measured to be 36.5 nm.

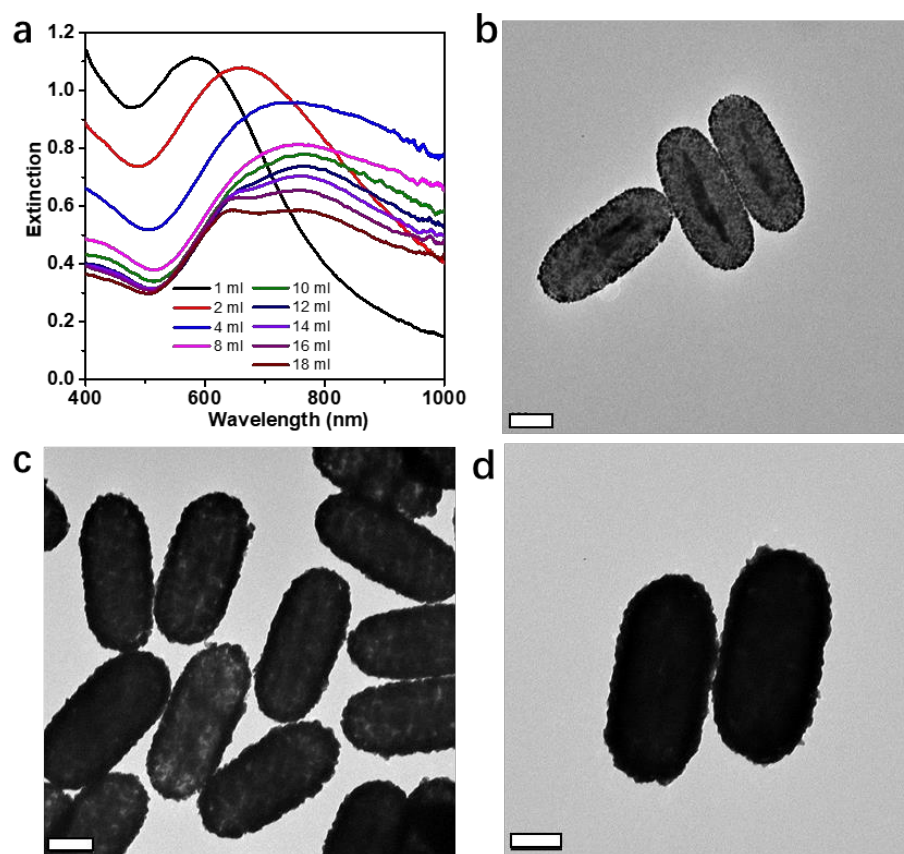


Figure 3.4 (a) UV-Vis spectra measured during the seeded growth process with different amount of the gold growth solution. (b-d) TEM images of the nanocomposites when the amount of the gold growth solution is 1, 4 and 12 mL, respectively.

3.3.2 Magnetically Controlled Angle-dependent Plasmonic Property

Upon applying an external magnetic field, the ferrimagnetic iron oxide nanorods, which are the cores in the nanocomposites, tend to orient themselves parallel to the direction of the magnetic field to minimize their magnetic potential energy and dipole–dipole interaction.^{3,12,31} By combining the anisotropic magnetic nanorod and ellipsoidal gold nanoshell, the orientation of the gold nanoshell now could be readily adjusted by simply applying an external magnetic field, which manifests the capability to exhibit magnetically controlled angle-dependent plasmonic property of such hybridized nanocomposites.

Figure 3.5a shows the schematic representation of the experimental setup for plasmonic extinction measurements. Linearly Y-polarized broadband light is incident along the X-axis. The orientation of nanocomposites is adjusted by applying an external magnetic field in the XY plane. The angle between the polarization direction of the incident light and the magnetic field is defined as θ (as schematically shown in Figure 3.5a). While θ is 0° , the polarization of excitation is just along the longitudinal axis of the nanocomposites; while θ is 90° , the polarization of excitation is then along the transverse axis of the nanocomposites. When varying θ from 0° to 90° by 10° each time, the extinction spectra gradually evolve from the red line to the black line, as shown in Figure 3.5b.

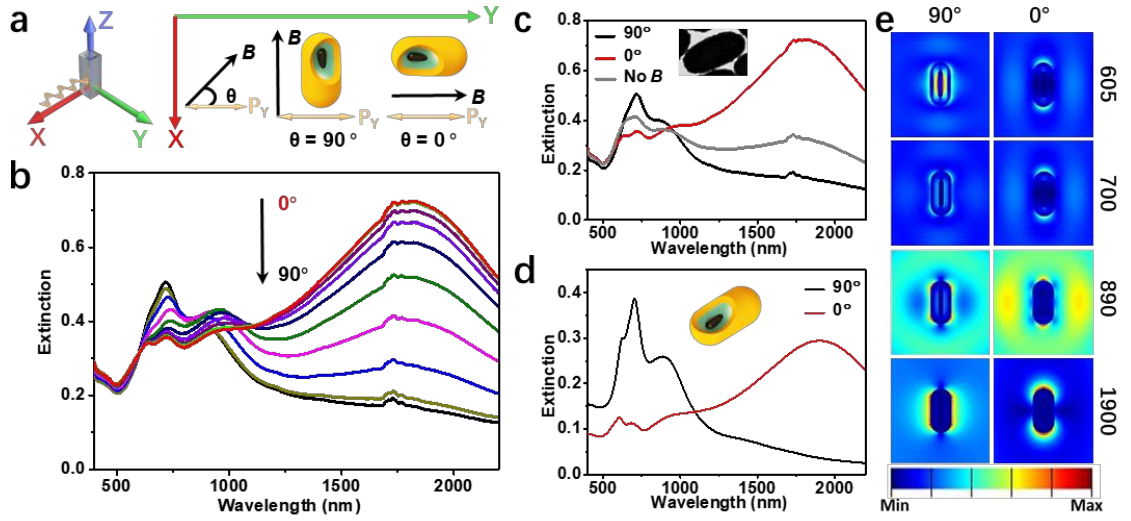


Figure 3.5 Magnetically controlled angle-dependent plasmonic property of the nanocomposites. (a) Schematic representation of the setup for plasmonic extinction measurement. (b) Extinction spectra measured when changing θ from 0° to 90° by 10° each time. The spectra are measured in a solution with CS_2 as the solvent. (c) Extinction spectra of the nanocomposites with θ of 90° and 0° , and without applying the external magnetic field, respectively. The inset shows the TEM image of a typical nanocomposite. (d) Calculated extinction spectra using the finite-difference time-domain (FDTD) method with θ of 90° and 0° . The inset shows the scheme of the nanocomposite used for simulation. (e) Electric field distributions, from top to bottom, under different excitation wavelengths of each peak as shown in extinction spectra: located at 601 nm, 692 nm, 958 nm, 1280 nm, and 1910 nm, respectively. The left column is when incident light polarized along the transverse axis (i.e., $\theta = 90^\circ$), and the right column is when incident light polarized along the longitudinal axis (i.e., $\theta = 0^\circ$).

The extinction peak at about 1820 nm gradually decreased, while the peaks at shorter wavelength, e.g., 640 nm and 720 nm, gradually increased, and with slightly peak position change. All the extinction intensity changes are mainly due to the orientation change of the gold shell, excluding the contributions from Fe_3O_4 NRs@ SiO_2 , as there is no obvious intensity change for Fe_3O_4 NRs@ SiO_2 while repeating the same controlled experiments (Figure 3.6a). The small peaks located in the range of 1650-1800 nm are verified to be the contribution from CS_2 (Figure 3.6b), which is the solvent used for the measurement. Upon no external magnetic field applied, since all the nanocomposites are randomly distributed in the solution, the measured extinction spectrum lies in between the red and black line, as shown in Figure 3.5c (grey line).

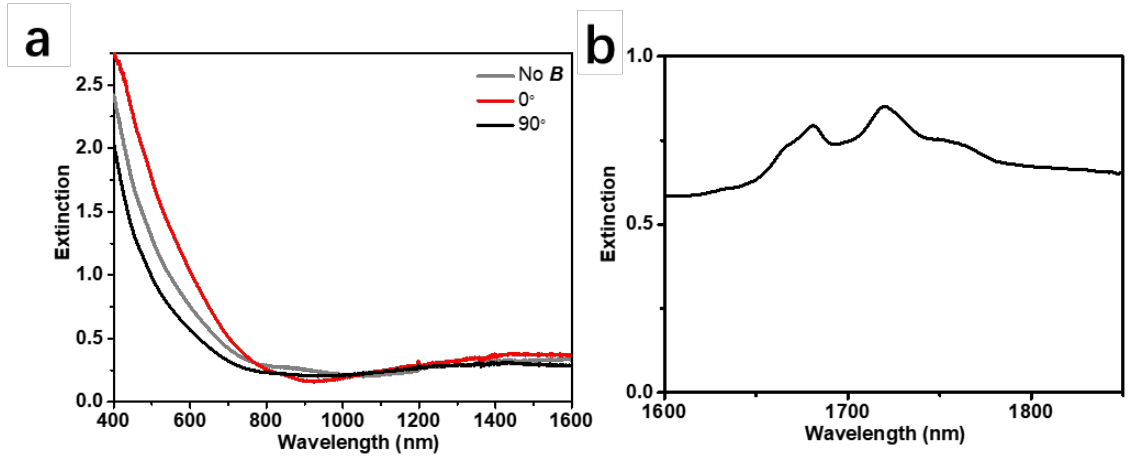


Figure 3.6 (a) Extinction spectra of the Fe₃O₄@SiO₂ NRs in PEGDA solution with θ of 90 ° and 0°, and without applying the external magnetic field, respectively. (b) Extinction spectra of CS₂.

For a better understanding of the extinction spectra, we employed the finite-difference time-domain (FDTD) method to investigate the corresponding plasmonic features. As is known to all, there are transverse (along with the short axis) and longitudinal (along with the long axis) surface plasmon resonance (SPR) modes in nanorod shaped metallic particles, which can be selectively excited by polarized light sources.⁵ Since now the orientation of the nanocomposites can be dynamically controlled by external magnetic field, we can thus selectively excite transverse or longitudinal SPR modes separately with no need for changing the optical property of light source. In this way, while θ is 90° by adjusting external magnetic field orientation, transverse SPR can be excited; while θ is 0° , longitudinal SPR can be excited. Simulated extinction spectra are presented in Figure 3.5d, with corresponding configurations as θ is 90° or 0° . As we can see, simulated spectra are in good agreement with the experimental results. For θ is 90° , transverse SPR is mainly excited showing extinction peaks in the visible wavelength range; while for θ is 0° , longitudinal SPR are mainly excited showing extinction peaks in the near-infrared wavelength range. To give a detailed theoretical explanation, typical field distributions located at 605 nm, 700 nm, 890 nm, and 1900 nm of both transverse and longitudinal SPR modes are depicted in Figure 3.5e. For θ is 90° , at short wavelength, e.g., 890 nm (see Figure 3.5e, left column, third row), transverse surface plasmon resonance (TSPR) of outer shell becomes quadruple and plasmonic resonance of inner core (dipole mode) becomes visible, and the total plasmonic extinction becomes hybridized. Moreover, the quadruple mode becomes even distinct when wavelength moves to even shorter, e.g., 700 nm (Figure 3.5e, left column, second row). Moreover,

the quadrupole mode is so strong that four lobes of radiation pattern can be observed. For shorter wavelength (e.g., 605 nm), the plasmonic resonance becomes more hybridized since the strength of plasmonic resonance of inner core turns to be more significant. On the other hand, for θ is 0° , as the polarization of excitation now is along the longitudinal axis, longitudinal SPR modes are excited, as shown in Figure 3.5e. For the wavelength of 1900 nm, it shows a very clean longitudinal dipole mode of the outer shell. While wavelength becomes shorter, high order longitudinal SPR modes are excited (e.g., 890 nm) while oscillation of the inner core becomes more and more evident, and total plasmonic resonance is thus hybridized. Besides, extinction coefficients of longitudinal SPR spectra (i.e., θ is 0°) are larger than that of transverse ones, which is quite consistent with the measured extinction spectrum. Overall, simulated extinction spectra are in good agreement with experimental data, except for slightly peak intensity change and peak position shift, which is possibly due to the imperfect nature of the synthesized gold shell.

3.3.3 Nanocomposites Array for Information Encryption

One of the advantages of instantaneous tuning of the geometrical arrangement of the plasmonic nanostructures by using external magnetic field is that the alignment of the magnetic/plasmonic nanocomposites is solvent independent, which offer us the opportunity to fix the orientation of the nanocomposites array inside a polymer film. Figure 3.7a shows the schematic illustration for the fixation of the nanocomposites array inside a poly(ethylene glycol) diacrylate (PEGDA) film. All the nanocomposites were fixed in the XZ plane. We vary the angle between the longitudinal axis of the nanocomposites and Z axis from 0° to 45° and then to 90° , and result in three films: **Film 0**, **Film 1**, and **Film 2**. The bottom image shows that the three films have a very similar appearance, and it is difficult to distinguish them by naked eyes. We measured the extinction spectra of the as-synthesized three films, with both linearly Z-polarized and Y-polarized light. As shown in Figure 3.7b, when the incident light was polarized along the Z axis, **Film 0** shows the highest extinction, as $\theta = 0^\circ$. **Film 2** shows the lowest extinction, as $\theta = 90^\circ$ and there was no contribution from the longitudinal modes. For **Film 1**, since $\theta = 45^\circ$, the extinction just lies in between that of 0° and 90° . It is worth noting that the extinction difference is mainly in the NIR range, and there is a slight difference in the visible range. This also explains why it is difficult to distinguish the three films by our own eyes, as they have almost the same color. However, when the incident light was polarized along the Y-axis, for all the three films, θ remains 90° , as all the nanocomposites were in the XZ plane. The extinction spectra are almost the same, as shown in Figure 3.7c, especially in the NIR range.

Based on the selective extinction property of the nanocomposite films, we designed a homemade IR photoelectric coupling system (IRPECS). Figure 3.7d shows the diagram of the IRPECS. IR LED with center emission at about 1600 nm (Figure 3.8a) was used as the incident light source. A film polarizer was used to generate the linearly polarized light. An IR photodiode (Figure 3.8b for the photodiode responsibility) together with a signal amplifier were used to detect the extinction change of the tested sample. When more light is illuminated onto the IR photodiode, it will generate a higher voltage, which makes it a perfect candidate to detect the extinction change. The output voltages for **Film 0**, **Film 1**, and **Film 2** with both Z-polarized and Y- polarized light were plotted in Figures 3.7e & f. Depending on the very different extinction, when the Z-polarized light was used, **Film 0**, **Film 1**, and **Film 2** showed output voltages of 1.076 V, 2.058 V, and 3.406 V, respectively. The higher the extinction, the lower the output voltage. When the Y-polarized light was used, all films showed the output voltages of 3.255 V to 3.395 V, as they have very similar extinction.

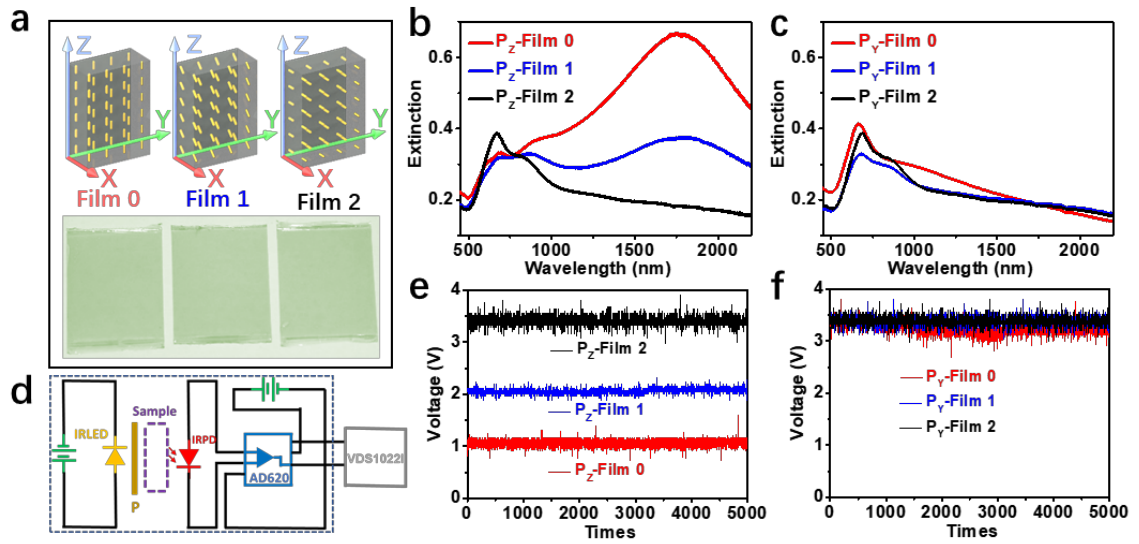


Figure 3.7 The electrical response of the nanocomposites array when tested by a homemade IR photoelectric coupling system. (a) Schematic illustration of the three polymer films consist of nanocomposites with different orientations (top row) and the digital images of the fabricated film. (b, c) Extinction spectra of the film measured under the illumination of linearly Z-polarized light (b) and linearly Y-polarized light (c). (d) Diagram of the homemade IR photoelectric coupling system (IRPECS). (e, f) Voltage of the film measured under the illumination of linearly Z-polarized light (e) and linearly Y-polarized light (f).

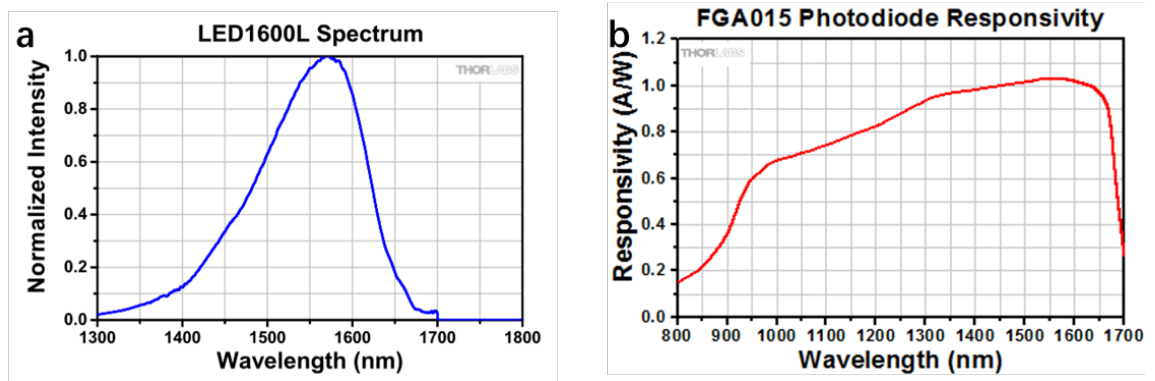


Figure 3.8 (a) Spectrum of the IR light source. (b) Photodiode responsivity profile.

Then we used small films (the orientations of the nanocomposites in small films are the same as **Film 0**, **Film 1**, and **Film 2**, and we name them as **0**, **1** and **2**) as building blocks for the demonstration of ternary data storage. Figure 3.10a shows the digital image of a nanocomposites film array with six building blocks, and the sequence of the six columns is **0**, **1**, **2**, **0**, **1**, **2**. The information stored in the film could be read out through the IRPECS. Figure 3.10b shows the digital image of part of the IRPECS (right part). For easier reading out, we combine the IRPECS with an identification system (left part of Figure 3.10b). Briefly, the output voltage for the tested film that comes from the IRPECS was used as an analog input signal for programmed ARDUINO, which controls the emission color of the LED light. Please refer to Figure 3.9 for the diagram of both the IRPECS and identification system. For **Film 0**, **1** and **2**, the emission colors were programmed to be red, green and purple (red + blue), respectively. For the same film, we could read it either using Y-polarized or Z-polarized light, as shown in the schematic drawing in Figures 3.10c & d. When the Y-polarized light was used, the readout result could be found in Figure 3.10e. All the films show almost the same voltages, as all the nanocomposites were in the XZ plane, and $\theta = 90^\circ$. From the identification system, the LED remains purple color during the test. When the Z-polarized light was used, the three kinds of the film showed very different output voltages, as shown in Figure 3.10f. From the identification system, the LED changed color among purple, green and red, based on the different types of the film. The readout could be recorded as “**012012**” (from left to right) or “**210210**” (from right to left).

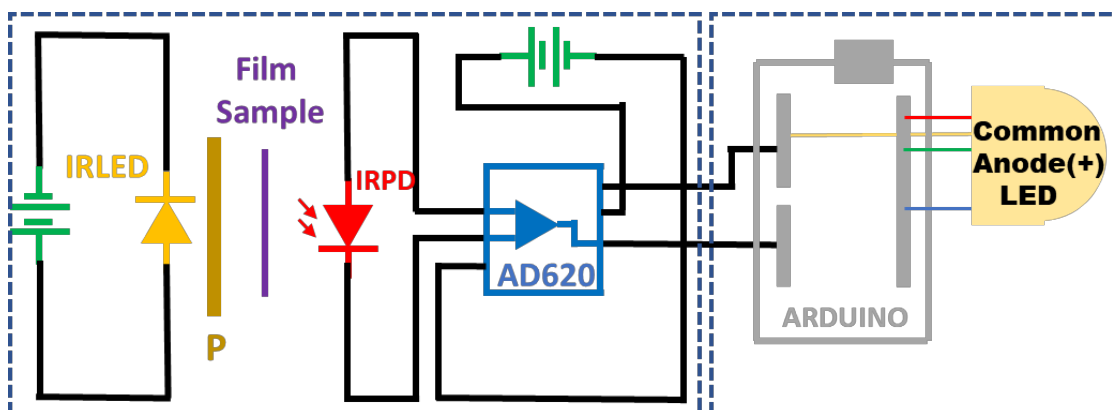


Figure 3.9 Diagram of the homemade IR photoelectric coupling system (IRPECS, left part) combined with the identification system (right part), which is a common anode LED that connected to the IRPECS through ARDUINO.

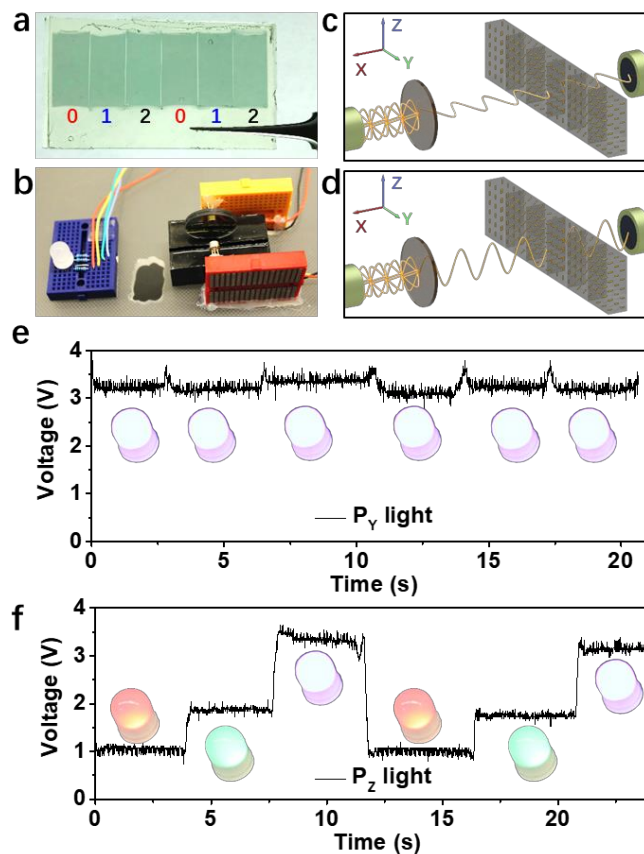


Figure 3.10 Nanocomposites array for information encryption. (a) Digital image of the fabricated film which consists of six building blocks. The sequence of the six columns is film 0, 1, 2, 0, 1, 2. (b) Digital image showing the IR light source, sample stage and photodiode part of the homemade IR photoelectric coupling system (on the right), and a common anode LED which connected to the system through ARDUINO (on the left). (c, d) Scheme showing the two decryption methods for the fabricated polymer film when using linearly Y-polarized light (c) and Z-polarized light (d), respectively. (e, f) A different voltage reading of the film when measured under the illumination of linearly Y-polarized light (e) and Z-polarized light (f). Insets: corresponding LED color when reading the specific column of the film.

For this ternary system, each column has 3 possibilities of the readout results. A nanocomposite array film with N columns will have 3^N different combinations. When $N = 3$, it is 27 combinations (Figure 3.11 for the scheme). For the film that we fabricated in this paper, since $N = 6$, so the total combinations will be $3^6 = 729$. What's more, from Figure 3.7e, we could find plenty of room between those three voltages, which means that more orientations of the nanocomposites could be fixed inside the film and be used as the building blocks. For example, if we add two more orientations, one with $\theta = 22.5^\circ$ and the other with $\theta = 67.5^\circ$, then there should be in total 5 different readouts. If we still fabricate a six-column nanocomposite array film, the total combinations will be $5^6 = 15625$.

In a word, the nanocomposite array film is an excellent example for multi-level information encryption. Firstly, the information hidden in the film could not be read directly by our own eyes, as all the columns have almost the same extinction in the visible range and show a very similar color. This is a common advantage when using materials with NIR extinction for information encryption or anticounterfeiting. Secondly, the information hidden in the film could vary with the testing method. When the incident light was polarized along Y and Z directions, the same film showed very different readouts, as shown in Figures 3.10e & f. This provides more security to the encryption: firstly, the film will only be valid when it has the polarization dependent readout property; secondly, without knowing which polarization is the right one for data decryption, the information hidden in the film will also be safe. For the information encryption purpose, here we only show that our magnetic/plasmonic nanocomposites array could be an

excellent candidate. More complicated encoding and decoding methods could be designed and used for an even higher level of information encryption.

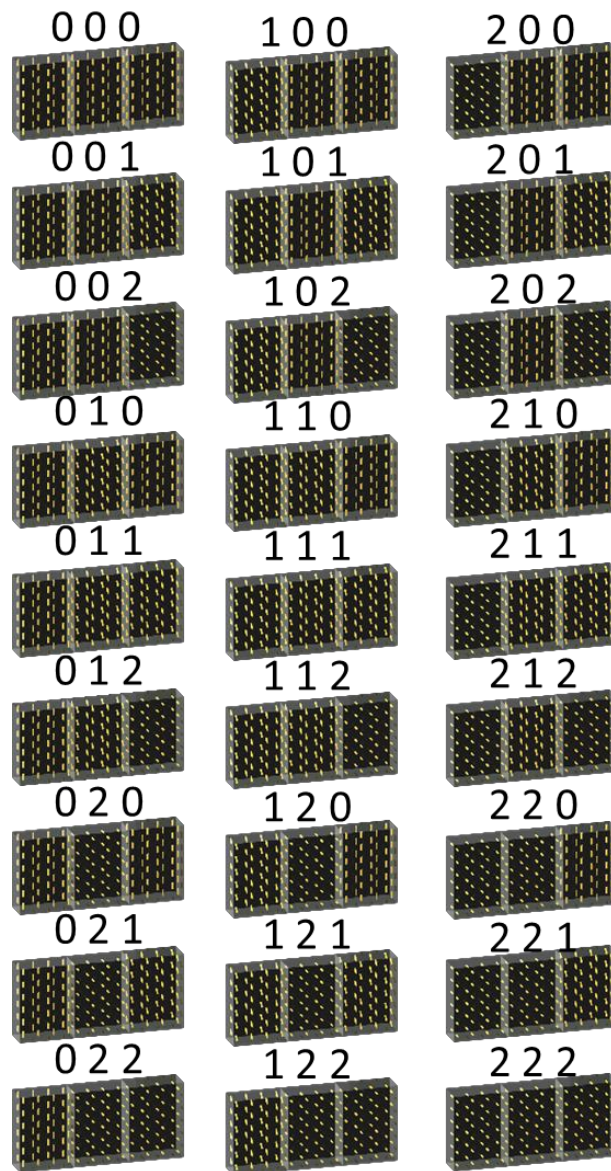


Figure 3.11 27 possible combinations of a three-column film, which shows a “222” reading under the Y-polarized light when reading under the Z-polarized light.

3.3.4 Application in Magnetic Field Direction Sensing

When dispersed in solution, the orientation of the nanocomposites could be dynamically tuned by applying the external magnetic field. Based on the output voltage, the direction of the external magnetic field could be deduced, which offers us a new opportunity for the fabrication of a new type of magnetic field direction sensor. Magnetic field sensing involves a variety of magnetic sensors to detect the presence, strength, or direction of magnetic fields. Most of the magnetic sensors are fabricated base on Hall effect or giant magnetoresistance.^{16,17} However, in our design, we utilize the angle-dependent plasmonic property of the nanocomposites.

Figure 3.12a shows the scheme of the sensor. The cuvette contains the liquid nanocomposite sample was placed at the sample stage. Linearly Y polarized light was used as the incident light. Upon changing the external magnetic field direction in XY plane, the output voltage that generated from the photodiode will change accordingly. The complete diagram could be found in Figure 3.12b (left part). We measured the extinction spectra and the output voltages of the same liquid sample when changing θ from 90° to 0° by 10° each time. As plotted in Figure 3.12c, from 1300 nm to 1700 nm, the extinction gradually increased while θ changing from 90° to 0° , but the corresponding output voltages gradually decreased.

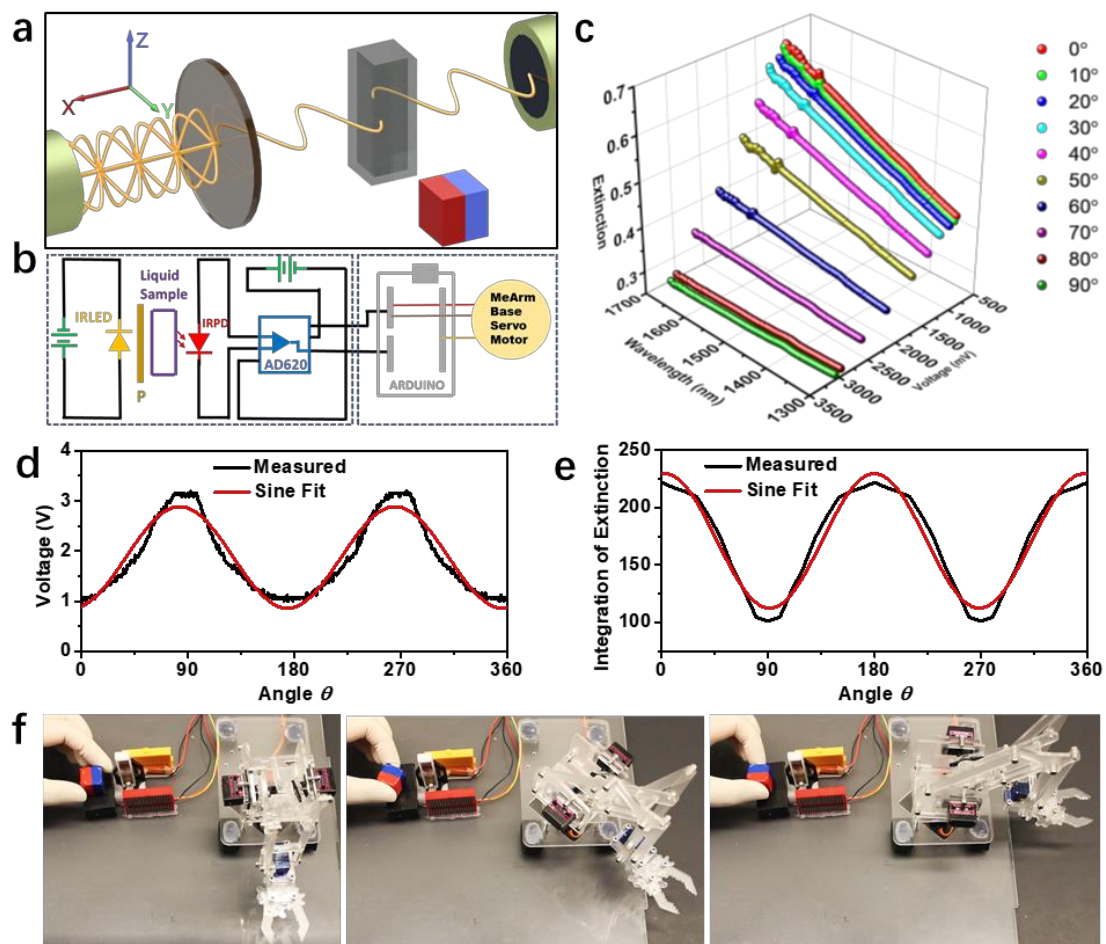


Figure 3.12 Magnetically controlled real-time photoelectric response of the nanocomposites in solution and its application for magnetic field direction sensor. (a) Schematic representation of the sample stage part. A cuvette containing the sample solution was placed in between the light source and the photodiode. A permanent magnet was used to dynamically control the orientation of the nanocomposites in XY plane. (b) Circuit diagram of the magnetic field direction sensor (left part) and an actuator (right part). (c) Extinction spectra and photoelectric response of the nanocomposites in solution when changing θ from 90° to 0° , by 10° each time. (d) Voltage plotted over θ angle and its sine fit. (e) Integration of the measured extinction from 1300 nm to 1700 nm of the nanocomposites in PEG-DA solution plotted over θ angle and its sine fit. (For both d and e, when θ changes from 90° all the way back to 0° , we did the conversion for the angle to be 90° to 180° . The similar conversion has been done for the second cycle of the angle change to be 180° to 360° .) (f) Digital images showing the magnetic field direction sensor based actuator system. From left to right, the robotic arm moved accordingly when changing the direction of the external magnetic field.

The correlation between θ and the output voltage was further determined by a quasi-continuous measurement. We used a servo motor that equipped with a permanent magnet to provide the external magnetic field, and the motor was programmed to rotate continuously at a speed of 10° per 50 ms. The output voltages were plotted over time (Figure 3.13b), and it shows very consistent results for six measurement cycles. We then plotted the output voltages over angle θ , with some conversion of θ from 90° to 360° range. As shown in Figure 3.12d, the spectrum shows an obvious sine fit, with a fitting function of $V_{output} = 1.873 + 1.103 \sin[\pi(\theta - 37.56)/90.96]$, which is in the form of $y = y_0 + A \sin[\pi(x - x_c)/\omega]$ (A , the amplitude of the peak and ω , peak width, y_0 and x_c are constants). Since the output voltage is directly related to the extinction of the tested solution, we then plot the integration of extinction from 1300 nm to 1700 nm over θ . Figure 3.12e shows an obvious cosine fit, which could explain why the output voltage is compliant with a sine fit, since the higher the extinction, the lower the output voltage.

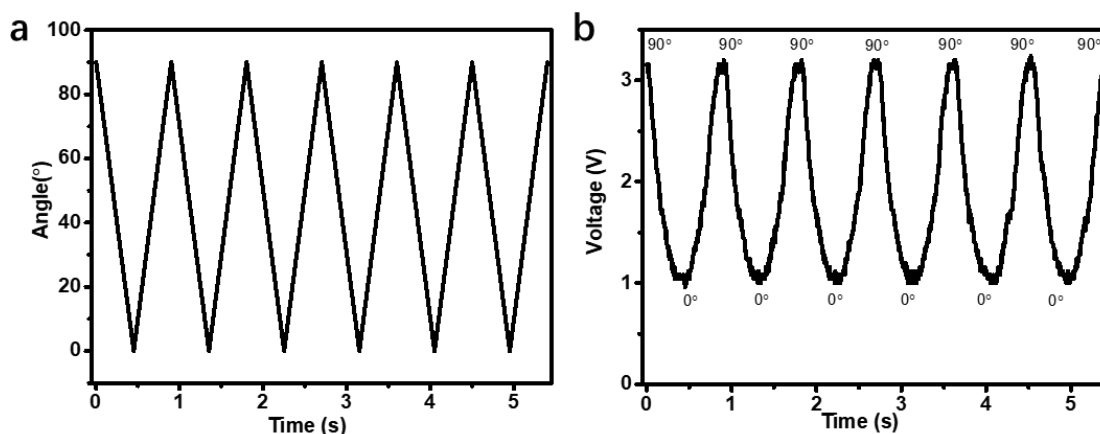


Figure 3.13 θ angle (a) and voltage (b) plotted over time when using a servo motor which equipped with a permanent magnet to apply the external magnetic field. The rotation rate of the servo motor is 10° per 50 ms. The voltage was measured by using the homemade IR photoelectric coupling system (see Figure 3.7d for circuit diagram). Insets in b are the corresponding θ angles.

For the demonstration of the application of our sensor, we designed a magnetic field direction sensor based actuator system, which could respond to the changing of magnetic field direction. Figure 3.12b (right part) shows the diagram of the actuator system. We connected our sensor with a MeArm base servo motor through ARDUINO. When changing θ by manually rotating the permanent magnet that placed beside the cuvette, the robotic arm could respond accordingly, as shown in Figure 3.12f. Here, we only confine the rotation of the robotic arm within 90° . However, it could be programmed to respond in a broader range, e.g., 180° or 360° , depending on the specific motor type and how to program it.

3.4 Conclusion

In conclusion, we successfully synthesized the anisotropic magnetic/plasmonic Fe_3O_4 NRs@ SiO_2 @Au core-shell nanocomposites by a post-reduction and seeded growth method. By applying an external magnetic field, the orientation of the nanocomposites could be dynamically controlled, which provides us the opportunity to measure the angle-dependent plasmonic extinction of the as-synthesized material.

Furthermore, we demonstrated the nanocomposites array, when fixed inside a polymer film, could serve as excellent building blocks for information encryption. We designed and fabricated a homemade IR photoelectric coupling system, which could generate different output voltages based on the extinction property of the measured sample. In particular, we have fabricated a six-column nanocomposite array film and demonstrate that it could realize multi-level information encryption. We believe that with more orientation control over the fixed nanocomposites and more complicated encoding and decoding methods, the information encryption security could be significantly improved.

Taking advantage of the instantaneous tuning over the orientation of the nanocomposites in solution, we extended the working principle and fabricated a new type of magnetic field direction sensor. The sensor could detect the magnetic field direction change, as the output voltage is compliant with a sine fit over the angle θ . An actuator system which consists of the sensor and a MeArm base servo motor vividly showed the performance of the sensing ability.

We envision that by miniaturization and integration, our anisotropic magnetic/plasmonic Fe_3O_4 NRs@ SiO_2 @Au shell nanocomposites based functional devices could find many other potential applications, such as mapping of the magnetic field, magnetosensitive precise control and measurement, and optical computing.

3.5 References

- (1) Kelly, K. L.; Coronado, E.; Zhao, L. L.; Schatz, G. C. *J. Phys. Chem. B* **2003**, 107, 668-677.
- (2) Li, N.; Zhao, P.; Astruc, D. *Angew. Chem., Int. Ed.* **2014**, 53, 1756-1789.
- (3) Wang, M.; Gao, C.; He, L.; Lu, Q.; Zhang, J.; Tang, C.; Zorba, S.; Yin, Y. *J. Am. Chem. Soc.* **2013**, 135, 15302-15305.
- (4) Murphy, C. J.; Sau, T. K.; Gole, A. M.; Orendorff, C. J.; Gao, J.; Gou, L.; Hunyadi, S. E.; Li, T. *J. Phys. Chem. B* **2005**, 109, 13857-13870.
- (5) Chen, H.; Shao, L.; Li, Q.; Wang, J. *Chem. Soc. Rev.* **2013**, 42, 2679-2724.
- (6) Zhang, Q.; Li, N.; Goebel, J.; Lu, Z.; Yin, Y. *J. Am. Chem. Soc.* **2011**, 133, 18931-18939.
- (7) Pérez-Juste, J.; Rodríguez-González, B.; Mulvaney, P.; Liz-Marzán, L. M. *Adv. Funct. Mater.* **2005**, 15, 1065-1071.
- (8) Ou, J.-Y.; Plum, E.; Zhang, J.; Zheludev, N. I. *Nat. Nanotechnol.* **2013**, 8, 252.
- (9) Liu, Y.; Han, X.; He, L.; Yin, Y. *Angew. Chem., Int. Ed.* **2012**, 51, 6373-6377.
- (10) Wang, M.; Yin, Y. *J. Am. Chem. Soc.* **2016**, 138, 6315-6323.
- (11) Zhang, M.; Magagnosc, D. J.; Liberal, I.; Yu, Y.; Yun, H.; Yang, H.; Wu, Y.; Guo, J.; Chen, W.; Shin, Y. J. et al. *Nat. Nanotechnol.* **2016**, 12, 228.
- (12) Wang, M.; He, L.; Zorba, S.; Yin, Y. *Nano Lett.* **2014**, 14, 3966-3971.
- (13) He, L.; Wang, M.; Ge, J.; Yin, Y. *Acc. Chem. Res.* **2012**, 45, 1431-1440.
- (14) Zijlstra, P.; Chon, J. W. M.; Gu, M. *Nature* **2009**, 459, 410.
- (15) Pham, H. H.; Gourevich, I.; Oh, J. K.; Jonkman, J. E. N.; Kumacheva, E. *Adv. Mater.* **2004**, 16, 516-520.
- (16) Raab, F. H.; Blood, E. B.; Steiner, T. O.; Jones, H. R. *IEEE Trans. Aerosp. Electron. Syst* **1979**, AES-15, 709-718.
- (17) van den Berg, H. A. M.; Clemens, W.; Gieres, G.; Rupp, G.; Vieth, M.; Wecker, J.; Zoll, S. *J. Magn. Magn. Mater.* **1997**, 165, 524-528.

- (18)Cañón Bermúdez, G. S.; Karnaushenko, D. D.; Karnaushenko, D.; Lebanov, A.; Bischoff, L.; Kaltenbrunner, M.; Fassbender, J.; Schmidt, O. G.; Makarov, D. *Science Advances* **2018**, 4.
- (19)Krahne, R.; Manna, L.; Morello, G.; Figuerola, A.; George, C.; Dekar, S. *Physical Properties of Nanorods*; Springer, **2013**.
- (20)Oldenburg, S. J.; Averitt, R. D.; Westcott, S. L.; Halas, N. J. *Chem. Phys. Lett.* **1998**, 288, 243-247.
- (21)Duff, D. G.; Baiker, A.; Edwards, P. P. *Langmuir* **1993**, 9, 2301-2309.
- (22)Wang, X.; Wang, C.; Cheng, L.; Lee, S.-T.; Liu, Z. *J. Am. Chem. Soc.* **2012**, 134, 7414-7422.
- (23)Palik, E. D. *Handbook of optical constants of solids*; Academic press, **1998**; Vol. 3.
- (24)Schlegel, A.; Alvarado, S. F.; Wachter, P. *J. Phys. C* **1979**, 12, 1157.
- (25)Wang, J.; Chen, Q.; Zeng, C.; Hou, B. *Adv. Mater.* **2004**, 16, 137-140.
- (26)Lian, S.; Wang, E.; Kang, Z.; Bai, Y.; Gao, L.; Jiang, M.; Hu, C.; Xu, L. *Solid State Commun.* **2004**, 129, 485-490.
- (27)Wang, M.; He, L.; Xu, W.; Wang, X.; Yin, Y. *Angew. Chem., Int. Ed.* **2015**, 54, 7077-7081.
- (28)Piao, Y.; Kim, J.; Na, H. B.; Kim, D.; Baek, J. S.; Ko, M. K.; Lee, J. H.; Shokouhimehr, M.; Hyeon, T. *Nat. Mater.* **2008**, 7, 242-247.
- (29)Wang, H.; Brandl, D. W.; Nordlander, P.; Halas, N. J. *Acc. Chem. Res.* **2007**, 40, 53-62.
- (30)Ge, J.; Hu, Y.; Yin, Y. *Angew. Chem.* **2007**, 119, 7572-7575.
- (31)Wang, M.; He, L.; Hu, Y.; Yin, Y. *J. Mater. Chem. C* **2013**, 1, 6151-6156.

Chapter 4 Confined Growth of Gold/Silver Nanostructures within Resorcinol-formaldehyde (RF) Resin Templates

4.1 Introduction

Templating is one of the most important techniques for the controlled synthesis of nanostructured materials. This powerful tool uses a pre-existing guide with desired nanoscale features to direct the formation of nanomaterials into forms that are otherwise difficult to obtain.¹ Compared to the soft templating method, the hard templating strategy is conceptually simple. When a solid template is used, it results in hollow nanostructures; and when a hollow structure is used as a template, the synthesized structure will replicate the size and shape of the hollow space, and thus result in some solid structures.² One of the advantages of the templating process is its potential for large-scale production.

Gao et al. reported a general method for the synthesis of noble metal nanorods, including Au, Ag, Pt, and Pd, based on the seeded growth process within silica nanotube.³ Silica nanotubes were synthesized by templating against nickel-hydrazine nanorods. Before the sol-gel coating of silica on the template, a layer of 3-aminopropyltriethoxysilane (APS) was first coated onto the nickel-hydrazine nanorods surface. The purpose of APS coating is to introduce amino groups inside the silica shell, facilitating the selective gold seed loading (Figure 4.1a). After seeded growth and removal of silica templates, high-quality Au nanorods were finally synthesized (Figure 4.1d). By varying the aspect ratios of silica nanotubes, the aspect ratio, as well as the plasmonic properties of gold nanorods, could be readily tuned. When a different metal precursor was used, metal nanorods with different compositions, such as Ag, Pt, and Pd,

could be successfully achieved. This method affords large quantities of noble metal nanorods with well-controlled aspect ratios and high yield.

As mentioned above, when a solid template was used, it results in hollow nanostructure if the template was completely removed. However, if solid spherical particles are used as the templates, we will get isotropic spherical shells, such as the gold shell^{4,5} or hollow titania shell^{6,7}. But if we change the hard template to be anisotropic, like nanorods or nanowires, then the anisotropic hollow structure will be synthesized (Figure 4.2a). For example, galvanic replacement reaction between silver nanowires and HAuCl_4 could produce Au/Ag alloyed nanotubes.⁸

Even based on an isotropic template, anisotropic nanostructure could also be synthesized through the combination of template synthesis and post-treatment method. Gao et al. reported a novel confined-space thermal dewetting strategy for the fabrication of Au nanocups with tunable diameter, height, and size of cup opening.⁹ The nanocup morphology is defined by the cup-shaped void space created by a yolk-shell silica template that spontaneously takes an eccentric configuration during annealing. Thermal dewetting of Au, which is sandwiched between the yolk and shell, leads to the desired nanocup morphology.

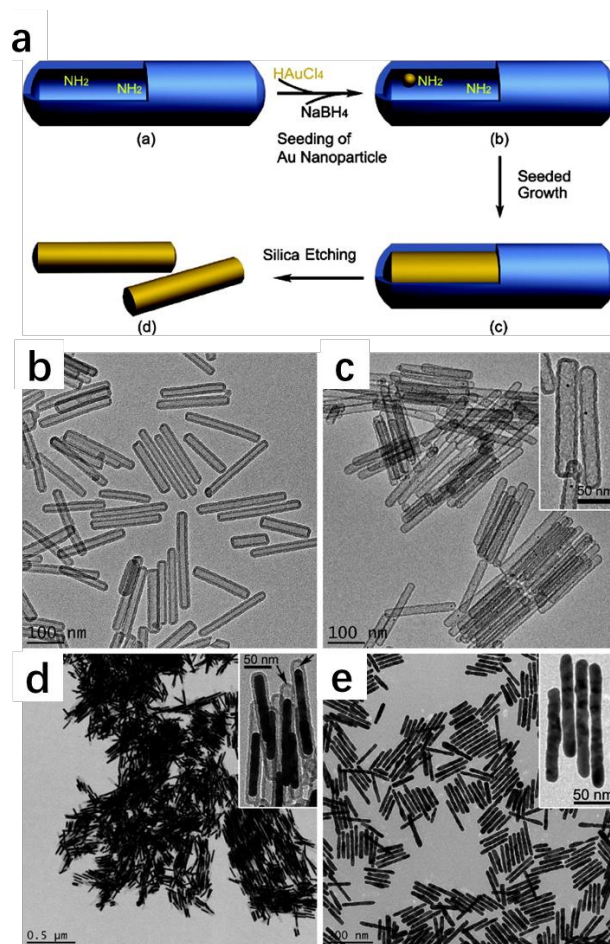


Figure 4.1 Template synthesis of AuNRs by using hollow silica tube as templates. (a) Scheme showing a general templating approach to the synthesis of metal nanorods. (b-e) TEM images of the (b) silica nanotubes with inner cavity functionalized with amino groups; (c) Au seed@silica nanotubes; (d) Au nanorod@silica nanotubes after seeded growth; (e) Au nanorods after removal of silica templates. Reprinted with permission from Ref. ³. Copyright © 2011 American Chemical Society.

Figure 4.2b shows the scheme of the confined dewetting process for the fabrication of Au nanocups. In general, silica spheres are coated sequentially with RF, Au, and SiO₂ layers, followed by calcination in the air to remove RF and dewet Au from SiO₂ surface, and then etching SiO₂ templates to release Au nanocups. Figure 4.2c-e show the SEM images of a series of Au nanocups prepared by using SiO₂@RF templates with a core diameter of ≈ 350 nm and RF thickness of 25, 18, and 12 nm. With the decrease in RF thickness, the height of Au nanocups increased, and the size of the cup opening decreased. The overall size of the Au nanocups could also be controlled by changing the size of the silica templates. Figure 2.4 f-h show the Au nanocups with the size of ≈ 120 , 300, and 400 nm prepared using silica templates with a diameter of ≈ 80 , 250, and 350 nm.

In this chapter, we adopted the templating strategy and realized the confined growth of gold and silver nanorods within hollow RF resins by using β -FeOOH nanorods as a sacrificial template through a seeded growth method. Also, without removing the FeOOH nanorod templates, the anisotropic gold shell could be synthesized. Since the size and aspect ratio of the β -FeOOH nanorods could be easily adjusted during the synthesis procedure, it would be a versatile platform for the synthesis of gold/silver nanorods with different sizes and aspect ratios. Also, compared to traditionally used silica, the RF shell is more porous and stretchable, which not only prevents the self-nucleation of the metal nanoparticles outside of the templates, but also offers more size tunability within one Au seed@RF template.

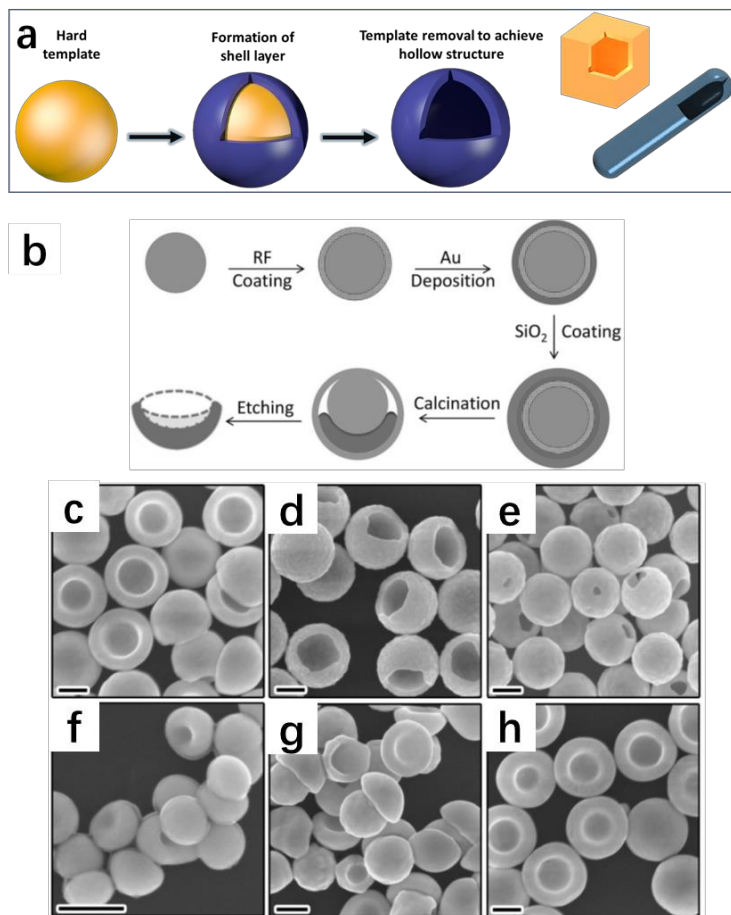


Figure 4.2 Template synthesis of anisotropic nanostructures. (a) Scheme showing the template synthesis of hollow anisotropic nanostructures. Reprinted with permission from Ref. ². Copyright © 2016 American Chemical Society. (b) Outline of the confined dewetting process for the fabrication of Au nanocups. (c-h) SEM images of the Au nanocups prepared using templates of 350 nm silica coated with RF thickness of (a) 25 nm, (b) 18 nm, and (c) 12 nm, demonstrating the convenient control over cup opening by the thickness of the RF layer. (d-f) SEM images of Au nanocups obtained using silica cores with diameters of ≈ 80 , ≈ 250 , and ≈ 350 nm. All scale bars are 200 nm. Reprinted with permission from Ref. ⁹. Copyright © 2013 John Wiley and Sons.

4.2 Materials and Methods

4.2.1 Materials

Iron(III) chloride hexahydrate ($\text{FeCl}_3 \cdot 6\text{H}_2\text{O}$), polyacrylic acid (PAA, average M.W. 1800), tetraethyl orthosilicate (TEOS), diethylene glycol (DEG), cystamine, gold(III) chloride trihydrate ($\text{HAuCl}_4 \cdot 3\text{H}_2\text{O}$), tetrakis-(hydroxymethyl)phosphonium chloride (THPC), Resorcinol (R), formaldehyde (HCHO), potassium iodide (KI), and L-ascorbic acid (AA) were purchased from Sigma-Aldrich. $\text{NH}_3 \cdot \text{H}_2\text{O}$ solution (28%), NaOH, K_2CO_3 , oxalic acid, acetonitrile (ACN), sodium citrate tribasic dihydrate (TSC, 99 %), and silver nitrate (AgNO_3) were purchased from Fisher Scientific. Ethanol (200 proof) was purchased from Decon Laboratories Inc. Polyvinylpyrrolidone (PVP, K12, average M.W. 3500) was purchased from Acros Organics. All the chemicals were used as received.

4.2.2 Synthesis of Gold and Silver NRs within Hollow RF Templates

(1) Surface modification of FeOOH NRs by cystamine.

Small FeOOH nanorods (158 * 33 nm) were synthesized by the hydrolysis of $\text{FeCl}_3 \cdot 6\text{H}_2\text{O}$. Typically, 0.1 M $\text{FeCl}_3 \cdot 6\text{H}_2\text{O}$ solution was sealed in a pyrex bottle and aged in an oven at 40 °C for 50 h. After washing with water, the nanorods were then modified by cystamine to facilitate the gold seed loading. For cystamine modification, 120 mg of the small FeOOH nanorods dispersed in 10 mL DI water was mixed with 0.5 mL of 0.02 M cystamine solution. After incubation and vortex for about 10 min, the mixture was washed with water at 15,000 rpm for 8 min to remove the excess cystamine.

(2) Gold seed loading

Tiny gold seeds (about 1-2 nm) were synthesized following a reported protocol¹⁰ with slight modification. Please refer to section 3.2.3 for detail. For gold seed loading, 120 mg of cystamine modified nanorods (FeOOH-Cys) which re-dispersed in water was added to 10 mL of the above THPC gold seeds dropwise under sonication. After addition, the mixture was stirred for 60 min. Free gold seeds were removed by washing with water for twice, and the seed loaded nanorods (FeOOH-Cys-Au seed) were re-dispersed in 12 mL of water (10 mg/mL).

(3) RF coating

Before RF coating on the gold seed loaded FeOOH nanorods, PAA modification was performed. Typically, 0.12 mL of $\text{NH}_3 \cdot \text{H}_2\text{O}$ solution (28%) was added to 15 mL of 0.1 M PAA solution to adjust the pH to 8-9. Then 12 mL of the above FeOOH-Cys-Au seed was added to the PAA solution. The mixture was incubated during stir for 4 h. After incubation, excess PAA was removed by washing.

For RF coating, 120 mg of the above FeOOH-Cys-Au seed-PAA nanorods were dispersed into 27 mL DI water. Then 15 mg resorcinol and 21 μL formaldehyde were added. The mixture was heated up to 60 °C in a 3-neck flask. Then 20 μL of ammonia solution (28%) was added. The mixture was first incubated at 60 °C for 2 h, then refluxed at 100 °C for 6 h. After the reaction, the RF coated nanorods were then collected by centrifugation.

(4) Removal of FeOOH nanorods

Oxalic acid etching was used to remove the inner FeOOH nanorods. Typically, 40 mg of the RF coated FeOOH-Cys-Au seed-PAA nanorods were added to 0.5 M of the oxalic acid solution and incubated for 3 h. After the reaction, the mixture was washed with water at 11,000 rpm for 3 min, and then re-dispersed into 4 ml DI water (10 ml/mL) to get Au hollow seed@void@RF templates.

(5) Seeded growth of gold

The growth of gold nanorods inside the hollow Au seed@void@RF templates was conducted following a reported method with some modification.³ Typically, in a glass vial, under stirring, chemicals were added in the following order: 2 mL of water, 200 μ L of PVP solution (MW = 3500, 5 % in water), 200 μ L of KI (0.2 M), 160 μ L of ascorbic acid (AA, 0.1 M), and 120 μ L of HAuCl₄ (0.05 M), forming a clear colorless solution (growth solution). Then, 100 μ L of the hollow Au seed@void@RF templates stock solution (10 ml/mL) was injected into the growth solution, and the growth of Au nanorods started immediately, accompanied by a significant color change. After 10 min of reaction, the Au nanorod@RF material was collected by centrifugation and washed with water. When different amount of HAuCl₄ was used, the amount of AA was adjusted accordingly to keep the constant ratio of gold precursor to AA.

(6) Seeded growth of silver

The growth of silver nanorods inside hollow Au seed@void@RF templates was conducted following a reported method with some modification.³ In a glass vial, under stirring, chemicals were added in the following order: 2 mL of acetonitrile (ACN), 1 mL

of TSC solution (0.1 M), 200 μ L of ascorbic acid (0.1 M), and 100 μ L of the Au seed@void@RF hollow tube stock solution (10 ml/mL) stock solution, forming a clear light pink solution (growth solution). Then, 50 μ L of AgNO₃ (0.1 M) was injected into the growth solution, and the growth of Ag nanorods started immediately, accompanied by a significant color change from pink to red, blue, gray. After 20 min of reaction, the Ag nanorod@RF was collected by centrifugation and washed with water.

4.2.3 Confined Growth of Gold Shell within Fe_xO_y@RF Templates

(1) Synthesis of FeOOH@RF nanorods

FeOOH nanorods (270 * 47 nm) were synthesized by the hydrolysis of FeCl₃·6H₂O. Typically, 0.1 M FeCl₃·6H₂O solution was sealed in a pyrex bottle and aged in an oven at 60 °C for 6 days. Before RF coating, the as-synthesized β -FeOOH nanorods were first modified by PAA (Please refer to Section 2.3.2 for detail).

For RF coating, 30 mg of the above FeOOH- PAA nanorods were dispersed into 84 mL DI water. Then 75 mg resorcinol and 105 μ L formaldehyde were added. The mixture was heated up to 60 °C in a 3-neck flask. Then 60 μ L of ammonia solution (28%) was added. The mixture was first incubated at 60 °C for 2 h, then refluxed at 100 °C for 6 h. After the reaction, the RF coated nanorods were then collected by centrifugation

(2) Partial reduction to form Fe_xO_y@RF nanorods

Polyol reduction and carbothermal reduction methods were used for the partial reduction of FeOOH@RF to form Fe_xO_y@RF nanorods. For polyol reduction, DEG was used as the solvent and reducing agent, the FeOOH@RF nanorods were reduced at 220 °C for 10 min. For carbothermal reduction, the FeOOH@RF nanorods were first

dried into a powder and then calcinated for 2 h at 200 °C and 300 °C, respectively. To improve the dispersibility after carbothermal reduction, the FeOOH@RF nanorods were first coated by another layer of silica, and then calcinated for 2 h at 300 °C and 400 °C, respectively. After reduction, the silica layer was removed by NaOH etching.

(3) In-situ growth of the gold shell

In-situ growth of the gold shell was achieved by refluxing with H_{Au}Cl₄. Typically, 0.5 mg of Fe_xO_y@RF nanorods were first dispersed in 25 mL DI water. Then 20 µL of ammonia solution (28%) and 100 µL of 0.05 M H_{Au}Cl₄ were added. The mixture was first heated to 100 °C and then refluxed for 90 min. After the reaction, the product was collected by centrifugation and washed with water. Control experiments were conducted without the addition of ammonia solution or with the addition of other bases, such as NaOH.

4.3 Results and Discussion

4.3.1 Synthesis of Gold and Silver NRs within Hollow RF Templates

Based on the reported templating synthesis method, we adopt the strategy and realize the confined growth of gold and silver nanorods within resorcinol-formaldehyde (RF) resin by using β -FeOOH nanorods as sacrificial templates through a seeded growth method. Figure 4.3a shows the scheme for the synthesis procedure. First, FeOOH nanorods were modified by cystamine, which could bond to the surface of FeOOH through click chemistry. After cystamine modification, the free amino groups and disulfide groups could be used to immobilize tiny gold seeds. Then, a layer of RF resin was coated on the seed loaded nanorods. After completely removal of the FeOOH nanorods by oxalic acid etching, following by a seeded growth process, the gold or silver nanorods could be synthesized within the hollow Au seed@RF templates.

Figure 4.3b shows the TEM image of the FeOOH nanorods. The uniform small nanorods were used as the sacrificial templates. Figure 4.3c shows that the tiny gold seeds could be successfully anchored onto the surface of FeOOH nanorods, and a thin layer of RF has been coated. After completely removal of the nanorods, we got the hollow Au seed@void@RF templates (Figure 4.3d). Compared to Figure 4.3c, there is some ripening of the gold seeds after removal of the FeOOH nanorods. However, the small gold seeds have not ripened to form a single gold nanoparticle.

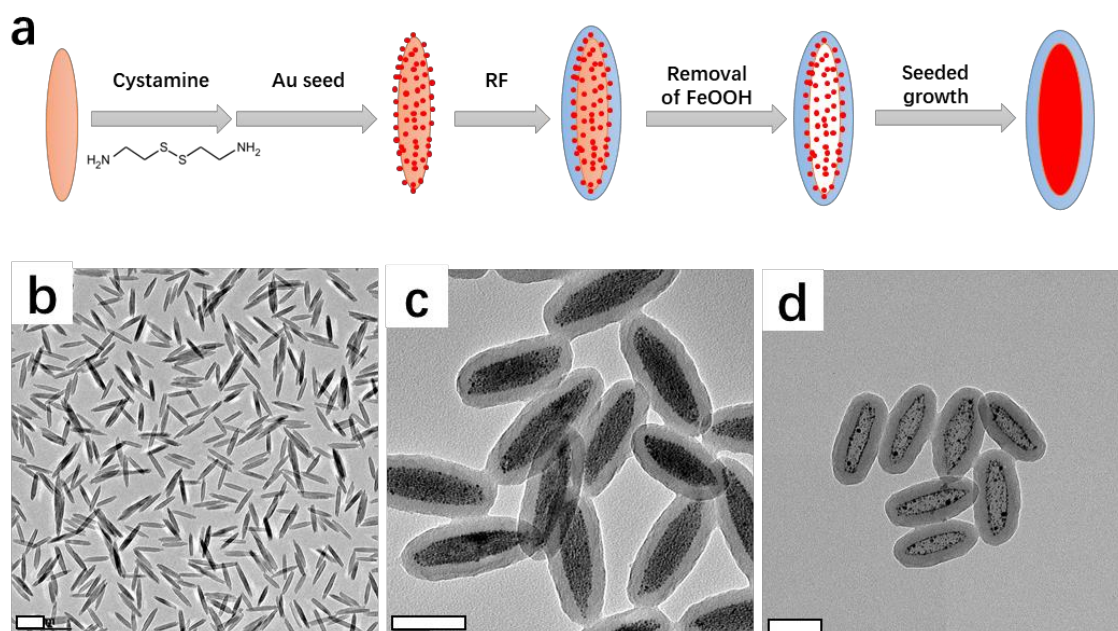


Figure 4.3 Confined growth of Au/Ag nanostructures within RF resin by using FeOOH NRs as templates: synthesis strategy and Au seed loading. (a) Scheme for the synthesis strategy. (b) TEM image of FeOOH NRs. (c) TEM image of Au seed loaded FeOOH NRs after RF coating. (d) TEM image of Au seed@void@RF when removing the FeOOH NRs template. Scale bars are 100 nm.

The growth of gold nanorods inside hollow Au seed@void@RF templates was conducted following a reported method with some modification.³ When only 5 μL of HAuCl_4 was added, the nanorods are relatively shorter, with the longitudinal extinction peak located at 650 nm (Figure 4.4g and Table 4.1). In some of the hollow RF templates, there are more than one of the shorter nanorods, and the size is not very uniform. This also explains why the longitudinal peak is relatively broad.

When increased the amount of HAuCl_4 to 7.5 μL , there was an obvious red-shift of the longitudinal peak from 650 nm to 809 nm. Considering that we only added 2.5 μL more of the gold precursor, the large red-shift could be attributed to the coalescence of adjacent shorter nanorods into longer ones, as shown in the TEM image (Figure 4.4c).

Further increasing the amount of HAuCl_4 to 20 μL , the longitudinal peak red-shifted to 914 nm, and another peak at about 650 nm emerged. As we could see from the TEM image (Figure 4.4d), the nanorods are ellipsoidal, rather than cylindrical, due to the shape of the FeOOH nanorods. The new peak at about 650 nm could arise from the roughness of the surface of the nanorods.¹¹ It is worth noting that the size of the gold nanorods is $166 * 51$ nm, which is larger than the FeOOH nanorods templates ($158 * 33$ nm), especially in the width direction.

When 30 μL of HAuCl_4 was added, the gold nanorods become larger and larger, with the size of $167 * 68$ nm. Since the increase in width is more obvious so that it resulted in even decreasing aspect ratio from 3.2 to 2.5. The longitudinal peak blue-shifted to 872 nm, which is consistent with the aspect ratio change.

When 60 μL of HAuCl_4 was added, the gold nanorods become even larger with the size of 207×101 nm. Compared to the original width of the FeOOH nanorods, the width of the gold nanorods right now is almost three times larger.

All the above results demonstrate that gold nanorods with different size and aspect ratios could be synthesized within the same hollow Au seed@void@RF templates. The RF shell is more porous and stretchable, which not only prevents the self-nucleation of the metal nanoparticles outside of the templates, but also offers more size tunability within one Au seed@RF template.

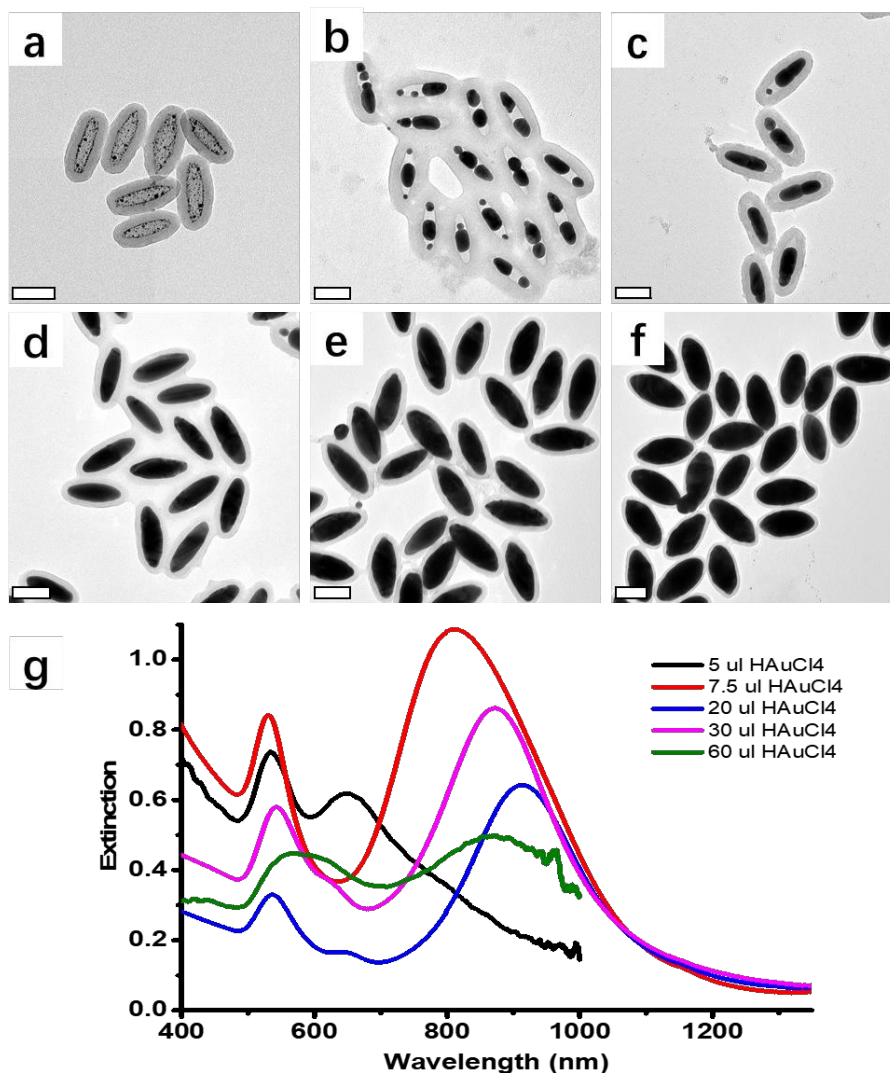


Figure 4.4 Confined growth of Au nanorods within RF resin by using FeOOH NRs as templates: the seeded growth of gold with different amount of HAuCl₄. (a-f) TEM images of (a) Au seed@void@RF template and AuNRs synthesized by seeded growth with (b) 5 μ L, (c) 7.5 μ L, (d) 20 μ L, (e) 30 μ L, and (f) 60 μ L of 0.05 M HAuCl₄. (g) Extinction spectra of the as-synthesized AuNRs with different amount of HAuCl₄. Scale bars are 100 nm.

Table 4.1 Size and aspect ratio evolution of Au nanorods during the seeded growth with different amount of H_{AuCl₄}.

V _{H_{AuCl₄}} (μ L)	Transverse (nm)	Longitudinal (nm)	Length (nm)	Width (nm)	AR
5	534	650	-	-	-
7.5	529	809	116	39	3.0
20	537/650	914	166	51	3.2
30	543/630	872	167	68	2.5
60	568/628	872	207	101	2.1

The growth of silver nanorods inside the hollow Au seed@void@RF templates was conducted following a reported method with some modification.³ As shown in Figure 4.5a, the silver nanorods synthesized by using the same seed were not as complete as the gold nanorods, and it is more like some small silver nanoparticles' aggregation. This may be due to multiple gold seeds inside one template. Also, there is no obvious extinction peak for the as-synthesized silver nanorods. More efforts will be put into the optimization for the synthesis parameters of silver nanorods.

We also did the seeded growth of silver when using the pre-synthesized smaller gold nanorods as seeds. The products for the seeded growth of original Au seed@void@RF templates with 5 μL of HAuCl_4 were used as the new seeds. After seeded growth of silver, we aim to form Au/Ag alloy nanorods. As shown in Figure 4.5c, when 45 μL of AgNO_3 was added, the nanorods did become longer. From the contrast difference, we could distinguish silver from the original gold nanorods part. However, the extinction spectra after seeded growth of silver did not show much difference, with slightly blue-shift of the transverse mode and slightly red-shift of the longitudinal mode, while the relative peak intensity did not change much.

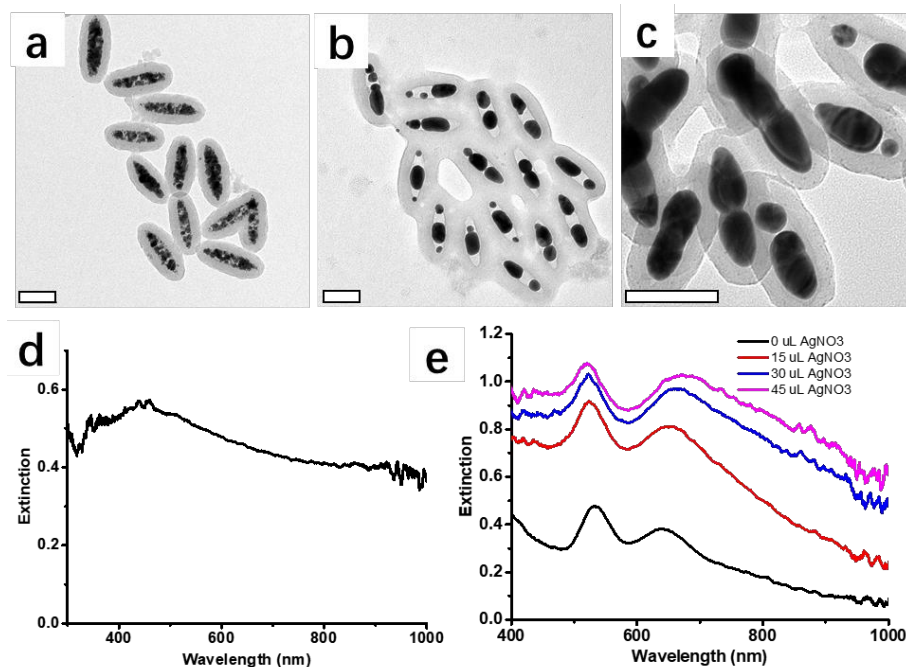


Figure 4.5 Confined growth of Ag nanorods within RF resin by using FeOOH NRs as templates: seeded growth. (a, d) The growth of silver based on Au seed@void@RF. (a) TEM image of Ag nanorod synthesized by using 50 μL of 0.1 M AgNO_3 . (d) Extinction spectrum of the synthesized Ag nanorod. (b, c & e) The growth of silver based on Au NRs@void@RF. (b) AuNRs synthesized by seeded growth with 5 μL HAuCl_4 of as the seed for the growth of silver. (c) TEM image after growth of silver by using 45 μL of 0.1 M AgNO_3 . (e) Extinction spectra before and after growth of silver. Scale bars are 100 nm.

4.3.2 Confined Growth of Gold Shell within $\text{Fe}_x\text{O}_y\text{@RF}$ Templates

From section 4.3.1, we learned that RF is very flexible and stretchable. Based on the previous results, the width of the RF capsule could extend to almost three times of its original size. We then considered a situation when the FeOOH nanorods are not removed from the FeOOH@RF composites. Due to the flexibility of the RF shell, it would be possible to selectively grow gold shell between the FeOOH NRs and the RF shell.

Figure 4.6a shows the scheme for the synthesis procedure. First, FeOOH@RF was transferred to $\text{Fe}_x\text{O}_y\text{@RF}$ nanorods through a partial reduction process. Then the partially reduced Fe_xO_y nanorods could serve as the reducing agent, and the in-situ growth of gold shell could happen on the surface of Fe_xO_y nanorods. Due to confinement effect of the RF layer, a complete shell should be formed.

Figure 4.6b-k and Table 4.2 show the experimental results when different partially reduced FeOOH@RF nanorods were incubated with HAuCl_4 . Among all the trials, only when the FeOOH@RF nanorods were reduced by carbothermal reduction at 300 °C for 2 h, and with the presence of $\text{NH}_3\cdot\text{H}_2\text{O}$ when incubated with HAuCl_4 , the gold shell could be formed. All the other trials, we only got some irregularly shaped gold nanoparticles. Even for the case with the formation of the gold shell, the yield is not 100%. We could also observe some small nanoparticles on the surface of RF shell.

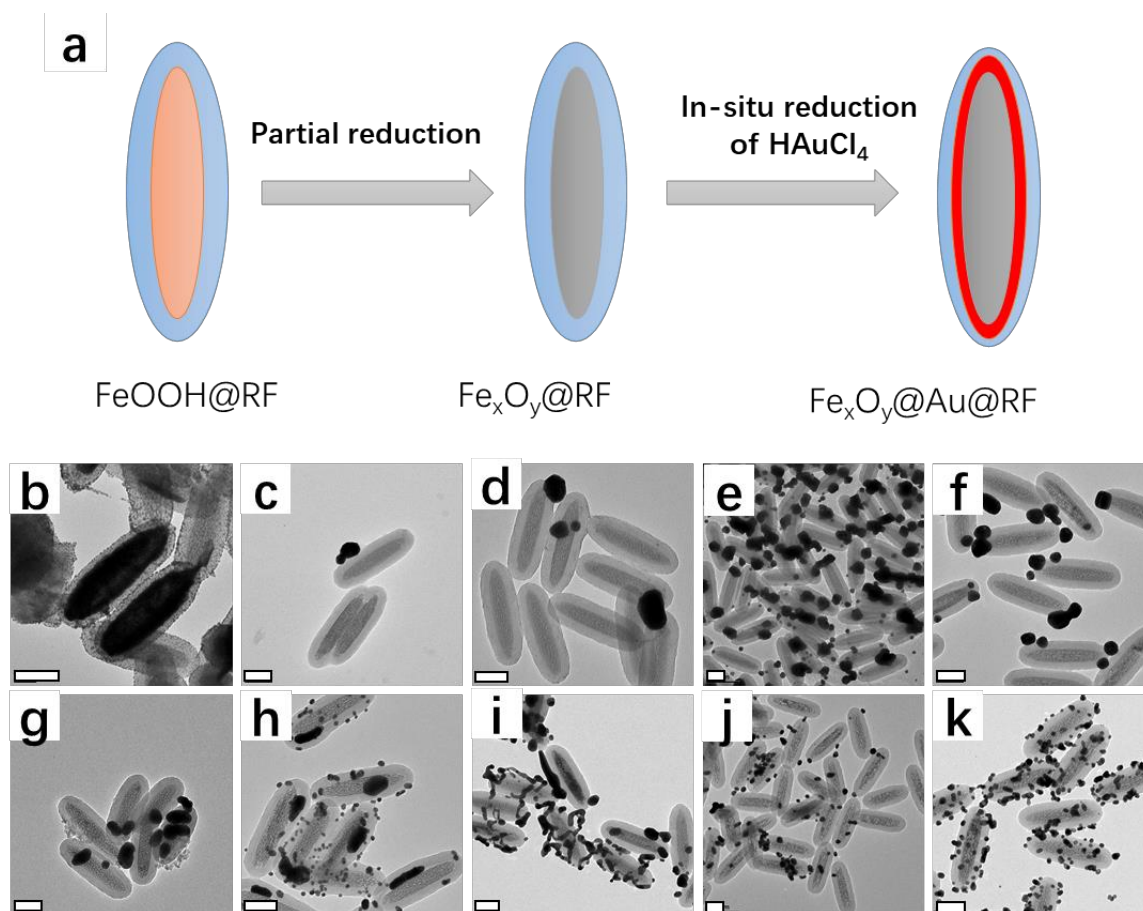


Figure 4.6 Confined growth of gold shell within $\text{Fe}_x\text{O}_y @\text{RF}$ composite. (a) scheme showing the synthesis procedure. (b-k) TEM images of partially reduced $\text{FeOOH}@\text{RF}$ nanorods incubated with HAuCl_4 with (b-f) and without (g-k) the addition of $\text{NH}_3 \cdot \text{H}_2\text{O}$. The partial reduction parameters are 300 °C, 2 h by carbothermal reduction (b, g), 300 °C, 2 h by carbothermal reduction with the protection of silica (c, h), 200 °C, 2 h by carbothermal reduction (d, i), 400 °C, 2 h by carbothermal reduction with the protection of silica (e, j), and 220 °C, 10 min by DEG. Scale bars are 100 nm.

Table 4.2 Summary of different partial reduction methods and their product when incubated with HAuCl_4 .

FeOOH@RF treatment	With $\text{NH}_3\cdot\text{H}_2\text{O}$	Without $\text{NH}_3\cdot\text{H}_2\text{O}$
300 °C, 2 h	Shell	NPs outside the shell
300 °C, 2 h (silica)	Free Au NPs	NPs both inside and outside
200 °C, 2 h	NPs outside	Large NPs
400 °C, 2 h (silica)	Large NPs outside	Small NPs outside
220 °C, 10 min by DEG	Large NPs outside	Small NPs outside

We then investigated the in-situ growth process of the gold shell. Figure 4.7a shows the absorbance spectra of the $\text{Fe}_x\text{O}_y @ \text{Au shell} @ \text{RF}$ composites with different incubation time during the synthesis. Unfortunately, with time increasing, only the intensity of the spectrum increased. Since there is no obvious peak for the tested sample, we could not learn more about the shell growth process. This may due to the low yield of the gold shell since the majority in the samples are $\text{Fe}_x\text{O}_y @ \text{RF}$ nanorods. However, it still could not explain why the scattering of the sample becomes stronger with the increasing reaction time.

We also tried to improve the yield of the gold shell by adjusting the concentration of $\text{NH}_3 \cdot \text{H}_2\text{O}$. When compared the results of Figure 4.6b & g, we found that the role of $\text{NH}_3 \cdot \text{H}_2\text{O}$ is critical for the formation of gold shell. Without $\text{NH}_3 \cdot \text{H}_2\text{O}$, only some large gold nanoparticles could be formed. As shown in Figure 4.8a, when decreased the amount of $\text{NH}_3 \cdot \text{H}_2\text{O}$ from 200 μL to 40 μL , the yield of gold shell became lower, as we could only find few gold shells. When increased the amount of $\text{NH}_3 \cdot \text{H}_2\text{O}$ to 400 μL , the yield became higher. However, for both cases with 200 μL and 400 μL , the yields were both relatively low. To eliminate the pH influence, we did the control experiment by using NaOH. For the standard recipe, when 200 μL of $\text{NH}_3 \cdot \text{H}_2\text{O}$ was added, the pH was 10.58. We then adjusted the pH to 10.5 by adding NaOH to the synthesis solution. From the TEM images, no gold shell formed, and we could only observe some large gold nanoparticles on the surface of RF shell.

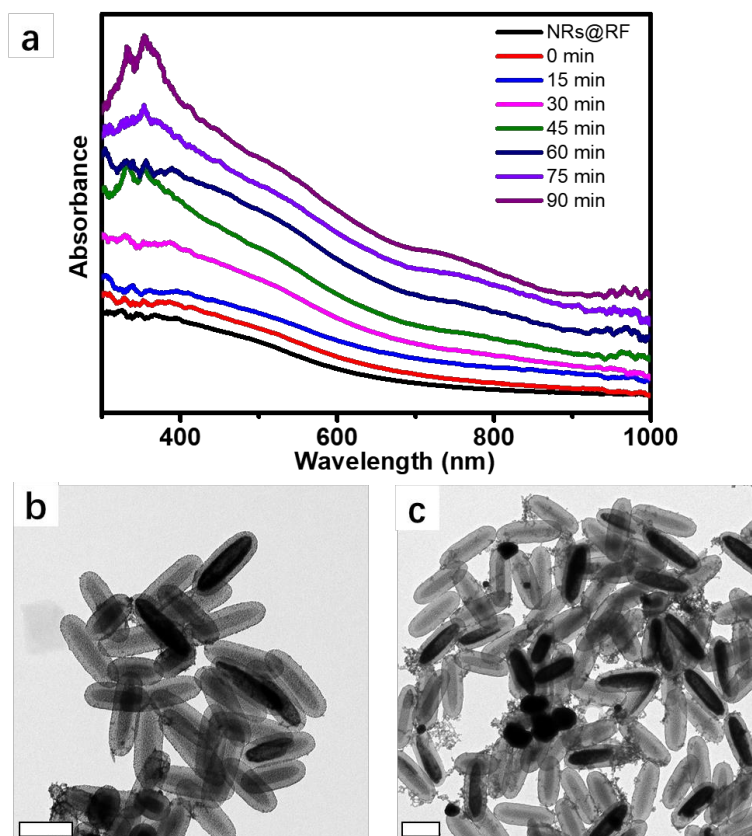


Figure 4.7 Confined growth of gold shell within Fe_xO_y @RF composite with different reaction time. (a) UV-Vis spectra of samples synthesized with different reaction time. (b, c) TEM images of samples synthesized with 45 min (b) and 90 min (c), respectively. Scale bars are 200 nm.

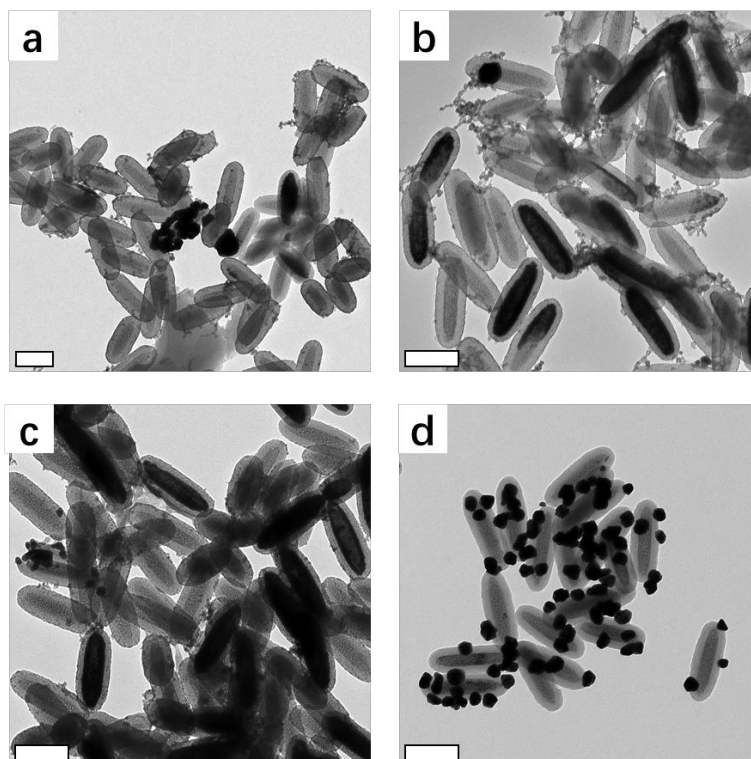


Figure 4.8 Effect of the concentration of $\text{NH}_3 \cdot \text{H}_2\text{O}$. TEM images of sample synthesized with (a) $40 \mu\text{L}$ $\text{NH}_3 \cdot \text{H}_2\text{O}$, (b) $200 \mu\text{L}$ $\text{NH}_3 \cdot \text{H}_2\text{O}$, (c) $400 \mu\text{L}$ $\text{NH}_3 \cdot \text{H}_2\text{O}$, and (d) NaOH . Scale bars are 200 nm.

To confirm the formation of the gold shell, selective etching of either the inner Fe_xO_y nanorods or the RF shell was performed. From Figure 4.9a, when the Fe_xO_y nanorods were removed by oxalic acid etching at 60 °C for 3 h, we could see the shell structure more clearly, even though the shells were not as completely as before. When the RF shell was removed by NaOH etching at 100 °C for 24 h, from some broken parts of the shell, we could see that it is the nanoshell that surrounding the surface of the Fe_xO_y nanorods. For both cases, the quality decrease of the shell may be attributed to the selective etching procedure, since gold shell could still undergo the ripening process during etching.

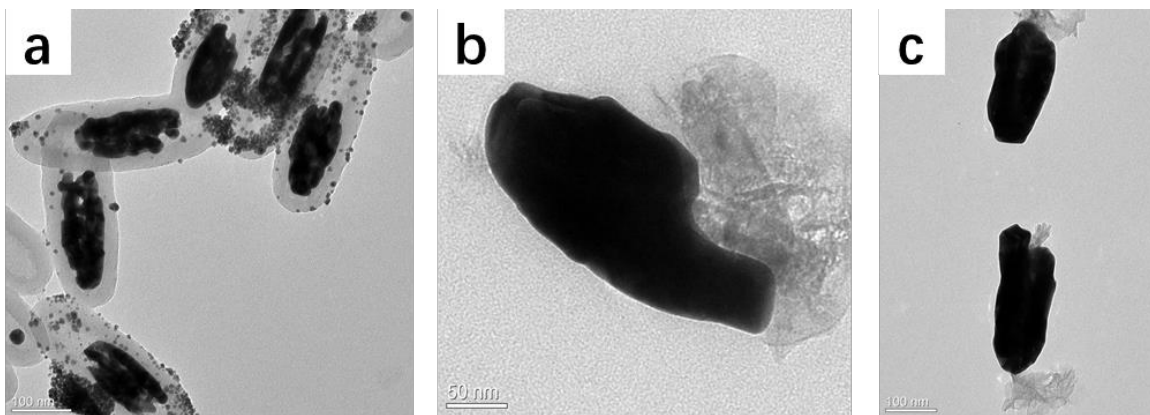


Figure 4.9 (a) TEM image of $\text{Fe}_x\text{O}_y@\text{Au shell}@\text{RF}$ when etching away the Fe_xO_y nanorods. (b, c) TEM image of $\text{Fe}_x\text{O}_y@\text{Au shell}@\text{RF}$ when etching away the RF layer.

4.4 Conclusion

In conclusion, we adopted the templating strategy and realize the confined growth of gold and silver nanorods within RF by using β -FeOOH nanorods as sacrificial templates through a seeded growth process. By controlling the amount of gold precursor added during the seeded growth process, Au nanorods with different sizes and aspect ratios could be synthesized by using the same template. Compared to traditionally used silica, the RF shell is more porous and stretchable, which not only prevents the self-nucleation of the metal nanoparticles outside of the templates, but also offers more size tunability within one Au seed@RF template. The growth of silver has also been tried, but due to the poor quality of the nanorods, we did not observe obvious extinction peak. More efforts will be put into the optimization for the synthesis parameters of silver nanorods.

Also, without removing the FeOOH nanorod templates, the partially reduced Fe_xO_y @RF could serve as the reducing agent, and facilitates the gold shell formation between Fe_xO_y nanorod and RF layer. Among all the trials, only when the FeOOH@RF nanorods were reduced by carbothermal reduction at 300 °C for 2 h, and with the presence of $\text{NH}_3\cdot\text{H}_2\text{O}$ when incubated with HAuCl_4 , the gold shell could be formed. Control experiments show that during the formation of the gold shell, $\text{NH}_3\cdot\text{H}_2\text{O}$ plays an important role. Overall, the yield of the gold shell is relatively low, and more efforts should be put into the investigation of formation mechanism and optimization of the shell quality.

4.5 References

- (1)Liu, Y.; Goebel, J.; Yin, Y. *Chem. Soc. Rev.* **2013**, 42, 2610-2653.
- (2)Wang, X.; Feng, J.; Bai, Y.; Zhang, Q.; Yin, Y. *Chem. Rev.* **2016**, 116, 10983-11060.
- (3)Gao, C.; Zhang, Q.; Lu, Z.; Yin, Y. *J. Am. Chem. Soc.* **2011**, 133, 19706-19709.
- (4)Zhang, Q.; Ge, J.; Goebel, J.; Hu, Y.; Sun, Y.; Yin, Y. *Adv. Mater.* **2010**, 22, 1905-1909.
- (5)Prodan, E.; Radloff, C.; Halas, N. J.; Nordlander, P. *Science* **2003**, 302, 419-422.
- (6)Liu, H.; Joo, J. B.; Dahl, M.; Fu, L.; Zeng, Z.; Yin, Y. *Energy Environ. Sci.* **2015**, 8, 286-296.
- (7)Joo, J. B.; Lee, I.; Dahl, M.; Moon, G. D.; Zaera, F.; Yin, Y. *Adv. Funct. Mater.* **2013**, 23, 4246-4254.
- (8)Sun, Y.; Xia, Y. *J. Am. Chem. Soc.* **2004**, 126, 3892-3901.
- (9)Gao, A.; Xu, W.; Ponce de León, Y.; Bai, Y.; Gong, M.; Xie, K.; Park, B. H.; Yin, Y. *Adv. Mater.* **2017**, 29, 1701070.
- (10)Duff, D. G.; Baiker, A.; Edwards, P. P. *Langmuir* **1993**, 9, 2301-2309.
- (11)Huang, Y.; Wu, L.; Chen, X.; Bai, P.; Kim, D.-H. *Chem. Mater.* **2013**, 25, 2470-2475.